



# Long-term MAX-DOAS measurements of NO<sub>2</sub>, HCHO, and aerosols and evaluation of corresponding satellite data products over Mohali in the Indo-Gangetic Plain

Vinod Kumar<sup>1</sup>, Steffen Beirle<sup>1</sup>, Steffen Dörner<sup>1</sup>, Abhishek Kumar Mishra<sup>2</sup>, Sebastian Donner<sup>1</sup>, Yang Wang<sup>1</sup>, Vinayak Sinha<sup>2</sup>, and Thomas Wagner<sup>1</sup>

<sup>1</sup>Max Planck Institute for Chemistry, Mainz, Germany

<sup>2</sup>Department of Earth and Environmental Sciences, Indian Institute of Science Education and Research Mohali, Mohali, India

**Correspondence:** Vinod Kumar (vinod.kumar@mpic.de)

Received: 24 April 2020 – Discussion started: 15 May 2020

Revised: 9 October 2020 – Accepted: 13 October 2020 – Published: 23 November 2020

**Abstract.** We present comprehensive long-term ground-based multi-axis differential optical absorption spectroscopy (MAX-DOAS) measurements of aerosols, nitrogen dioxide (NO<sub>2</sub>), and formaldehyde (HCHO) from Mohali (30.667° N, 76.739° E; ~ 310 m above mean sea level), located in the densely populated Indo-Gangetic Plain (IGP) of India. We investigate the temporal variation in tropospheric columns, surface volume mixing ratio (VMR), and vertical profiles of aerosols, NO<sub>2</sub>, and HCHO and identify factors driving their ambient levels and distributions for the period from January 2013 to June 2017. We observed mean aerosol optical depth (AOD) at 360 nm, tropospheric NO<sub>2</sub> vertical column density (VCD), and tropospheric HCHO VCD for the measurement period to be  $0.63 \pm 0.51$ ,  $(6.7 \pm 4.1) \times 10^{15}$ , and  $(12.1 \pm 7.5) \times 10^{15}$  molecules cm<sup>-2</sup>, respectively. Concerning the tropospheric NO<sub>2</sub> VCDs, Mohali was found to be less polluted than urban and suburban locations of China and western countries, but comparable HCHO VCDs were observed. For the more than 4 years of measurements during which the region around the measurement location underwent significant urban development, we did not observe obvious annual trends in AOD, NO<sub>2</sub>, and HCHO. High tropospheric NO<sub>2</sub> VCDs were observed in periods with enhanced biomass and biofuel combustion (e.g. agricultural residue burning and domestic burning for heating). Highest tropospheric HCHO VCDs were observed in agricultural residue burning periods with favourable meteorological conditions for photochemical formation, which in previous studies have shown an implication for high ambient ozone also over the

IGP. Highest AOD is observed in the monsoon season, indicating possible hygroscopic growth of the aerosol particles. Most of the NO<sub>2</sub> is located close to the surface, whereas significant HCHO is present at higher altitudes up to 600 m during summer indicating active photochemistry at high altitudes. The vertical distribution of aerosol, NO<sub>2</sub>, and HCHO follows the change in boundary layer height (BLH), from the ERA5 dataset of European Centre for Medium-Range Weather Forecasts, between summer and winter. However, deep convection during the monsoon transports the pollutants at high altitudes similar to summer despite a shallow ERA5 BLH. Strong gradients in the vertical profiles of HCHO are observed during the months when primary anthropogenic sources dominate the formaldehyde production. High-resolution MODIS AOD measurements correlate well but were systematically higher than MAX-DOAS AODs. The ground-based MAX-DOAS measurements were used to evaluate three NO<sub>2</sub> data products and two HCHO data products of the Ozone Monitoring Instrument (OMI) for the first time over India and the IGP. NO<sub>2</sub> VCDs from OMI correlate reasonably with MAX-DOAS VCDs but are lower by ~ 30%–50% due to the difference in vertical sensitivities and the rather large OMI footprint. OMI HCHO VCDs exceeded the MAX-DOAS VCDs by up to 30%. We show that there is significant scope for improvement in the a priori vertical profiles of trace gases, which are used in OMI retrievals. The difference in vertical representativeness was found to be crucial for the observed biases in NO<sub>2</sub> and HCHO surface VMR intercomparisons. Using the ratio of NO<sub>2</sub> and HCHO

VCDs measured from MAX-DOAS, we have found that the peak daytime ozone production regime is sensitive to both NO<sub>x</sub> and VOCs in winter but strongly sensitive to NO<sub>x</sub> in other seasons.

## 1 Introduction

Air pollution is a serious issue in south Asia with the Indo-Gangetic Plain (IGP) being one of the hotspots of both present and future forecasts (Giles, 2005). For example, over the IGP, the ambient air quality standards of several criteria air pollutants (e.g. ozone, PM<sub>10</sub>, and PM<sub>2.5</sub>) are violated for more than 60 % of the days in a year (Pawar et al., 2015; Kumar et al., 2016). NO<sub>x</sub> (sum of NO and NO<sub>2</sub>) and volatile organic compounds (VOCs) are the precursors of ozone and secondary organic aerosols. Formaldehyde, the most abundant carbonyl compound in the atmosphere, is the primary source of HO<sub>2</sub> radicals in the troposphere, which in the presence of NO<sub>x</sub> can ramp up ozone production (Wolfe et al., 2016; Fortems-Cheiney et al., 2012). While NO<sub>x</sub> is a major anthropogenic primary pollutant, formaldehyde has both biogenic and anthropogenic sources and is mainly formed during the atmospheric oxidation of methane and VOCs (e.g. alkenes), a process that is related to the production of ozone in the troposphere. An increase in both NO<sub>2</sub> and HCHO over India with an average annual rate of 2.2 % and 1.5 % per year, respectively, was documented using more than 15 years of dataset from multiple satellite instruments (Mahajan et al., 2015). Significant spatial and seasonal variabilities in NO<sub>2</sub> and HCHO were shown in these studies, but their maximum tropospheric columns were observed over the IGP.

Differential optical absorption spectroscopy (DOAS) (Platt, 1994), a technique based on the Beer–Lambert's law, has found its versatile application in the last 2 decades for remote sensing of tropospheric pollutants including aerosol, NO<sub>2</sub>, and HCHO from both ground-based and space-borne platforms. Ground-based multi-axis (MAX-) DOAS instruments provide continuous measurements of trace gases and aerosol including their vertical profile by observing scattered sunlight at different, mostly slant, elevation angles (Hönninger et al., 2004; Wagner et al., 2011, 2004; Sinreich et al., 2005). One of the significant advantages of this technique is that, from one spectrum, many atmospheric constituents (e.g. aerosol, NO<sub>2</sub>, HCHO, BrO, glyoxal, HONO, oxygen dimer (O<sub>4</sub>), SO<sub>2</sub>, and water vapour) can be quantified. Another advantage of the MAX-DOAS technique is that it does not require a radiometric calibration and can be operated autonomously even in very remote locations. Due to their simple design, the vast applicability for the detection of multiple atmospheric constituents, low power demand, minimal maintenance, possible automation, and remote access, MAX-DOAS instruments have been extensively employed both for long-term monitoring (Ma et al., 2013; Chan et al., 2019;

Wang et al., 2017a, b) and extensive fields campaigns (Li et al., 2013; Heckel et al., 2005; Schreier et al., 2020; Halla et al., 2011) over the last decade. These measurements have been used for characterization of pollution and its source attribution (Wang et al., 2014), emission strength (Shaiganfar et al., 2017, 2011), chemistry, and transport (MacDonald et al., 2012) and for the validation of satellite observations (Wang et al., 2017a; Drosoglou et al., 2017; Mendolia et al., 2013). Over India, ground-based measurements of trace gases are limited primarily to in situ measurements (e.g. Gaur et al., 2014; Sinha et al., 2014; Kumar et al., 2016), whereas MAX-DOAS measurement of trace gases (e.g. NO<sub>2</sub>, HCHO) and aerosol have rarely been reported. The few studies are limited only to 4 d of mobile measurement around Delhi (Shaiganfar et al., 2011) for an estimation of NO<sub>x</sub> emission from Delhi and satellite validation and more recently to a suburban site Pantnagar (29.03° N, 79.47° E) (Hoque et al., 2018) and a rural site Barkachha (25.06° N, 82.59° E) in the Indo-Gangetic Plain (Biswas et al., 2019). Though in situ techniques provide crucial continuous measurements of targeted atmospheric pollutants (e.g. NO<sub>x</sub>, O<sub>3</sub>, aerosol, and VOCs), logistical constraints in their setup and maintenance limit their spatial and temporal coverage. Unless specifically designed inlets are used to alternate between different altitudes or mounted on aircraft or balloons, these measurements also lack the information about vertical profiles.

The DOAS principle has also been applied to the backscattered signal measured in the UV and visible wavelengths by several sun-synchronous satellite instruments to provide almost daily global coverage of the spatial distribution of aerosol (Torres et al., 2007; Levy et al., 2013), NO<sub>2</sub> (Boersma et al., 2011), formaldehyde (González Abad et al., 2015; Zara et al., 2018), and several other trace gases (González Abad et al., 2019) for more than 2 decades. Satellite observations of NO<sub>2</sub> and HCHO have been extensively used for a variety of applications ranging from (but not limited to) validating chemistry transport models in various atmospheric environments, the assessment of bottom-up emission inventories, assessing seasonal and long-term trends, constraining emission strength on NO<sub>x</sub> sources, the lifetime of NO<sub>x</sub> (Beirle et al., 2011; Huijnen et al., 2010; Ma et al., 2013; Chan et al., 2019), and VOC emissions trends, characterization, and their source contribution (Kaiser et al., 2018; Zhu et al., 2017; Fu et al., 2007). Satellite observations over India have been employed to study long-term trends and the spatial distribution of NO<sub>2</sub> and HCHO and trends in NO<sub>x</sub> emissions (Ghude et al., 2008, 2013; Mahajan et al., 2015; Hilboll et al., 2013) and to investigate important processes contributing to HCHO formation and constraining the VOC emissions (Chaliyakunnel et al., 2019; Surl et al., 2018).

Despite their attractive spatial coverage, satellite observations have their inherent uncertainties, arising from the retrieval algorithm, the presence of clouds, the underlying assumption for calculations of a priori profiles, air mass factors, and background corrections. For example, satellite mea-

measurements of trace gases located close to the surface usually underestimate the actual values around megacities due to the so-called aerosol shielding and gradient smoothing effect (Ma et al., 2013). Ground-based remote-sensing techniques, e.g. MAX-DOAS, have proved instrumental for the validation of satellite measurements (Wang et al., 2017a; Jin et al., 2016; Ma et al., 2013; Schreier et al., 2020; Mendolia et al., 2013; Irie et al., 2008; Brinksma et al., 2008). In addition to validation, MAX-DOAS measurements complement satellite observations by providing information about the diurnal and vertical profiles of trace gases and aerosol. Additionally, the MAX-DOAS observations also have the potential to bridge the gap between the scales of in situ and satellite observations as the former are more sensitive to concentration close to their inlet, whereas the latter are representative of a larger area up to few hundred square kilometres.

Over India, the application of ground-based remote-sensing techniques for the validation of atmospheric chemistry and composition observations is majorly limited for aerosol measurements, except for the study by Shaiganfar et al. (2011) using 4 d of mobile measurements. Over polluted regions, the Ozone Monitoring Instrument (OMI) was found to underestimate the NO<sub>2</sub> vertical column densities (VCDs), while the inverse was observed for clean regions. Sun photometers have been used in the past to validate MODIS aerosol optical depth (AOD) measurements (Tripathi et al., 2005; Mhawish et al., 2019). Considering the spatial and temporal variation in emission sources over all of India, there is an urgent need for the validation of satellite observations of trace gases with ground-based remote-sensing measurements. Even though several in situ measurements of NO<sub>2</sub> have been reported over India, the fundamental difference in the retrieved information for satellite and in situ measurements (VCD and surface concentration) also precludes a direct intercomparison. The two stationary MAX-DOAS measurements so far over India focussed primarily on surface volume mixing ratios (VMRs) and have not reported the VCDs of trace gases, and hence they lack intercomparison with the satellite observation. To the best of our knowledge, so far there have not been any measurements probing the vertical distribution of NO<sub>2</sub> and formaldehyde over India, which limits the understanding of vertical transport of pollutants at various temporal scales (diurnal or seasonal). Moreover, the retrieved profile results close to the surface can also be compared to in situ measurements.

In this paper, we present more than 4 years (January 2013–June 2017) of MAX-DOAS measurements of AOD, NO<sub>2</sub>, and HCHO vertical column densities, vertical profiles, and surface concentration (extinction) from Mohali in the north-west IGP and investigate the factors driving these parameters. We perform a detailed comparison of several NO<sub>2</sub>, HCHO, and AOD data products of OMI and MAIAC (Multi-Angle Implementation of Atmospheric Correction) AOD data product of MODIS with MAX-DOAS measurements and discuss the discrepancies. The ratio of NO<sub>2</sub> and formaldehyde was

employed to investigate whether NO<sub>x</sub> or VOC drives ozone production in different seasons. The volume mixing ratios of NO<sub>2</sub> and HCHO close to the surface were evaluated with in situ measurements to understand the spatial representativeness of both the measurements.

## 2 Experimental and data analyses

### 2.1 Site description

Here, we report the measurements and satellite observations from a suburban site, Mohali, located in the north-west Indo-Gangetic Plain. Figure 1 shows the location of Mohali, major cities, and a terrain map around North India. We also show the spatial distribution of mean NO<sub>2</sub> tropospheric vertical column densities probed by the TROPOMI satellite (van Geffen et al., 2017; Veeffkind et al., 2012) for the period December 2017–October 2018 in a 25 km × 25 km box around Mohali. The Himalayan mountain range starts at ~ 35 km in the north. The in situ and ground-based remote-sensing measurements were performed at the IISER (Sinha et al., 2014) Mohali atmospheric chemistry facility (30.667° N, 76.739° E; 310 m a.m.s.l.). A detailed description of the site including the seasonal characteristic of meteorological parameters, characteristic wind sectors, and major emissions can be found elsewhere (Kumar et al., 2016; Pawar et al., 2015; Sinha et al., 2014). The urban city Chandigarh is located in the wind sector spanning from north to east, while the west and south are comprised mostly of agricultural lands and small cities or towns. Two major power plants are located within 50 km of the measurement site. At ~ 45 km to the north-west (~ 342°) is the 1260 MW Guru Gobind Singh super thermal power plant (PP1), Rupnagar, which was operational with 90 % of its capacity until 2014. Since February 2014, a 1400 MW power plant (PP2) has been functional in Rajpura, which is ~ 18 km south-west (~ 230°) of the measurement site.

For the climate of India, the year can be divided into the following four seasons: winter (November to February), summer (March–June), monsoon (July–August), and post-monsoon (September–October). Large-scale crop residue burning events occur in the late summer and late post-monsoon, which strongly perturb the atmospheric chemistry and composition (Kumar et al., 2018; Sarkar et al., 2013). In order to account for these perturbations, Kumar et al. (2016) have recommended a further classification of summer and post-monsoon months into clean and polluted periods. The primary fetch region of the air masses is north-west throughout the year except in the monsoon season, when the wind direction is primarily south-east. Figure F1 shows the wind rose plots indicating the wind speed and wind direction frequencies around Mohali in the four major seasons over the measurement period. Over the years 2012–2017, rapid urbanization has happened in Mohali and nearby regions

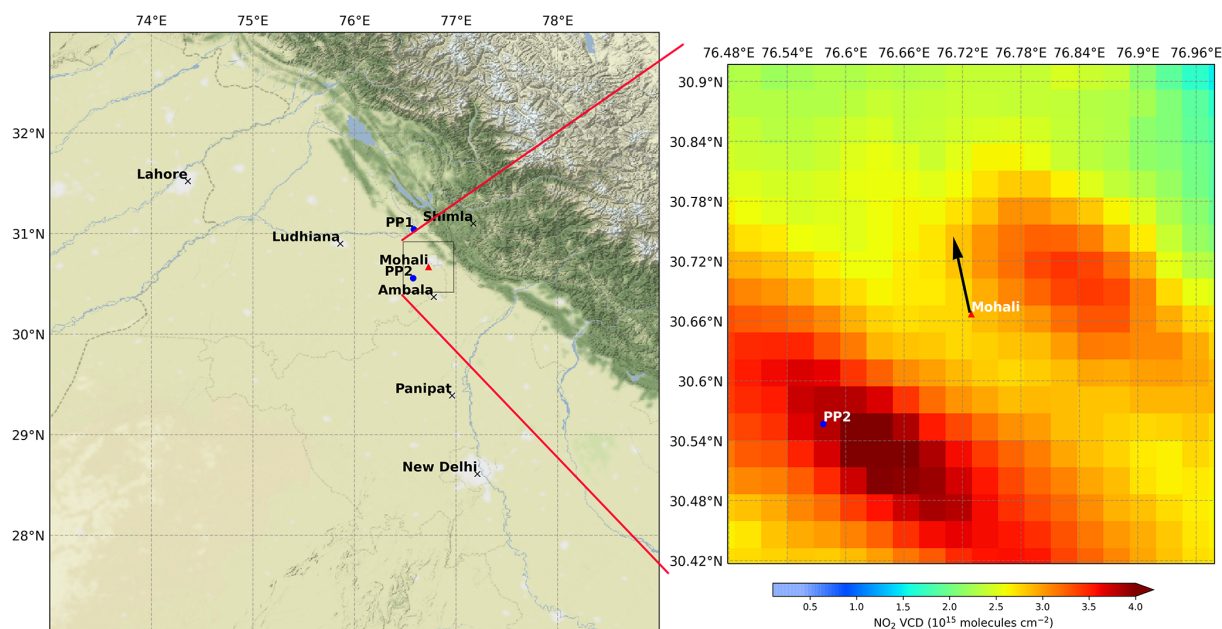


**Figure 1.** Left: terrain map showing the location of Mohali (red triangle) in North India, along with major cities (crosses) and two major thermal power plants near Mohali (blue circles: PP1 – Guru Gobind Singh super thermal power plant; PP2 – Larsen & Toubro super thermal power plant (NPL), Rajpura) and province boundaries. Right: mean tropospheric NO<sub>2</sub> VCD measured by TROPOMI overlaid on the terrain map of a  $0.5^\circ \times 0.5^\circ$  box around Mohali (shown in the left panel) for the period December 2017–October 2018. The black arrow indicates the viewing direction of the MAX-DOAS instrument. Terrain maps are adapted from Stamen (<http://maps.stamen.com/terrain>, last access: 17 November 2020).

(e.g. the commissioning of new international airport terminal and highways, extended construction activities for residential (e.g. Aero city, ECO city) and institutional (Knowledge City, Medicity) purposes). According to the census of 2011, the district of Mohali holds the top rank in urban population growth among all districts in the state of Punjab at a rate of 90.2 % for the period between the years 2001 and 2011 (Tripathi and Mahey, 2017).

## 2.2 MAX-DOAS measurement setup and spectral analysis

A MAX-DOAS instrument (Hoffmann Messtechnik GmbH) was installed at ca. 20 m above ground level with an azimuth viewing direction of  $10^\circ$  anticlockwise from the north. The instrument primarily consists of a Czerny Turner spectrometer (Ocean Optics USB 2000+), an optical assembly consisting of a quartz lens that collects the scattered sunlight, quartz optical fibre that transmits the light to the spectrometer, and electronics in a sealed metal box. The box is mounted on a stepper motor which can be programmed to set the elevation viewing angle of the instrument. The spectral resolution of the spectrometer was  $\sim 0.7$  nm in the spectral range of 318–465 nm with a field of view (FOV) of  $0.7^\circ$ . In order to avoid light outside the telescope's FOV being scattered onto the fibre, a black tube (ca. 6 cm long) was mounted in front of the lens. The scattered sunlight spectra were recorded for el-

evation viewing angles 1, 2, 4, 6, 8, 10, 15, 30, and  $90^\circ$  at a total integration time (number of scans  $\times$  acquisition time for one scan) of 60 s each. Since the complete MAX-DOAS instrument was mounted outside, it was important to adjust the detector temperature so that the following two conditions are met:

1. The detector temperature is lower than the ambient temperature.
2. The difference between the ambient temperature and detector temperature is not more than  $20^\circ$  C. This ensures that the workload on the Peltier cooler is manageable and the detector temperature is stable.

Hence, depending on the seasons, the detector temperature was adjusted. Figure F2 shows the nominal detector temperatures ( $T_{\text{set}}$ ) and actual detector temperature ( $T_{\text{cold}}$ ) for the various periods during the measurement period. The dark current and offset spectra were recorded every night, and while performing the spectral analysis, these were subtracted from the measured spectra recorded at a similar detector temperature. Additional offset was corrected from the measured spectrum accounting for the mean intensity recorded by the dark pixels (pixel nos. 1–6 among the 2048 pixels) of the spectrometer. Wavelength-to-pixel calibrations were performed in the QDOAS software (<http://uv-vis.aeronomie.be/software/QDOAS/>, last access: 20 November 2020) (Danck-

aert et al., 2012) every time the detector temperature was changed, by matching the structures in a measured spectrum in the zenith direction at around noontime with those in a highly resolved solar spectrum. Horizon scans were performed every day at around 12:00 local time (LT). Figure F3 shows a typical variation in measured intensity and its derivatives at three different wavelengths over an elevation angle range from  $-3$  to  $3^\circ$ . A steep increase was observed in the measured intensity, which was centred between  $0$  and  $0.3^\circ$  for various wavelengths chosen for analysing the horizon scan. During the period of measurement, the horizon in the viewing direction was determined by a residential building with a height of about  $40$  m at a distance of  $3$  km. The viewing angle of this visible horizon would be about  $0.38^\circ$  in good agreement with the results from the elevation scan. Thus we did not need to perform any correction for the true horizon in further analyses (Donner et al., 2020). We also see from Fig. F3 that the FOV of the instrument is rather large ( $>0.7^\circ$ ), and typically the root mean square (rms) of the spectral analysis for the measurements at  $1^\circ$  elevation is substantially larger than those for the higher-elevation angles. Hence, we excluded the measurements at  $1^\circ$  elevation angle from further analyses.

The measured spectra of the scattered sunlight were analysed for NO<sub>2</sub>, HCHO, and the oxygen dimer (O<sub>4</sub>) using the QDOAS software. Table 1 lists the wavelength intervals, included cross sections and other relevant details pertaining to the different retrievals, and Fig. 2 shows example DOAS fits and residuals for these retrievals. The typical values (peak of the frequency distribution) of the rms of the DOAS fit residuals are around  $5 \times 10^{-4}$ ,  $7 \times 10^{-4}$ ,  $6 \times 10^{-4}$ , and  $6 \times 10^{-4}$  for O<sub>4</sub>, NO<sub>2</sub> (UV), NO<sub>2</sub> (VIS), and HCHO, respectively. In order to retain analysis results corresponding to good-quality fits, we have excluded the O<sub>4</sub>, NO<sub>2</sub>, and HCHO differential slant column densities (dSCDs) corresponding to an rms greater than  $2 \times 10^{-3}$  and solar zenith angles higher than  $85^\circ$  (Wang et al., 2019). The rms threshold removes 1.1 %, 1.4 %, 0.7 %, and 1.3 % of the O<sub>4</sub>, NO<sub>2</sub> (UV), NO<sub>2</sub> (VIS) and HCHO dSCDs, respectively, of all the measured dSCDs at solar zenith angles less than  $85^\circ$ .

The spectral analysis is performed with respect to a Fraunhofer reference spectrum (FRS) measured in the zenith direction of each complete elevation angle measurement sequence in order to account for the Fraunhofer lines and the stratospheric contribution of the absorbers (Hönninger et al., 2004). For analysing the off-axis spectra measured at time “ $t$ ”, we calculate the FRS at the time of the measurement by interpolating the zenith spectra measured before and after the complete measurement sequence. Thus, the primary retrieved quantity from MAX-DOAS spectral analysis is the so-called dSCD. dSCD of a trace gas (absorber) at an elevation angle  $\alpha$  can be regarded as the difference between the absorber concentration integrated along the photon path at

elevation angle  $\alpha$  (SCD <sub>$\alpha$</sub> ) and zenith direction (SCD<sub>90</sub>).

$$\text{dSCD}_\alpha = \text{SCD}_\alpha - \text{SCD}_{90} \quad (1)$$

dSCD is related to the tropospheric VCD through differential air mass factors (dAMF or AMF <sub>$\alpha$</sub>  – AMF<sub>90</sub>):

$$\text{VCD} = \frac{\text{dSCD}}{\text{dAMF}}. \quad (2)$$

Unless specifically mentioned, we will use VCD to refer to tropospheric VCDs in the paper hereafter. The air mass factors are related to the light path of the photons reaching the telescope of the instrument and depend on several parameters, e.g. elevation angle, solar zenith angle, relative solar azimuth angle with respect to the instrument, surface reflectance, aerosol and trace gas vertical profile, and aerosol optical properties. In Sect. 2.4, we provide the details of the calculation of air mass factors and subsequent profile inversion to retrieve the VCDs and vertical profiles.

DOAS retrievals of NO<sub>2</sub> can be performed both in the UV and visible wavelength windows but have their respective advantages and limitations. NO<sub>2</sub> has a stronger absorption in the visible as compared to UV. Hence, the DOAS fit in the visible results in smaller fit uncertainties as compared to that in the UV (Fig. A1). This is an important aspect, especially for instruments with rather low quantum efficiencies like the detector of the MAX-DOAS instrument used in this study. However, the profile inversion methods (please refer to Sect. 2.4) to retrieve NO<sub>2</sub> vertical profiles and VCDs also require information about aerosol extinction profiles at the same wavelength as that used for NO<sub>2</sub> retrieval. The aerosol extinction profile retrieval for DOAS relies on the O<sub>4</sub> measurements, which have a rather weaker absorption at the visible wavelengths (in the spectral range of our instrument). Hence an alternative approach is to use an Ångström exponent to scale the aerosol extinction profiles derived at UV wavelengths to visible wavelengths. The aerosol extinction profiles calculated for the visible wavelength are subsequently used as an input parameter for the NO<sub>2</sub> profile inversion in the visible window. In Appendix A, we compare the performance and internal consistency of the NO<sub>2</sub> profiles and VCDs retrieved in the UV and visible by the profile inversion algorithm and by the geometric approximation under various sky conditions. Briefly, we found very good agreement between the NO<sub>2</sub> VCDs retrieved in the UV and visible under clear-sky conditions with a low aerosol load (slope = 0.95 and  $r = 0.9$ ). Even in the clear-sky case with high aerosol load and cloudy-sky conditions, a reasonable agreement for NO<sub>2</sub> VCDs between the retrieval in UV and visible was observed (slope = 0.75 and 0.78 for high aerosol and cloudy cases, respectively;  $r = 0.82$  for both). The NO<sub>2</sub> dSCDs from the retrieval in the UV wavelength window were found to be in good agreement with those retrieved in the visible, but they were systematically lower ( $r = 0.9$ , slope = 0.95 and a negative offset of  $1.1 \times 10^{14}$  molecules cm<sup>-2</sup>).

**Table 1.** Spectral analysis settings and considered cross sections in QDOAS for the retrieval of dSCDs of NO<sub>2</sub> (in UV and Vis), HCHO, and O<sub>4</sub>.

Species	NO <sub>2</sub> (UV)	NO <sub>2</sub> (Vis)	HCHO	O <sub>4</sub>
Fit window	338–370 nm	400–460 nm	336.5–359 nm	352–387 nm
Fitted absorption cross sections	NO <sub>2</sub> (298 K with $I_o$ correction corresponding to an SCD of $10^{17}$ molecules $\text{cm}^{-2}$ ) <sup>1</sup> , NO <sub>2</sub> (220 K pre-orthogonalized to NO <sub>2</sub> cross section at 298 K) <sup>1</sup> , HCHO (297 K) <sup>2</sup> , O <sub>3</sub> (223 K with $I_o$ correction corresponding to an SCD of $10^{20}$ molecules $\text{cm}^{-2}$ ) <sup>3</sup> , BrO (223 K) <sup>4</sup> , O <sub>4</sub> (293 K) <sup>5</sup> , Ring	NO <sub>2</sub> (298 K with $I_o$ correction corresponding to an SCD of $10^{17}$ molecules $\text{cm}^{-2}$ ) <sup>1</sup> , H <sub>2</sub> O (296 K) <sup>6</sup> , O <sub>3</sub> (223 K with $I_o$ correction corresponding to an SCD of $10^{20}$ molecules $\text{cm}^{-2}$ ) <sup>3</sup> , O <sub>4</sub> (293 K) <sup>5</sup> , Ring	HCHO (297 K) <sup>2</sup> , BrO (223 K) <sup>4</sup> , O <sub>3</sub> (223 K with $I_o$ correction corresponding to an SCD of $10^{20}$ molecules $\text{cm}^{-2}$ ) <sup>3</sup> , NO <sub>2</sub> (298 K with $I_o$ correction corresponding to an SCD of $10^{17}$ molecules $\text{cm}^{-2}$ ) <sup>1</sup> , O <sub>4</sub> (293 K) <sup>5</sup> , Ring	O <sub>4</sub> (293 K) <sup>5</sup> , NO <sub>2</sub> (298 K with $I_o$ correction corresponding to an SCD of $10^{17}$ molecules $\text{cm}^{-2}$ ) <sup>1</sup> , HCHO (297 K) <sup>2</sup> , O <sub>3</sub> (223 K with $I_o$ correction corresponding to an SCD of $10^{20}$ molecules $\text{cm}^{-2}$ ) <sup>3</sup> , BrO (223 K) <sup>4</sup> , Ring
Polynomial order	5	5	5	5
Intensity offset	Constant and first order	Constant and first order	Constant and first order	Constant, first, and second order
Fraunhofer reference selection	Sequential	Sequential	Sequential	Sequential
Shift and stretch	Spectrum	Spectrum	Spectrum	Spectrum

<sup>1</sup> Vandaele et al. (1998). <sup>2</sup> Meller and Moortgat (2000). <sup>3</sup> Serdyuchenko et al. (2014). <sup>4</sup> Fleischmann et al. (2004). <sup>5</sup> Thalman and Volkamer (2013). <sup>6</sup> Rothman et al. (2010).

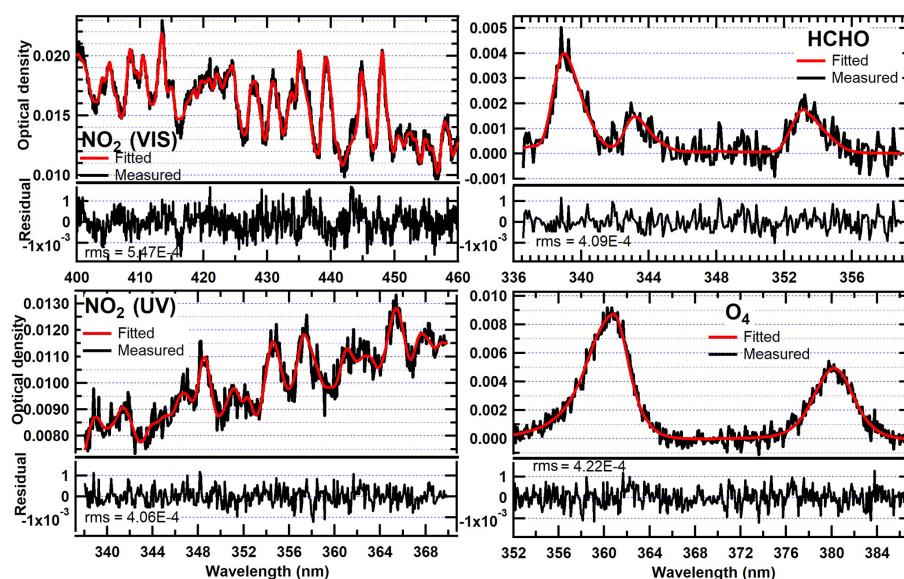


**Figure 2.** Example DOAS fits and residuals for NO<sub>2</sub> in the visible (dSCD =  $2.91 \times 10^{16} \pm 2.89 \times 10^{14}$  molecules  $\text{cm}^{-2}$ ) and UV (dSCD =  $2.09 \times 10^{16} \pm 8.17 \times 10^{14}$  molecules  $\text{cm}^{-2}$ ), HCHO (dSCD =  $7.23 \times 10^{16} \pm 4.32 \times 10^{15}$  molecules  $\text{cm}^{-2}$ ), and O<sub>4</sub> (dSCD =  $2.06 \times 10^{43} \pm 4.25 \times 10^{41}$  molecules<sup>2</sup>  $\text{cm}^{-5}$ ) for a typical spectrum measured on 26 July 2015 at a solar zenith angle of 20° and 2° elevation angle.

### 2.3 Cloud classification

Clouds have a strong impact on MAX-DOAS measurements and subsequent profile inversion as they alter the light path and intensity (Wagner et al., 2014, 2011). Clouds are generally not included within the radiative transfer models for profile inversion. The cloud classification scheme is based on the measured radiances at 360 nm, the colour index (ratio of measured radiances at 330 and 390 nm), and the measured O<sub>4</sub> air mass factors (O<sub>4</sub> slant column density (SCD)/O<sub>4</sub> VCD) (for details see Wagner et al., 2016). Besides the absolute values of these quantities, their temporal variation and their elevation dependencies are also considered. The threshold for these quantities (the spread of O<sub>4</sub>, the normalized CI, the spread of the CI, and the temporal variation in the CI) are parameterized as polynomials of the SZA as provided in Wagner et al. (2016). We can classify the sky conditions into the following seven categories: (1) clear sky with low aerosol load, (2) clear sky with high aerosol load (AOD > 0.85 at 330 nm), (3) broken clouds, (4) cloud holes, (5) continuous clouds, (6) fog, and (7) optically thick clouds (Wagner et al., 2014, 2016). In the first step, using the colour index (CI), its variation across the zenith spectrum for an adjacent elevation sequence, and its variation within an elevation sequence, the primary cloud classification is performed to retrieve information about primary conditions (types 1–5). The identification of fog and thick clouds is performed in the second step using the O<sub>4</sub> air mass factor (AMF) and measured radiance at 360 nm. Fog is identified if there is very little variation in O<sub>4</sub> dSCD for different elevation angles within the measurement sequence. The details pertaining to the calculation of thresholds for radiance for the identification of thick clouds are provided in Appendix B. While the classification of aerosols might be slightly affected by the specific properties of the local aerosol, the cloud classification is robust to the variability of aerosol properties. However, this is not critical here because the main aim – the cloud classification – is hardly affected by these specific aerosol properties.

Figure 3 shows the percentage of the mean monthly sky condition for the complete measurement period. The most prominent sky condition in all the seasons is “clear sky with high aerosol load”, comprising ~ 48 % of the total. March and April are marked by the maximum occurrence of clear-sky conditions with low aerosol load at ~ 18 %. Continuous clouds and optically thick clouds are most abundant in July–August, which is marked by the monsoon season. Please note that due to the widespread crop residue burning and suppressed meteorological conditions, the months of October and November witness severe smog events in the north-west Indo-Gangetic Plain leading to very poor air quality and low visibility. The poor air quality conditions extend until December due to emission from domestic burning for heating and similar meteorological conditions. The prevalent high aerosol load conditions are also marked by the cloud classification algorithm as seen by occurrences greater than 55 % in

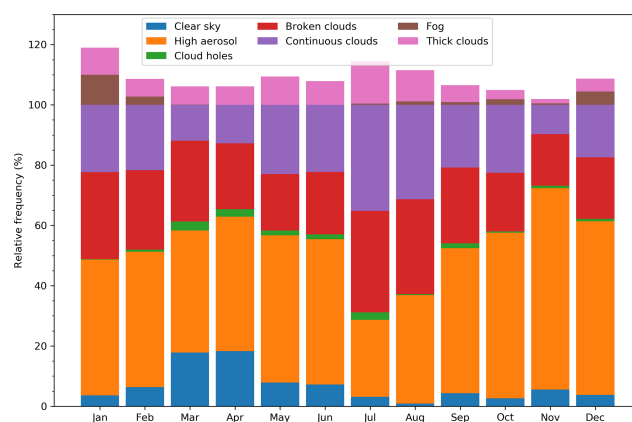


**Figure 3.** Relative frequencies of occurrence of various sky conditions in different months of the year over Mohali as derived from 4.5 years of MAX-DOAS observations. Note that the secondary cloud classifications of fog and optically thick clouds are not mutually independent and exclusive of the primary classification (clear sky, clear sky with high aerosol load, broken clouds, cloud holes, and continuous clouds). Hence, these are shown separately above the 100 % mark.

October, November, and December. Fog is observed in December and January, when winter is at its peak.

### 2.4 Profile inversion to retrieve vertical profiles and vertical column densities from slant column densities

In order to account for the complex dependence of air mass factors on viewing geometry and measurement conditions, radiative transfer models (e.g. McARTIM; Deutschmann et al., 2011) are employed. dAMFs are calculated for various combinations (nodes) of viewing geometry and profiles (of trace gases and aerosol), which are stored offline as multi-dimensional lookup tables (LUTs) for various wavelengths (e.g. separate LUTs for 343, 360 and 430 nm). Profile inversion techniques use these LUTs to determine the scenarios which best match the measured dSCDs. From these scenarios, the aerosol and trace gas profiles, VCDs, and AOD are derived.

We have used MAPA (Mainz Profile algorithm) (Beirle et al., 2019) version 0.98 for this purpose. The vertical profiles of trace gas concentrations (or aerosol extinction) can be parameterized using three profile parameters namely column parameters ( $c$ ) (VCD for trace gases and AOD for aerosol), height parameter ( $h$ ), and shape parameter ( $s$ ) (Beirle et al., 2019; Wagner et al., 2011). In the first step, the aerosol profiles are retrieved using the measured O<sub>4</sub> dSCDs. A Monte Carlo approach is utilized to identify the best ensemble of the forward model parameters ( $h$ ,  $s$  and  $c$ ) which fit the measured O<sub>4</sub> dSCDs for the sequence of elevation angles. Generally, a scaling factor (0.8 in most of the cases) is applied to the measured O<sub>4</sub> dSCDs before they are used in the pro-

file retrieval (see Wagner et al., 2019, and references therein). The reason for this scaling factor is still not understood, and in Sect. 3.3, we also investigate the effect of the different scaling factors on the intercomparison of the retrieved AOD with satellite observation from MODIS. In the second step, the aerosol profiles retrieved from the O<sub>4</sub> inversion are used as input to retrieve similar model parameters ( $h$ ,  $s$ , and  $c$ ) for the trace gases (e.g. NO<sub>2</sub> and HCHO). To assess the quality of the retrievals, MAPA also provides “valid”, “warning”, or “error” flags for each measurement sequence, which are calculated based on pre-defined thresholds for various fit parameters (Beirle et al., 2019). We have used the lookup tables calculated at 360 nm for the inversion of O<sub>4</sub> and NO<sub>2</sub> in the UV and 343 nm for HCHO and 430 nm for NO<sub>2</sub> in the visible window. For the HCHO profile inversion, we observed unrealistic  $h$  and  $s$  at high solar zenith angles (SZA > 60°), which are probably related to spectral interferences with the ozone absorption within the DOAS analysis. Therefore, we only consider HCHO profile results for measurements with an SZA of less than 60°. For the retrieval of NO<sub>2</sub> in the visible wavelength window and HCHO, the aerosol extinction profiles retrieved at 360 nm were scaled to those at 430 and 343 nm using an Ångström exponent of 1.54. This value was derived as the mean of the Ångström exponent (AE) between 470 and 550 nm measured by MODIS for the measurement period, where we do not observe a strong intra-annual variation (Fig. F4). We have calculated the AE using the measured AOD at 470 and 550 nm according to

$$AE = -\frac{\log(AOD_{470}/AOD_{550})}{\log(470/550)}. \quad (3)$$

We also investigated the effect of the choice of Ångström exponent on the profile inversion for a smaller subset of our data spanning 15 d. We found that AE values of 1.25 and 1.75 (minimum 5th percentile and maximum 95th percentile in Fig. F4) resulted in the same retrievals and the difference in the mean NO<sub>2</sub> VCD was less than 0.1 %. The surface NO<sub>2</sub> concentrations were slightly higher (4 %) for an AE value of 1.25 and were 3 % lower for an AE value of 1.75 as compared to those for an AE value of 1.54.

For the profile inversion using MAPA, we compare the number of valid and those retrievals flagged as warning and error in Table 2. We note that the sky conditions associated with thick clouds and fog are mostly flagged as errors in the profile inversion. For the analysis results shown in the paper hereafter, we only retained the DOAS measurements corresponding to sky conditions without thick clouds and fog.

## 2.5 Satellite data

### 2.5.1 OMI

OMI aboard the AURA satellite crosses the Equator at 13:42 local solar time in the ascending orbit. OMI has an effective ground pixel size of 13 × 24 km<sup>2</sup> at nadir view, which

broadens up to 13 × 150 km<sup>2</sup> at the swath edges (Levelt et al., 2006; Schenkeveld et al., 2017). The intensity of backscattered solar radiation from the Earth's atmosphere is measured by two spectrometers in three bands in the spectral ranges of 260–311, 307–383, and 349–503 nm. With an across-track swath width of ~ 2600 km, OMI provides daily coverage of the Earth in 14 orbits. Several data products of AOD, NO<sub>2</sub>, and HCHO retrieved from OMI measurements are available, which we briefly describe in Appendix C and compare against MAX-DOAS observation in the subsequent sections. From the level 2 data corresponding to individual orbits every day, we have retained the data pertaining to the centre of the ground pixel within 0.25° × 0.25° of the measurement site. For sensitivity analysis, we have also separately selected the collocated pixels, i.e. OMI pixels whose corner points contained the exact location of the measurement location. Ground pixels with an effective cloud fraction > 0.3 or measurements affected by the so-called row anomaly and problems in the DOAS retrieval were filtered out for the analysis. In order to minimize the effect of the diurnal variation, we have only chosen the MAX-DOAS measurements between 07:00 and 09:00 UTC (between 12:30 and 14:30 LT) for comparison with OMI observations. We have used the OMAERUV data product for AOD, the DOMINO V2, OMNO2 v3.0, and the QA4ECV data products for NO<sub>2</sub>, and the OMHCHO and QA4ECV data products for HCHO for the evaluation with the corresponding MAX-DOAS retrieved quantities (see Appendix C for the details of the satellite data products). The retrieval and quality control details pertaining to these data products are provided in Appendix C.

### 2.5.2 MODIS

Satellite measurements of the AOD were also obtained from the MODIS instruments on-board the TERRA and AQUA satellites having Equator overpasses at local solar times 10:30 and 13:30, respectively. We have used the MAIAC data product available at 1 × 1 km<sup>2</sup> spatial resolution (Lyapustin et al., 2018). Since MAIAC is a combined product of MODIS TERRA and AQUA, we have chosen the daily means of the DOAS measurements between 9:30 and 11:30 and between 12:30 and 14:30 LT for the intercomparison.

## 2.6 Ancillary measurements

In situ measurements of NO<sub>x</sub> (NO and NO<sub>2</sub>) were performed using a model 42i trace level analyser (Thermo Fischer Scientific) based on the chemiluminescence technique. Ambient NO<sub>2</sub> is first converted into NO using a heated molybdenum converter, which further reacts with excess ozone generated inside the instrument to produce a chemiluminescence signal proportional to the available NO. Checks for zero drifts were performed every week, and five point calibrations were performed every month. Meteorological parameters (e.g. ambient temperature, rainfall, wind speed, wind direction, and

**Table 2.** Frequency of MAPA retrievals flagged as “valid”, “warning”, or “error” for various species and different sky conditions.

	All-sky conditions ( $n = 63\,107$ )				Condition except for thick clouds and fog ( $n = 58\,209$ )			
	O <sub>4</sub>	NO <sub>2</sub> (UV)*	NO <sub>2</sub> (VIS)	HCHO	O <sub>4</sub>	NO <sub>2</sub> (UV)*	NO <sub>2</sub> (VIS)	HCHO
Valid	27530	24287	24981	21671	27096	23899	24637	21462
Warning	10281	12893	12634	15491	9699	12304	11981	14758
Error	25296	25927	25492	25945	21414	22006	21591	21989

\* The number of valid retrievals for NO<sub>2</sub> (UV) is calculated using relaxed rms flag criteria (Appendix A).

relative humidity) were measured using collocated met sensors (Met One Instruments Inc.). The details pertaining to the measurements’ principle and calibration protocol can be found elsewhere (Sinha et al., 2014; Kumar et al., 2016).

In situ measurements of formaldehyde were performed at Mohali using a high-sensitivity proton transfer reaction mass spectrometer (PTR-MS) (Lindinger et al., 1998). Inside the PTR-MS, HCHO (proton affinity = 170.4 kcal mol<sup>-1</sup>) is chemically ionized by hydronium ions (H<sub>3</sub>O<sup>+</sup>) because of its higher proton affinity than that of water vapour (proton affinity = 165.2 kcal mol<sup>-1</sup>), prior to its detection using a quadrupole mass analyser. Using a PTR-MS, HCHO is detected at a protonated mass-to-charge ratio ( $m/z$ ) of 31. The measured signal (counts s<sup>-1</sup>) is converted to VMRs using the  $m/z$  dependent sensitivity factors, which are usually determined using calibration experiments. Due to the degradation of the detector, the sensitivity of PTR-MS might also change with time, which is evaluated using routine calibration performed using a gas standard of known VMR (Chandra and Sinha, 2016; Sinha et al., 2014). However, such a calibration for HCHO could not be performed due to the unavailability of a calibration standard. Hence, we have calculated theoretical sensitivity factors for HCHO, similar to the method incorporated by Kumar et al. (2018). The major sources of uncertainty in the HCHO measurements, when a theoretical sensitivity factor is used, are from (1) uncertainty in the proton transfer reaction rate constant of the reaction between HCHO and H<sub>3</sub>O<sup>+</sup> (~ 15 %) and (2) the ratio of transmission efficiencies of HCHOH<sup>+</sup> and H<sub>3</sub>O<sup>+</sup> (~ 25 %) (Zhao and Zhang, 2004; de Gouw and Warneke, 2007). Systematic uncertainties due to the degradation of the detector would increase with time. Ambient humidity is also known to interfere with the formaldehyde measurements with a PTR-MS, and we have performed an absolute humidity-based correction, according to Cui et al. (2016). HCHO VMRs increase by ~ 30 % on average after the application of the absolute humidity-based correction.

### 3 Results and discussion

#### 3.1 Seasonal and annual trends of AOD, NO<sub>2</sub>, and HCHO

Figure 4 shows the time series of monthly mean AOD, NO<sub>2</sub> VCD, and HCHO VCD for the complete measurement period from January 2013 until June 2017. The vertical error bars show the monthly variability as the interquartile range. The gaps in the time series are due to instrument malfunction (primarily due to the stepper motor and connection to the measurement computer). The mean AOD for the complete measurement period was  $0.63 \pm 0.51$ , with the monthly means varying between 0.30 in March 2013 and 1.25 in August 2014. We quantify the seasonal variability of the measured AOD to be 187 %, which is calculated as the difference between the maximum and minimum of the 30 d running mean divided by the mean over the measurement period. For the same months, very small inter-annual variability in the monthly means (<0.2) was observed for all the months except April–July. We observe the maximum AOD (0.8–1.2) during the monsoon months (June–August) at Mohali, which is most probably caused by the hygroscopic growth of the aerosol particles (Altaratz et al., 2013). Previous studies comparing various MODIS AOD data products and AERONET measurements over the Indo-Gangetic Plain have also found the maximum AOD in the monsoon months but also significant differences among the different data products (Mhawish et al., 2019; Tripathi et al., 2005). The retrieval of the aerosol size distribution from AERONET measurements has shown that during the monsoon, the coarse-mode fraction increases by more than 50 % of the annual average over the Indo-Gangetic Plain (Tripathi et al., 2005). In order to further confirm that the high AOD during the monsoon is not an artefact caused by the persistent cloud cover over the IGP, we have investigated the seasonality of the AOD under cloud-free conditions measured at different AERONET sites in the IGP nearest to Mohali (New Delhi ~ 250 km south and Lahore ~ 250 km west). Both at Lahore and New Delhi, high AOD values are observed in the monsoon months (June–August) (Fig. F5). Relatively high monthly mean AOD (0.6–0.9) values are also observed in May and October, which are characterized by crop residue fire emissions. We have also compared the MODIS AOD (converted to 440 nm using the

AE derived from Eq. (3) to the AERONET AOD at these two stations and found very good agreement in the daily measured values with Pearson correlation coefficients ( $r$ )  $> 0.84$  (Fig. F5) and an overall bias  $< 10\%$  for both sites.

The mean NO<sub>2</sub> VCD for the complete measurement period was  $(6.7 \pm 4.1) \times 10^{15}$  molecules cm<sup>-2</sup> with a variability in the monthly means between  $4.7 \times 10^{15}$  molecules cm<sup>-2</sup> in July 2015 and  $8.9 \times 10^{15}$  molecules cm<sup>-2</sup> in November 2013. The observed NO<sub>2</sub> VCDs are comparable to those observed in long-term measurements in rural and suburban environments (Kramer et al., 2008; Drosoglou et al., 2017) and satellite observations in the Indian metropolitan city Mumbai (Hilboll et al., 2013). These are much smaller than those observed in the urban areas worldwide (Mendolia et al., 2013; Drosoglou et al., 2017) or rural, suburban, and urban locations of China (Ma et al., 2013; Wang et al., 2017a; Chan et al., 2019; Jin et al., 2016; Vlemmix et al., 2015), where the mean monthly levels are generally higher than  $1 \times 10^{16}$  molecules cm<sup>-2</sup>. The observed seasonal variability of 145% in the 30 d running means can be explained by the seasonality of emissions and the changing lifetimes.

For NO<sub>2</sub>, we see that the monsoon months (July and August) are cleanest followed by early pre-monsoon months (March–April). The primary emission sources active throughout the year in and around the region are vehicular emissions, garbage burning, and biomass burning for cooking and construction activities. In the suburban and rural regions around the measurement site, biomass (e.g. wood, domestic, and agricultural residue) and biofuel (coal) burning serve as the primary source of heating. Increased emissions from biomass burning for domestic heating in winter when the atmospheric lifetime of NO<sub>2</sub> is at a maximum, marks the highest observed NO<sub>2</sub> VCDs in the year. Also, during the crop residue burning active periods of summer (May–June) and post-monsoon (October–November), we observe enhanced NO<sub>2</sub> VCDs. Notwithstanding the strong urbanization trends, a significant annual trend is not observed in either of the three parameters (AOD, NO<sub>2</sub>, and HCHO) measured by MAX-DOAS, indicating the dominance of non-organized emission sources, e.g. domestic heating, garbage burning, and crop residue burning for the  $\sim 4.5$ -year measurement period. This is further ascertained by the fact that we do not see any noticeable weekday–weekend dependence in either of NO<sub>2</sub>, HCHO, and AOD (Fig. F6).

The mean HCHO VCD for the complete measurement period was  $(12.1 \pm 7.5) \times 10^{15}$  molecules cm<sup>-2</sup>, with a strong seasonality with monthly means ranging from  $5.3 \times 10^{15}$  molecules cm<sup>-2</sup> in March 2017 to  $17.7 \times 10^{15}$  molecules cm<sup>-2</sup> in October 2015. The seasonal variability was found to be strongest at 284% for HCHO among the three parameters measured by MAX-DOAS. The mean and monthly variability is comparable to those observed in the urban areas of China (Vlemmix et al., 2015; Wang et al., 2017a). In contrast to these long-term measurements of formaldehyde in China, the minimum VCDs are not observed in the winter but

rather observed in March. Globally photochemical production from biogenic and anthropogenic hydrocarbons dominates the formaldehyde sources while having a minor fraction being directly emitted from biomass burning and vegetation (Fortems-Cheiney et al., 2012). At complex suburban environments, e.g. Mohali, different sources can dominate the formaldehyde production in different periods of the year. At an urban site Kolkata in the IGP, the contribution of primary sources to ambient formaldehyde was observed to be 71% and 32% during summer and winter, respectively (Dutta et al., 2010).

At Mohali two distinct formaldehyde enhancement periods are observed; first in May–June and second in October, both of which are the periods when crop residue burning is practised around the region. Several identified and unidentified chemical compounds are formed in the atmosphere due to crop residue fires, which readily react with OH radicals and form second- and higher-generation oxidation products and potentially form formaldehyde as a by-product (Kumar et al., 2018; Sarkar et al., 2013). The pre-monsoon period of May and June provides favourable conditions (e.g. long daytime hours, uninterrupted solar radiation, and high temperature) for the photochemical production of secondary pollutants from the precursors emitted from wheat residue fires (Kumar et al., 2016; Sinha et al., 2014). This is reflected in very high formaldehyde VCDs observed in May and June in the range of  $16.9 \times 10^{15}$ – $17.4 \times 10^{15}$  molecules cm<sup>-2</sup>. Similar levels of HCHO VCDs are also observed in October, when paddy residue fires are active in the region. Also, the photochemical production of ozone is attributed to the emission from crop residue fires by Kumar et al. (2016). The observed maximum NO<sub>2</sub> VCDs in the winter months indicates very high primary emissions, which could eventually lead to formaldehyde production from its co-emitted precursors. However, low ambient temperatures and lack of ample sunlight hours result in HCHO VCDs that are not so high compared to May, June, and October.

The agricultural lands in the north-west fetch region of Mohali practice agroforestry, where poplar (most common) and eucalyptus trees are planted in the periphery of fields (Sinha et al., 2014; Pathak et al., 2014; Mishra et al., 2020). Over the Indo-Gangetic Plain, biogenic sources contribute to  $\sim 40\%$  of the total VOC emission flux annually (Chaliyakunnel et al., 2019). In the early post-monsoon season, soil moisture availability and daytime temperatures between 30 and 35 °C provide a favourable condition for isoprene emissions (Guenther et al., 1991). Generally, a strong variability is observed in the number of rainfall events and the total rainfall over the IGP between different years (Fukushima et al., 2019), which also affects the soil moisture availability and in turn the biogenic emissions from plants. For the period discussed in this study with available MAX-DOAS HCHO measurements, the years 2014 and 2015 were quite different with respect to the monsoon rainfall. During the monsoon months, 2014 witnessed 18 rainy days (to-

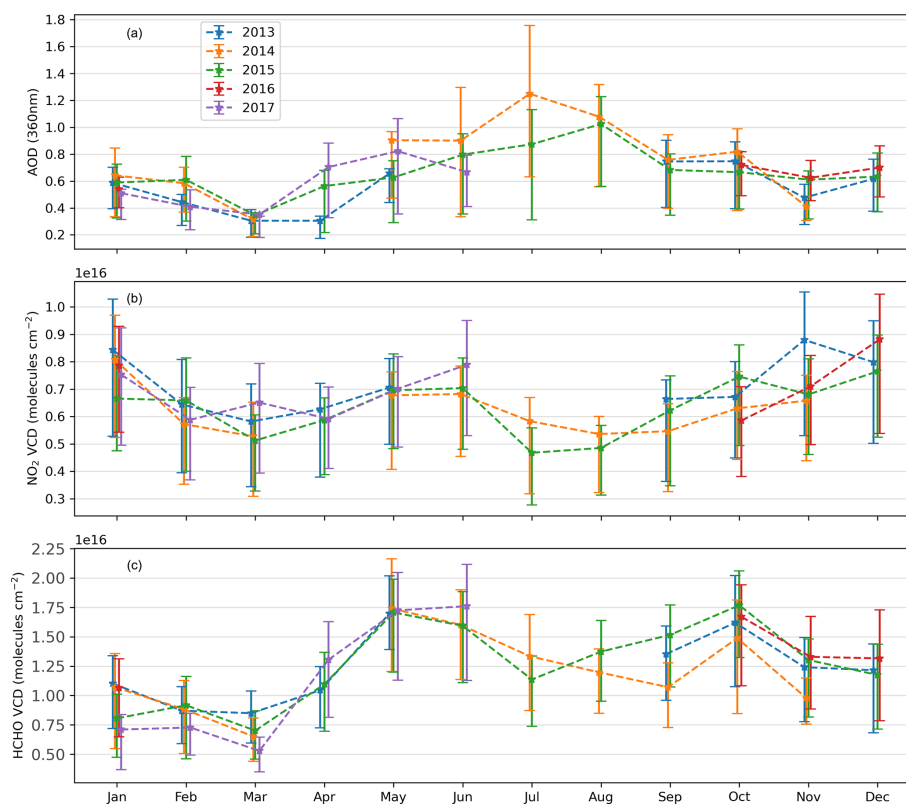


**Figure 4.** Monthly and annual variation in (a) AOD, (b) NO<sub>2</sub>, and (c) HCHO vertical column densities derived from MAX-DOAS measurements. The lower and upper vertical error bars represent the 25th and 75th percentiles, respectively.

tal rainfall = 378 mm), while 2015 witnessed 32 rainy days (total rainfall = 435 mm) in Mohali. Following the number of rainfall events, the early post-monsoon months (August–September) of 2015 witnessed higher HCHO VCDs, which can be attributed to the photo-oxidation of stronger biogenic emissions of isoprene (Mishra and Sinha, 2020). Poplar trees in the Indian subcontinent show little emissions in the months from December to March (Singh et al., 2007) due to loss of leaves. Minimal biogenic and anthropogenic emissions of formaldehyde and its precursors in March resulted in the minimum VCDs during the year. From these observations, we conclude that anthropogenic emissions (primarily due to biomass burning) and their oxidation dominate the formaldehyde seasonality in most of the year except early post-monsoon where biogenic emissions have a major contribution to the measured formaldehyde.

### 3.2 Diurnal variation and vertical profiles of AOD, NO<sub>2</sub>, and HCHO

Figure 5 shows the diurnal variation in the mean vertical profiles of aerosol extinction, NO<sub>2</sub> concentration and HCHO concentration for different months of the year retrieved using MAX-DOAS measurements at Mohali. The corresponding diurnal variations in the VMR of NO<sub>2</sub> and HCHO and

aerosol extinction close to the surface are shown as Figs. F7–F9.

The vertical profile of aerosol extinction is expected to be primarily driven by the boundary layer height (BLH) and to some extent, the photochemistry, which eventually drives secondary aerosol formation (Wang et al., 2019). At Mohali, the diurnal evolution of the aerosol extinction profile heights reaches its maximum during afternoon hours. In Fig. 6a, we show the typical diurnal evolution of BLH from the ERA5 re-analysis data for the four major seasons. We observe a growth of the BLH from morning until noon with a maximum at 14:00 LT and a subsequent decline. The maximum BLH up to 3 km is observed in summer. Shallow daytime BLH up to 1.2 km are observed in the monsoon period due to overcast sky conditions, stronger wind, and high surface moisture and in winter due to low surface temperature and low surface heat flux (Sathyanadh et al., 2017). We observe that the aerosol is trapped in the bottom layers (within 400 m) in winter, whereas during the afternoon hours in summer, monsoon, and early post-monsoon months, aerosol extinction up to  $0.2 \text{ km}^{-1}$  is observed even at around 1.5 km altitude. Though the ERA5 BLH is shallow in monsoon, yet we observe similar aerosol profiles during that period as during summer, which indicates that at Mohali, the vertical distribution of aerosol does not follow ERA5 BLH transition from

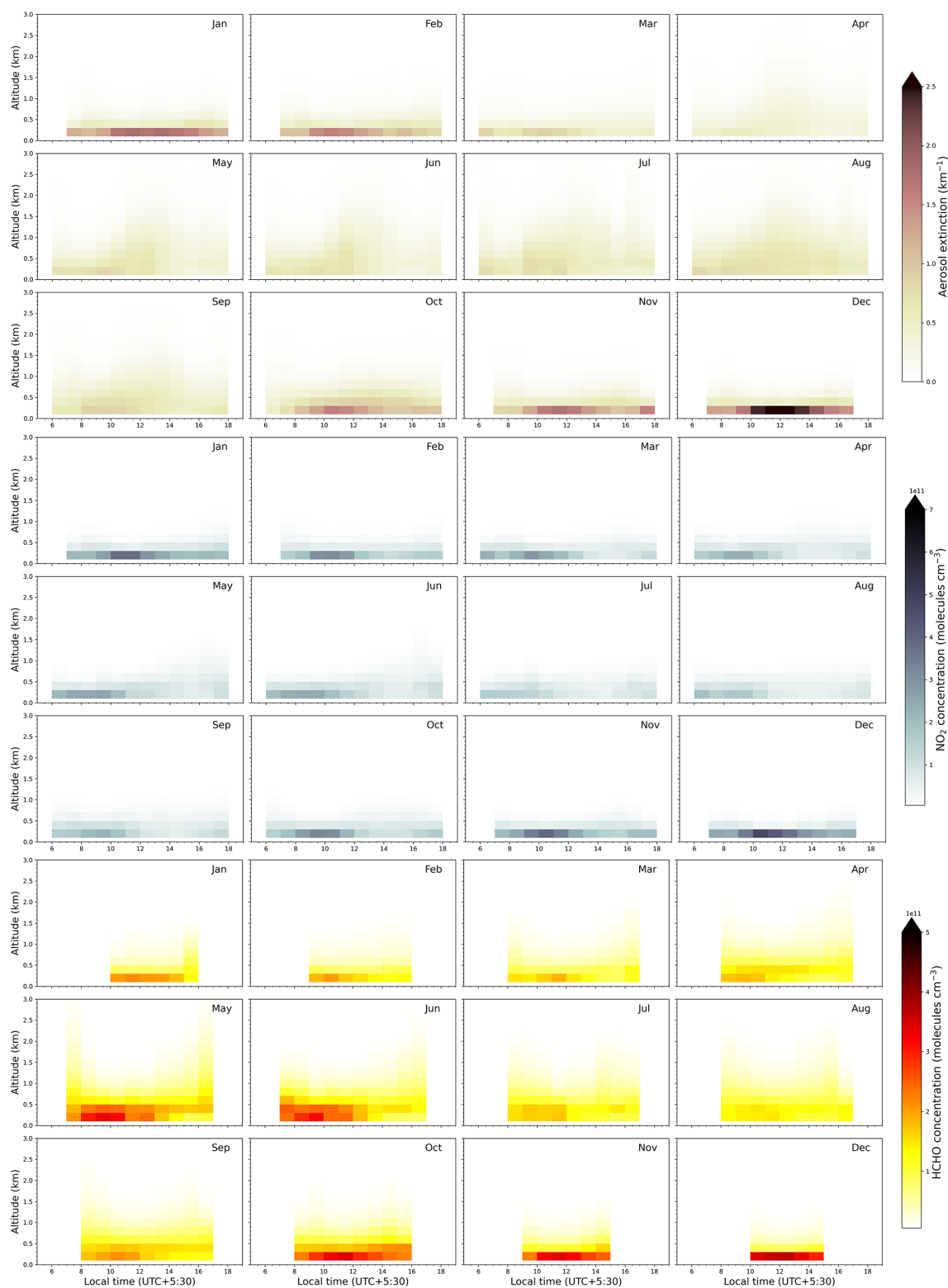


**Figure 5.** Hourly mean vertical profiles of aerosol extinction (top three rows, shades of olive), NO<sub>2</sub> concentrations (middle three panels, shades of blue) and HCHO concentrations (bottom three panels, shades of red) in different months retrieved from 4.5 years of MAX-DOAS measurements over Mohali.

summer to monsoon. Over India, the monsoon months are characterized by strong convective activity, which can bring the surface air aloft to several kilometres despite a shallow ERA5 BLH (Lawrence and Lelieveld, 2010). The convection is rather strong in the Himalayan foothill region (which also includes Mohali) and even pumps the surface pollutants into the UTLS (upper troposphere–lower stratosphere) (Fadnavis et al., 2015). The evidence of pollutant transport associated with deep convection is crucial for PAN (peroxyacetyl nitrate) formation in the UTLS, which is observed by the modelling studies over the IGP and Himalayan region. Long-lived non-methane VOCs (e.g. ethane) can be transported to the UTLS where both convective NO<sub>x</sub> transported from the surface and exchanged from the stratosphere serve as fuel for PAN formation. High aerosol extinction ( $>1.5\text{ km}^{-1}$ ) is observed in the surface layer in the winter months, with the maximum in December. In the winter months, biomass burning contributes to primary aerosol, the formation of secondary aerosol and particle growth as a result of coating on existing aerosol particles. Moreover, the high ambient relative humidity in winter (Kumar et al., 2016) further contributes to the growth of the existing aerosol particles, which further increases the aerosol extinction and in the extreme cases can lead to intense fog.

In order to quantitatively describe the mixing altitude, we define a characteristic profile height  $H_{75}$ , as the height below which 75 % of the trace gas column (or AOD) is located (Vlemmix et al., 2015). The profile parameter  $h$  used in the MAPA inversion algorithm represents the height below which the concentration (or extinction) of the trace gas (or aerosol) remains constant. For elevated profiles (for details, please refer to Wagner et al., 2011),  $h$  refers to the height above the trace gas (or aerosol) layer where the concentration (or extinction) becomes zero. Using  $h$  and shape parameter  $s$ , we calculate a profile height ( $H_{75}$ ) by employing Eqs. (2–5) of Beirle et al. (2019).

We show the diurnal evolution of characteristic profile heights ( $H_{75}$ ) in Fig. F10 for the four major seasons. Figure 6b shows the mean afternoon time characteristic profile heights ( $H_{75}$ ) for aerosol, NO<sub>2</sub>, and HCHO for different months, together with the mean ERA5 BLH. Due to their short atmospheric lifetime ( $<6\text{ h}$ ) during the daytime,  $H_{75}$  for NO<sub>2</sub> and HCHO is lower than that for aerosol.  $H_{75}$  for the measured species is observed to be smaller than the typical boundary layer heights. In the monsoon season, we observe  $H_{75}$  comparable to that in summer, even though the boundary layer height is shallow and comparable to that in winter. Trace gases and aerosol from the surface are lofted up due to deep convection in the monsoon leading to high  $H_{75}$ . This indicates that the vertical mixing of aerosol during the monsoon is not driven by the parameters used to calculate the ERA5 BLH but rather follows the trend of ambient daytime temperature, which does not show such a large difference between summer and monsoon (e.g. Fig. S2 of Kumar et al., 2016). The profile heights for aerosols and HCHO in sum-

mer months are similar to those observed in Beijing (Vlemmix et al., 2015), but we observe a much stronger seasonal dependence.  $H_{75}$  up to 1.1 km for aerosols are observed for the summer (except March) and monsoon months, while in winter  $H_{75}$  is usually less than 500 m. In all months, we observe the minimum  $H_{75}$  among the three measured species for NO<sub>2</sub> ( $\sim 200$  to 450 m), due to its short lifetime and production close to emission sources near the surface.  $H_{75}$  for NO<sub>2</sub> is generally much smaller than for Beijing (urban) and Xingtai (suburban) in China (Wang et al., 2019; Vlemmix et al., 2015).

In all the months and hours of the day, the major fraction of the NO<sub>2</sub> column is located in the bottom-most layer extending from the surface until 200 m. Until 11:00 LT, more than 60 % of the NO<sub>2</sub> column is located in the bottom-most layer in all the months. In winter months (November–February), the same is true for all hours of the day, but in the morning time (until 11:00 LT) the fraction in the bottom layer is even  $>80\%$ . During the late afternoon of the summertime, monsoon, and early post-monsoon, when the BLH grows deeper due to the heating of the surface, we observe a considerable fraction ( $\sim 20\%$ – $30\%$ ) of NO<sub>2</sub> in the layer extending from 200 to 400 m. There is a very small fraction ( $<5\%$ ) of NO<sub>2</sub> column in the layers above 600 m.

We observe the maximum NO<sub>2</sub> columns in the morning hours between 08:00 and 11:00 LT, subsequently decreasing during the day. The major factors driving the NO<sub>2</sub> columns are emissions and lifetime with respect to OH radicals. For the surface concentration, boundary layer dynamics also play an important role. Emissions from traffic and biomass burning for heating and cooking peak in the morning and evening hours. The lifetime of NO<sub>2</sub> is at a minimum in the afternoon when OH radical concentration peaks, which explains the decrease during the day. The amplitude of the diurnal profiles of the NO<sub>2</sub> surface VMR (Fig. F7) is at a maximum during winter months when there is little diurnal variability in the BLH (dilution effect) and NO<sub>2</sub> lifetime (sink effect) between morning and late afternoon hours and the shape is driven primarily by the emissions (source). The amplitude is at a minimum during the monsoon when biomass burning ceases (Mishra and Sinha, 2020). In Sect. 3.7, we will discuss the diurnal variation in the NO<sub>2</sub> surface VMR retrieved from MAX-DOAS and in situ measurements for different months.

For formaldehyde, we observe a comparable distribution among the 0–200 and 200–400 m layers for all seasons except winter. In winter months, the bottom-most layer contains up to 50 % of the total column, which is smaller as compared to aerosols and NO<sub>2</sub>. During the late afternoon hours of summer, monsoon, and the post-monsoon period, we also observe a larger fraction of the HCHO column in the 200–400 m layer as compared to the 0–200 m layer. In the presence of high NO<sub>x</sub> close to the surface, OH concentration is depleted, which might result in slowing down of the formaldehyde production from precursor VOCs. The higher characteristic profile heights of HCHO as compared

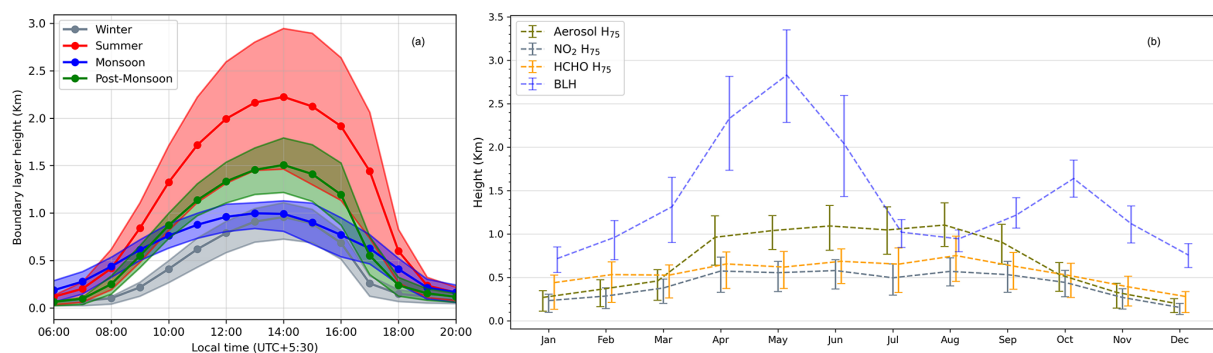


**Figure 6.** (a) Diurnal evolution of the hourly means ERA5 boundary layer height (BLH) at Mohali for the four major seasons of the year. (b) Mean afternoon time (between 12:00 and 15:00 LT) profile height (with 75 % of the total amount below) for aerosols, NO<sub>2</sub>, and HCHO and the ERA5 BLH for different months. The upper and lower vertical error bars represent the monthly variability as 75th and 25th percentiles, respectively.

to those of NO<sub>2</sub> can be attributed to the secondary photochemical formation from primary precursor emissions. A considerable fraction of primary emissions is transported to intermediate layers (similar to NO<sub>2</sub>) during summer, monsoon, and early post-monsoon, where secondary products (e.g. formaldehyde) are formed due to active photochemistry. The months in which primary anthropogenic emissions of formaldehyde and its precursors are stronger (e.g. months except for March, April, July, August, and September), the gradients of vertical profiles of HCHO are stronger in the layers from the surface to 1 km altitude. For the surface VMR, we observe maxima in the morning hours in all seasons except winter and late post-monsoon (Fig. F8). Even though formaldehyde is formed photochemically, which should increase during the day, the VMR close to the surface is reduced due to the vertical mixing in the afternoon hours. We observe the highest daytime HCHO surface VMR in winter months since the major fraction of HCHO is trapped in the bottom-most layer.

### 3.3 Intercomparison and temporal trends of aerosol optical depth

Figure 7a shows the time series of the AOD at 360 nm retrieved from MAX-DOAS measurements of O<sub>4</sub> (scaled by 0.8) and the AOD at 360 nm calculated from MODIS MAIAC data product over Mohali. The corresponding scatter plot is shown in Fig. 7b. Similar plots for the OMAERUV AOD product at 354 nm are shown in Figs. 7c and d. The solid line represents the monthly mean values, while the individual dots in the background represent the daily measurements. The vertical error bars represent the standard error of the mean ( $\sigma/\sqrt{N}$ ), where  $\sigma$  represents the standard deviation and  $N$  represents the number of daily measurements for the month.

The mean MAX-DOAS AOD at 360 nm for the measurement period if averaged around the MODIS overpass time (between 9:30 and 11:30 and between 12:30 and

14:30 LT) was  $0.59 \pm 0.39$  as compared to the MODIS AOD of  $0.81 \pm 0.53$ . The correlation coefficients ( $r$ ) for the linear regressions of daily and monthly mean data between the MAX-DOAS and MODIS AOD are found to be 0.78 and 0.85, respectively. For the monthly mean, we also performed the orthogonal distance regression (ODR) weighted by  $\sigma^{-2}$  (where  $\sigma$  is the monthly standard deviation) between MAX-DOAS and MODIS AOD, for which the slope and offset were 1.13 and 0.12, respectively.

Initially, we performed a comparison of AOD retrieved from MAX-DOAS measurements without applying any scaling factor to the measured O<sub>4</sub> dSCD. While there was a general agreement between the trends in the AOD retrieved from MAX-DOAS and MODIS, the MAX-DOAS AOD showed a strong underestimation (Fig. F11). Several MAX-DOAS measurement studies and comparison with independent datasets (e.g. sun photometer) found that a scaling factor (less than 1) was necessary to bring MAX-DOAS results and independent measurements into agreement (Wagner et al., 2009, 2019; Beirle et al., 2019). However, a similar number of studies did not find the need to apply such a scaling factor (Wang et al., 2017a; Franco et al., 2015). Currently, the reason for the scaling factors is not understood (Wagner et al., 2019, and references therein). In most cases, when scaling factors are used, values between about 0.8 and 0.9 are found best. In our case, the application of a scaling factor was found to be necessary to bring MAX-DOAS and satellite measurements into an agreement. In order to further confirm the choice of the scaling factor, the profile inversion was performed with a variable scaling. Figure F12 shows the distribution of the scaling factor which concludes that an O<sub>4</sub> scaling factor of 0.8 fits best for our measurements.

The NASA OMAERUV data product provides the AOD at 354 nm, but the spatial resolution and temporal coverage are not as good as for the MODIS MAIAC product. From Fig. 7c and d, we observe that OMAERUV generally underestimates the AOD over Mohali, and the level of agree-

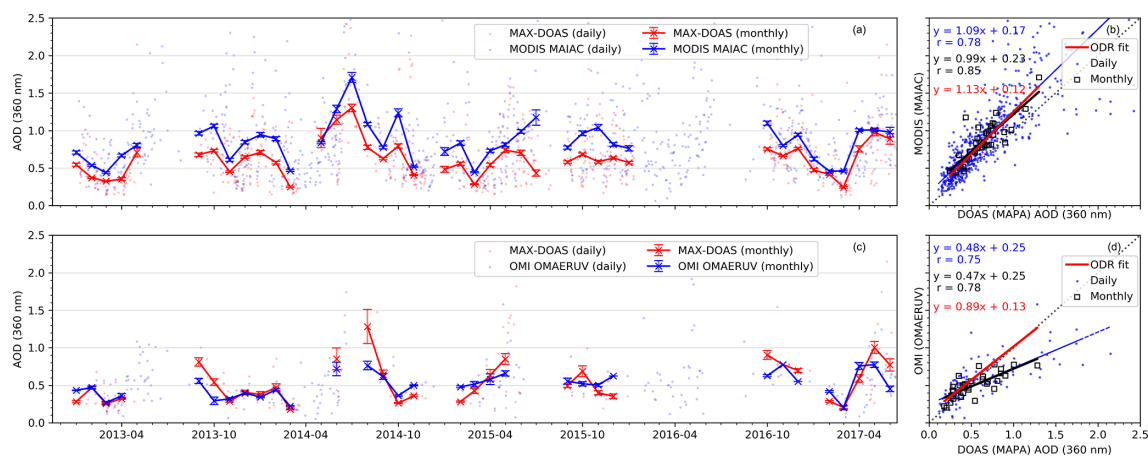


**Figure 7.** Intercomparison of daily (dots) and monthly mean (lines and markers) AOD at 360 nm retrieved from ground-based MAX-DOAS measurements and from the MODIS MAIAC data product (**a**, **b**) and OMI AERUV data product (**c**, **d**). The monthly mean of the MAX-DOAS and satellite data products were calculated by considering only the days of the month when both the measurements were available, causing different MAX-DOAS monthly means in (**a**) and (**c**).

ment is also worse both for daily and monthly mean values. For OMAERUV, the mean AOD was  $0.53 \pm 0.26$ . Over central and east Asia, independent comparison of OMI with AERONET measurements also found a  $\sim 50\%$  underestimation by OMAERUV and a poor agreement for a 10-year period (Zhang et al., 2016). We think that the much coarser spatial resolution of OMAERUV as compared to the MAIAC data product is among the probable reasons for the worse agreement. In order to evaluate this hypothesis, we created a time series of the MODIS MAIAC data product, spatially averaged over 5 and 25 km around Mohali.

MAX-DOAS measurements are spatially representative of a few kilometres in the field of view, depending on the ambient aerosol load and elevation angle, whereas the ground footprints of individual OMI pixels are  $13 \times 24 \text{ km}^2$  in the best case. We have calculated the horizontal sensitivity distance (HSD) of MAX-DOAS for low-elevation angles as the  $e$ -folding distance of O<sub>4</sub> dAMF from the instrument location (Wagner and Beirle, 2016). Figure F13 shows that the mean afternoon time (between 12:00 and 15:00 LT) HSD ranges between 5 and 7 km for clear-sky condition with low aerosol load and between 3 and 6 km for high aerosol conditions. Here it is important to note that this estimate is mainly representative of the near-surface layers. While for the trace gas inversions, the VCD is constrained by all elevation angles, the determination of the AOD is mostly constrained by the high-elevation angles. For high-elevation angles, the sensitivity range is much closer to the instrument (at distances up to 1 and 2 km for layer height of 0.5 and 1 km, respectively) (see Fig. 6a). Comparing the spatially degraded time series with MAX-DOAS AOD resulted in a worse agreement ( $r = 0.75$  and  $0.79$  for the daily and monthly means, respectively) for 25 km but did not change significantly for 5 km (Fig. F14) as compared to the original comparison when only a 2 km

area around Mohali was considered for spatial averaging. In addition to the effect of horizontal gradients, the poor agreement of the OMAERUV product might also be caused by residual cloud contamination. Further, non-representative assumptions about the aerosol types between smoke, dust, and non-absorbing aerosols used for the inversion of the measured reflectances might play a role, as highlighted by Zhang et al., 2016.

### 3.4 Intercomparison and temporal trends of NO<sub>2</sub> vertical columns

Figure 8 shows the time series of the NO<sub>2</sub> vertical column densities measured by MAX-DOAS and by OMI for the three different data products. Please note that for calculating the monthly means, we only considered the days of the month when both cloud-screened and quality-controlled satellite and MAX-DOAS data were available. Within the complete study period, the DOMINO, QA4ECV, and OMNO2 data products had 60%, 47%, and 46% days of cloud- and quality-screened data, respectively. We observe a general agreement in the trends of the NO<sub>2</sub> VCDs between the MAX-DOAS and OMI datasets. However, all OMI data products generally underestimate the NO<sub>2</sub> VCDs. The mean MAX-DOAS NO<sub>2</sub> VCD for the measurement period if averaged between 12:30 and 14:30 LT (around the OMI overpass) was  $(5.4 \pm 3.0) \times 10^{15} \text{ molecules cm}^{-2}$ . The mean VCD for OMI was  $(3.7 \pm 2.4) \times 10^{15} \text{ molecules cm}^{-2}$ ,  $(3.7 \pm 1.3) \times 10^{15} \text{ molecules cm}^{-2}$ , and  $(3.7 \pm 1.7) \times 10^{15} \text{ molecules cm}^{-2}$ , respectively, for the DOMINO, QA4ECV, and OMNO2 data products. The reasons for the systematic difference between the MAX-DOAS and OMI measurements can be attributed to several factors including (1) difference in spatial representation and (2) differences in vertical sensitivity of MAX-DOAS and OMI. Previous validation studies over China also

found systematic underestimation of  $\sim 60\%$  over Nanjing by the OMNO2 and  $\sim 30\%$  over Beijing and Nanjing by the DOMINO product (Chan et al., 2019; Ma et al., 2013). The observed discrepancies were attributed to differences in spatial representativeness, which introduces smoothing of the measured NO<sub>2</sub> VCD over a large satellite ground pixel and to the shielding effect of aerosols. At Mohali, the maximum disagreement of the OMI products is observed during the late post-monsoon and winter months, where all satellite data products significantly underestimate the NO<sub>2</sub> VCDs. Note that a large amount of aerosol and trace gases are emitted from the crop residue and domestic fires in these months, a major fraction of which is trapped close to the surface due to suppressed ventilation.

Figure 8 also shows the linear regression fits of the three OMI data products versus the MAX-DOAS NO<sub>2</sub> VCDs. We observe smaller scatter in the QA4ECV and OMNO2 products for both daily and monthly values, as compared to DOMINO product. An ODR fit was performed between the monthly means of MAX-DOAS and OMI NO<sub>2</sub> VCDs weighted by  $\sigma^{-2}$ , where  $\sigma$  is the monthly standard deviation. The slopes of the ODR fit between the MAX-DOAS and OMI monthly mean NO<sub>2</sub> VCDs were 0.94, 0.59, and 0.78, respectively, for DOMINO, QA4ECV, and OMNO2. The offsets of the ODR fits were  $-8.1 \times 10^{14}$ ,  $8.4 \times 10^{14}$ , and  $-1.7 \times 10^{14}$ , respectively, for DOMINO, QA4ECV, and OMNO2, respectively. Over Mohali, we observe excellent consistency between the QA4ECV and OMNO2 products with a slope and correlation coefficient ( $r$ ) of 0.94 and 0.72, respectively, between both datasets.

Since we have retained the OMI pixels whose centre points lie within  $0.25^\circ \times 0.25^\circ$  of the MAX-DOAS measurement site, differences can arise due to the smoothing effect across the OMI ground pixels. With the pristine regions of the Himalayan mountain range only  $\sim 35$  km from Mohali, smaller NO<sub>2</sub> VCD from OMI measurements are expected due to systematic gradients towards the mountain range. The effect of smoothing over a large area can be minimized if only collocated pixels are retained for the intercomparison. However, this significantly reduced the number of available days for intercomparison. If only collocated pixels were considered, we were left with only 35 %, 25 %, and 22 % of the measurement days for DOMINO, QA4ECV, and OMNO2, respectively. Due to the poor statistics, we did not observe improvements in the correlation coefficient ( $r$ ) of the linear regression of the daily data and these changed from 0.38, 0.50 and 0.43 to 0.38, 0.56, 0.43, respectively, for DOMINO, QA4ECV, and OMNO2. In the absence of higher-resolution NO<sub>2</sub> data for the study period, we could not quantify the effect of the different spatial representativeness of the MAX-DOAS and OMI measurements.

One of the major reasons for the disagreement between satellite and MAX-DOAS measurement is the difference in vertical sensitivity of the two measurements. Satellite instruments have limited sensitivity close to the ground. In con-

trast, MAX-DOAS measurements have the highest sensitivity close to the ground, while it becomes virtually zero above 3–4 km. The limited sensitivity of the satellite instruments is addressed using the box air mass factors (bAMFs) and the a priori profiles of the trace gases to be retrieved (Eskes and Boersma, 2003). In Appendix D we compare the bAMFs used in the DOMINO and QA4ECV retrievals with those calculated by employing the radiative transfer model (RTM) McARTIM over Mohali using the mean aerosol extinction profiles retrieved from the MAX-DOAS measurements. A discrepancy is found between the calculated bAMFs and those used for OMI retrievals (DOMINO and QA4ECV) (Fig. D1), such that the calculated bAMFs show systematically higher values close to the surface. In such a case, attribution of a smaller fraction of NO<sub>2</sub> in layers close to the surface in the a priori profiles cause a systematic underestimation of the VCDs (please see Appendix D for details). We found that the a priori NO<sub>2</sub> profiles used in the DOMINO v2 retrievals strongly differ from those retrieved using the MAX-DOAS measurements for winter and polluted post-monsoon when a large fraction of NO<sub>2</sub> is present in layers close to the surface (Figs. 5 and D2).

In order to eliminate the difference caused by the non-representative a priori NO<sub>2</sub> profiles, we calculated the “modified MAX DOAS VCDs” (called VCD<sub>mod</sub> hereafter), which represent the MAX-DOAS NO<sub>2</sub> VCDs as observed by OMI. The application of the OMI tropospheric averaging kernels and a priori profiles also to the MAX-DOAS profiles makes the comparison independent of the a priori profiles used for the OMI retrieval. In order to do so, we apply the tropospheric averaging kernels of OMI DOMINO (AK<sub>trop</sub>) data product to the NO<sub>2</sub> vertical profiles ( $x_{\text{doas}}$ ) retrieved from MAX-DOAS in layers ( $i$ ) from ground ( $i = 0$ ) to  $h = 4$  km ( $i = 20$ ), according to the following equation (Rodgers and Connor, 2003):

$$\text{VCD}_{\text{mod}} = \sum_{i=0}^h \text{AK}_{\text{trop},i}(x_{\text{doas},i} - x_{\text{ap},i}) + x_{\text{ap},i}. \quad (4)$$

Here,  $x_{\text{ap},i}$  represents the DOMINO a priori NO<sub>2</sub> profiles. Please note that the total averaging kernels (AK<sub>tot</sub>) provided in the DOMINO level 2 data product are converted to tropospheric averaging kernels using the ratio of total AMF (AMF<sub>tot</sub>) and tropospheric AMF (AMF<sub>trop</sub>):

$$\text{AK}_{\text{trop},i} = \text{AK}_{\text{tot}} \times \frac{\text{AMF}_{\text{tot}}}{\text{AMF}_{\text{trop}}}. \quad (5)$$

Figure 9 shows the time series of original MAX-DOAS VCDs (red), OMI DOMINO VCDs (blue), and modified MAX-DOAS VCDs (black). We observe that the bias between the OMI and MAX-DOAS measurements is smaller if the averaging kernels and a priori profiles are applied to the MAX-DOAS NO<sub>2</sub> profiles. However, in contrast to the MAX DOAS VCDs, the VCD<sub>MOD</sub> are systematically lower than the DOMINO NO<sub>2</sub> VCDs.

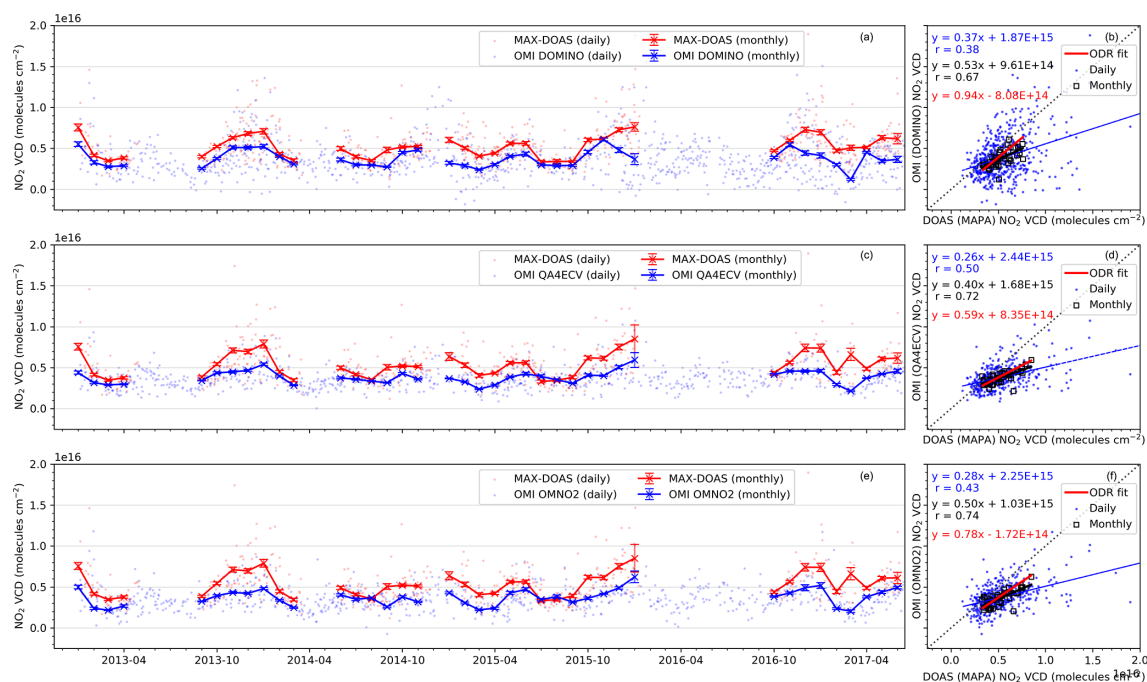


**Figure 8.** Intercomparison of time series of daily (dots) and monthly mean (lines and markers) NO<sub>2</sub> VCDs retrieved from ground-based MAX-DOAS measurements and the OMI DOMINO data product (a), the OMI QA4ECV data product (b), and the OMI OMNO2 data product (c). The vertical error bars represent the monthly variability as the standard error of the mean. The monthly mean of the MAX-DOAS and satellite data products were calculated by considering only the days of the month when both the measurements were available, causing different MAX-DOAS means in (a), (c), and (e). Scatter plots (panels b, d, and f for DOMINO, QA4ECV, and OMNO2, respectively) using the daily and monthly mean values are shown adjacent to the time series.

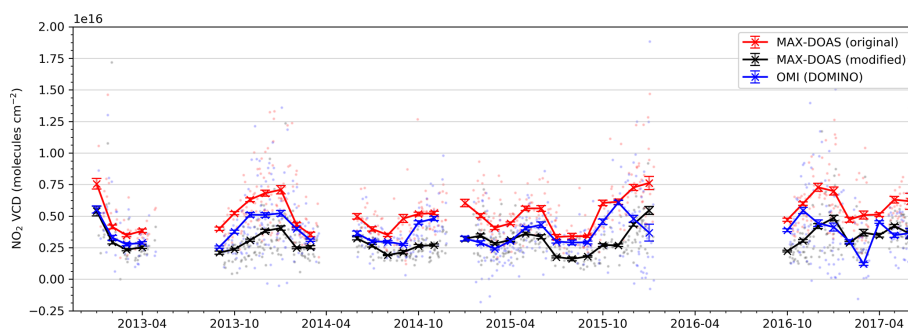


**Figure 9.** Time series of daily (dots) and monthly means (lines and markers) of MAX-DOAS NO<sub>2</sub> VCDs, OMI DOMINO NO<sub>2</sub> VCDs, and modified MAX-DOAS VCDs modified by using the DOMINO averaging kernels and a priori profiles.

While the application of the DOMINO averaging kernels and a priori NO<sub>2</sub> profiles to the MAX-DOAS profiles according to Eq. (4) accounts for the reduced OMI sensitivity close to the surface, it does not account for the limited sensitivity of MAX-DOAS at higher altitudes (above 3–4 km). VCD<sub>MOD</sub> hence represents the MAX-DOAS NO<sub>2</sub> VCD from the ground to up to ~4 km altitude, whereas the DOMINO NO<sub>2</sub> VCDs represents the NO<sub>2</sub> VCDs from the ground until the tropopause. For a qualitative estimate of the NO<sub>2</sub> column at high altitudes, we have calculated the fraction of the NO<sub>2</sub> column between 4 km altitude and the tropopause by

only considering the NO<sub>2</sub> partial VCDs of the TM4 a priori profiles in various layers. The NO<sub>2</sub> partial columns in the 4 km to tropopause altitude range account for 7%–18% (interquartile range) of the total NO<sub>2</sub> a priori VCDs. Hence, due to the limited sensitivity of MAX-DOAS at higher altitudes, the VCD<sub>MOD</sub> is systematically smaller than DOMINO NO<sub>2</sub> VCDs.

Please note that a similar comparison with OMI QA4ECV and OMNO2 products is not possible as a priori profiles and averaging kernels, respectively, are not available for these data products. For qualitative evaluation, we have used the

TM4 NO<sub>2</sub> a priori profiles with QA4ECV averaging kernels and calculated VCD<sub>MOD</sub>. This also results in an improvement of the bias between the MAX-DOAS and QA4ECV NO<sub>2</sub> VCDs (Fig. F15). A different approach for improved agreement between MAX-DOAS and satellite VCDs is by using the MAX-DOAS NO<sub>2</sub> profiles as a priori profiles for the calculation of air mass factors for the satellite retrieval (Chan et al., 2019; De Smedt et al., 2015). We discuss this approach and its limitations in Appendix D.

### 3.5 Intercomparison and temporal trends of HCHO vertical columns

Figure 10 shows the time series of HCHO VCDs measured by MAX-DOAS and by OMI for the QA4ECV (panel a) and OMHCHO products (panel c) with the respective scatter plots (panels b and d). Within the chosen quality and cloud filters, the QA4ECV and OMHCHO datasets have 42 % and 67 % days, respectively, out of the complete study period. The mean MAX-DOAS HCHO VCD for the measurement period if averaged between 12:30 and 14:30 LT (around OMI overpass) was  $(11.3 \pm 6.9) \times 10^{15}$  molecules cm<sup>-2</sup>. The mean VCDs from OMI observations were  $(14.9 \pm 11.3) \times 10^{15}$  molecules cm<sup>-2</sup> and  $(11.3 \pm 11.7) \times 10^{15}$  molecules cm<sup>-2</sup> for the QA4ECV and OMHCHO data products, respectively. A small negative bias was expected in the MAX-DOAS HCHO VCDs, as its sensitivity is limited at higher altitudes where a background HCHO may be present due to the oxidation of long-lived hydrocarbon (mainly methane). Though the non-methane VOCs dominate the formaldehyde production over land, methane oxidation is a ubiquitous source of formaldehyde across the globe. At high altitudes (between 3.6 and 8 km) in a pristine location (Jungfraujoch), the background HCHO VCDs have been observed between  $0.75 \times 10^{15}$  and  $1.43 \times 10^{15}$  molecules cm<sup>-2</sup> (Franco et al., 2015) which is equivalent to  $\sim 10\%$  of the total column as measured over Mohali.

In general, we see slightly higher VCDs by the OMI QA4ECV product compared to MAX-DOAS, except for the post-monsoon months, when we observe a better agreement between the two datasets. For the OMHCHO product, the monthly mean HCHO VCDs agree well with MAX-DOAS except for the post-monsoon of 2015, where MAX-DOAS VCDs were higher. The generally good agreement of the OMHCHO VCDs with MAX-DOAS is in line with previous works (Chan et al., 2019; Wolfe et al., 2019). The OMHCHO product was also shown to have a good agreement with airborne measurements in the remote troposphere (Wolfe et al., 2019). However, the accountability in the range of the monthly mean HCHO VCDs was much better for the QA4ECV product (slope = 0.77) as compared to OMHCHO (slope = 0.41). In comparison to the QA4ECV NO<sub>2</sub> dataset, we observe a higher noise in both spatial and temporal patterns of the HCHO VCDs, which arises due to the relatively small atmospheric absorption. The larger uncertainty

in the QA4ECV HCHO dataset is also evident from the scatter of daily measurements where sometimes VCDs close to zero are observed. For some months (e.g. January 2015, January 2016, March 2017, April 2017, and June 2017) when less than 6 d of QA4ECV data is retained for calculating the monthly means for intercomparison with MAX-DOAS measurements, the values should be considered carefully. If only collocated pixels are considered for the QA4ECV HCHO product, the statistics get poorer (only 17 % of valid observations) and we observe a worse coefficient of correlation ( $r = 0.19$  and  $0.17$  for daily and monthly means) with MAX-DOAS measurements.

The finding that in contrast to NO<sub>2</sub>, no general underestimation is observed for the comparison of the satellite HCHO VCDs to the MAX-DOAS HCHO VCDs can be attributed to the different vertical profiles and the different vertical sensitivities of MAX-DOAS and OMI observations. Since in general, the HCHO profiles reach higher altitudes than NO<sub>2</sub>, the satellite observations capture a larger fraction of the total HCHO column. However, we cannot perform a comparison of the modified MAX-DOAS VCDs for HCHO similar to that calculated for DOMINO NO<sub>2</sub>, as the total AMFs and averaging kernels (needed for Eq. 5) are not available for the QA4ECV and OMHCHO data products, respectively.

### 3.6 Discerning the sensitivity of ozone production on NO<sub>x</sub> and VOCs

Martin et al. (2004) recommended the use of the ratio of the formaldehyde and NO<sub>2</sub> columns from satellite observations as an indicator for the ozone production regime. HCHO/NO<sub>2</sub> ratios of less than 1 represent a VOC sensitive regime, whereas values greater than 2 indicate a NO<sub>x</sub> sensitive regime. Intermediate values of the HCHO/NO<sub>2</sub> ratio indicate a strong sensitivity towards both NO<sub>x</sub> and VOCs. The threshold for this indicator was initially calculated for afternoon time (between 13:00 and 17:00 LT) but was later extended to also include morning period by Schroeder et al. (2017). However, Schroeder et al. (2017) also indicated that the upper limit of the intermediate regime might vary spatio-temporally. Nonetheless, higher HCHO/NO<sub>2</sub> indicates that a reduction in NO<sub>x</sub> emissions would be more effective for ozone reduction. While the in situ measurements of the total OH reactivity are a more robust method to evaluate the ozone production regime, due to the experimental constraints, these measurements are reported only rarely and for short time periods (e.g. a few weeks or months) (Kumar et al., 2018; Kumar and Sinha, 2014). Mahajan et al. (2015) evaluated the ozone production regime over India using the ratio of HCHO and NO<sub>2</sub> VCDs observed from SCIAMACHY for the mean of the years 2002–2012. Over the north-west IGP, the HCHO/NO<sub>2</sub> was observed to be less than 1 in the winter months and between 1 and 2 in all other months. From our intercomparisons in the previous sections, we note that while the OMI NO<sub>2</sub> VCDs are generally un-

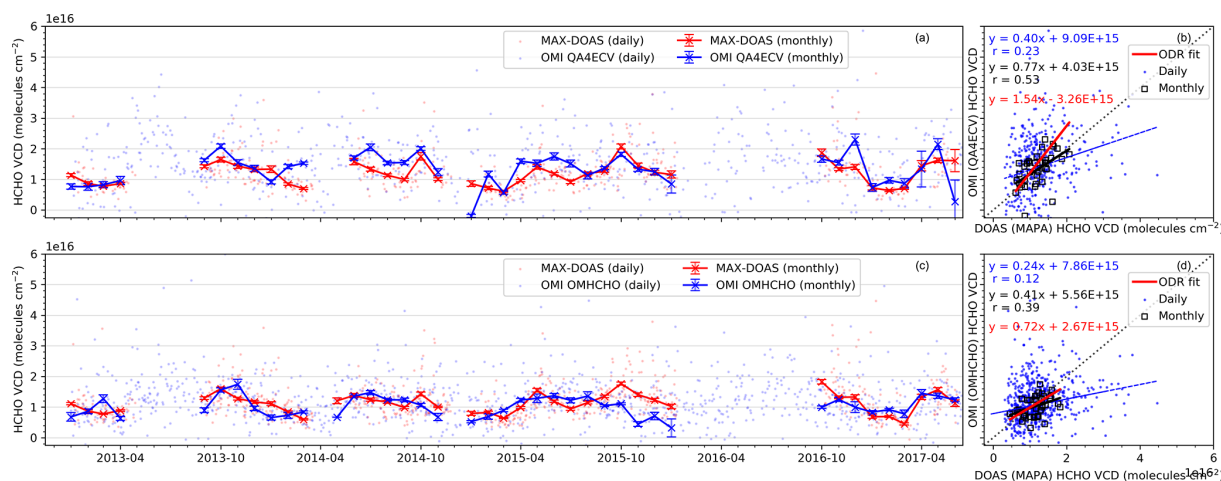


**Figure 10.** Intercomparison of time series of daily (dots) and monthly mean (lines and markers) HCHO VCDs retrieved from ground-based MAX-DOAS measurements and the OMI QA4ECV data product (a) and the OMI OMHCHO data product (c). The respective vertical error bars represent the  $1\sigma$  monthly variability as the standard error of the mean. The monthly means of the MAX-DOAS and satellite data products were calculated by considering only the days of the month when both the measurements were available, causing different MAX-DOAS means in (a) and (c). Scatter plots (b, d) using the daily and monthly mean values are shown adjacent to the time series.

derestimated, the HCHO VCDs are generally well accounted for. Hence the true HCHO/NO<sub>2</sub> will be smaller than those indicated by satellite observations, which indicates that the estimated sensitivity of the ozone production regime towards NO<sub>x</sub> should be smaller and shifted towards VOCs. Using the WRF-CMAQ model simulations at  $36 \times 36 \text{ km}^2$  resolution over India for 2010, Sharma et al. (2016) have evaluated the ozone production to be strongly sensitive to NO<sub>x</sub> emissions throughout the year and recommended reduction in transport emissions which account for 42 % of the total NO<sub>x</sub> emissions. However, with an increase in transport and power plant emissions (strong NO<sub>x</sub> sources) over India, the regimes are susceptible to shift away from being NO<sub>x</sub> limited and need to be re-evaluated. Figure 11 shows the monthly mean HCHO/NO<sub>2</sub> ratio calculated using the MAX-DOAS measurements for the morning (09:30–11:30 LT), noontime around the OMI overpass (12:30–14:30 LT), and late afternoon (15:30–17:30 LT). We observe a stronger (smaller) sensitivity towards NO<sub>x</sub> during the late afternoon (morning) as compared to noontime similar to other urban locations in the USA (Schroeder et al., 2017). VOCs contribute to ozone production via their oxidation by OH radicals and subsequent formation of peroxy radicals. During the build-up hours of ozone (between sunrise until noontime) at Mohali, the radicals' abundance is expected to be limited. Hence, the ozone production is more sensitive to VOC (or “radicals”) during morning, which shifts towards NO<sub>x</sub> later during the day. In winter months, mean daytime HCHO/NO<sub>2</sub> ratios between 1 and 2 are observed, which represent sensitivity towards both NO<sub>x</sub> and VOCs. The sensitivity of the ozone production regime changes towards NO<sub>x</sub> with the onset of summer and stays like that until the end of the post-monsoon

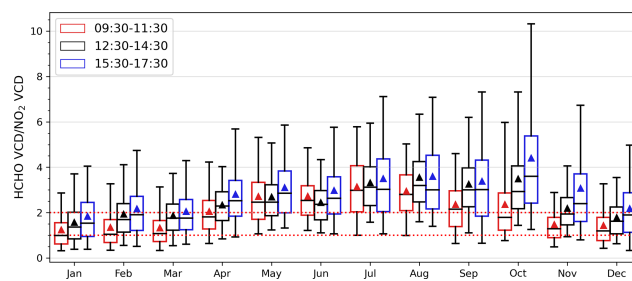


**Figure 11.** Monthly mean HCHO VCD/NO<sub>2</sub> VCD ratios (triangles) calculated from MAX-DOAS measurements for the morning (09:30–11:30 LT, red), noon around the OMI overpass time (12:30–14:30 LT, black), and late afternoon (15:30–17:30 LT, blue) over Mohali. The lines at the centres of the boxes represent the median; the boxes show the interquartile ranges whereas the whiskers show the 5th and 95th percentile values.

season. Over the Indo-Gangetic Plain, the strongest ozone pollution episodes are observed in the summer and post-monsoon months during the afternoon hours between 12:00 and 16:00 LT (Kumar et al., 2016; Sinha et al., 2015). Surface ozone measurements from Mohali have shown enhancement in its ambient concentrations during the late post-monsoon as compared to the early post-monsoon even though the daytime temperature drops by 6 °C. During summer, enhanced precursor emission from fires lead to an increase in  $\sim 19$  ppb ozone under similar meteorological conditions. Considering the stronger sensitivity of daytime ozone production towards NO<sub>x</sub>, the ozone mitigation strategies should focus on NO<sub>x</sub> emission reductions.

### 3.7 Surface volume mixing ratios of NO<sub>2</sub> and HCHO

The surface VMRs of NO<sub>2</sub> and HCHO can be derived from the MAX-DOAS measurements using the retrieved profiles. For MAPA, the profiles are saved using output grids of a uniform thickness of 200 m. The mean concentrations in the bottom-most layer have been used to calculate VMR by considering the measured ambient temperature.

Figure 12 shows the time series of the NO<sub>2</sub> VMRs measured with the *in situ* chemiluminescence analyser and that in the lowest 200 m grid obtained from the profile inversion from the MAX-DOAS measurements. The measurement frequency of the *in situ* measurements was 1 min, whereas, from MAX-DOAS, the mean concentrations are retrieved from individual complete sequences (~ 10 min). Hence, we averaged the *in situ* measurements to coincide with the exact MAX-DOAS measurement time. We observe a reasonable agreement between the two measurements in terms of temporal variability, but the MAX-DOAS surface VMRs are systematically higher until the end of 2014. The differences between the two can probably be explained by the difference in the horizontal and vertical representativeness and resolution and have been discussed in detail in Appendix E. Briefly, the surface VMR from MAX-DOAS represents the mean in the bottom-most 200 m grid of MAPA output, while those from *in situ* measurements are more sensitive to air mass sampled closed to the inlet. Hence MAX-DOAS VMRs are representative of a larger area around the measurement site, and we infer from Fig. 1 that the measurement location is relatively cleaner compared to the surroundings in terms of NO<sub>2</sub> levels. The mean NO<sub>2</sub> surface VMR from MAX-DOAS measurements was  $8.2 \pm 6.7$  ppb, whereas that from the concurrent *in situ* measurements was  $6.0 \pm 5.0$  ppb. If we consider all *in situ* observations (which also include the night-time observation and periods when MAX-DOAS measurements were unavailable), the mean NO<sub>2</sub> VMR was  $8.6 \pm 6.9$  ppb. As compared to previous MAX-DOAS measurements from India (Biswas et al., 2019), at a rural site ( $0.8 \pm 0.2$  ppb), we observe much higher NO<sub>2</sub> VMR in Mohali. However, these are comparable to previous *in situ* NO<sub>2</sub> VMR measured for a period of more than 1 year at urban and suburban locations (distant from traffic) of India (e.g. Mohali: 8.9 ppb; Pune: ~ 9.5/8.7 ppb; Kanpur: 5.7 ppb) (Gaur et al., 2014; Kumar et al., 2016; Beig et al., 2007; Debaje and Kakade, 2009) but smaller than near traffic urban measurement (e.g. New Delhi: 12.5/18.6 ppb; Agra: 15–35 ppb) (Saraswati et al., 2018; Tiwari et al., 2015; Singla et al., 2011). Please note that we have used an NO<sub>2</sub>/NO<sub>x</sub> ratio of 0.9 to estimate NO<sub>2</sub> VMR for comparison with the previous measurements which reported NO<sub>x</sub> VMR and hence have a larger uncertainty (Kunhikrishnan et al., 2006). The inset of Fig 12a shows the monthly variability of surface NO<sub>2</sub> VMR as a box-and-whiskers plot. Similar to the VCDs, we observe maximum NO<sub>2</sub> VMR in winter followed by the crop residue burning active periods of post-monsoon and summer.

Figure 13 shows the time series of the HCHO VMR measured with the PTR-MS and those derived for the lowest 200 m layer obtained from profile inversion of the MAX-DOAS measurements. The mean HCHO surface VMR from MAX-DOAS measurements was  $8.7 \pm 7.5$  ppb, whereas that from concurrent *in situ* PTR-MS measurements was  $3.3 \pm 1.7$  ppb. For HCHO, higher VMR from MAX-DOAS measurements can be explained by its photochemical formation at altitudes higher than the inlet of PTR-MS. This has been further discussed in Appendix E. The measured HCHO VMRs are comparable to previous MAX-DOAS measurements from India (Pantnagar: 2–6 ppb) but much lower than those measured previously in India using offline techniques (e.g. north Kolkata: 16 ppb; south Kolkata: 11.5 ppb) (Dutta et al., 2010; Hoque et al., 2018). From the monthly variation in HCHO VMRs shown in the inset of Fig. 13a, we observe that the maximum is observed in late post-monsoon and winter followed by late summer (crop residue burning active period). This monthly variability is slightly different from that of the HCHO VCDs (discussed in Sect. 3.1). A shallower profile (Fig. 5) in the late post-monsoon and winter leads to high surface VMR even though the VCD is smaller than that in late summer.

Figure F7 shows the mean diurnal profiles of the surface NO<sub>2</sub> VMRs for different months using MAX-DOAS and *in situ* measurements. A typical diurnal feature representative of a suburban location was observed from the *in situ* measurements, which is explained in detail elsewhere for Mohali for different seasons (Kumar et al., 2016). For the daytime hours, when MAX-DOAS observations are also available, we observe a general agreement in the absolute values and temporal evolution between the two measurements in all the seasons except winter. The occurrence of a morning peak for the *in situ* measurements between 07:00 and 09:00 LT in all months is primarily driven by emissions (traffic and bio-fuel combustion). For the MAX-DOAS observations, a similar maximum occurs between 08:00 and 10:00 LT and between 09:00 and 11:00 LT in winter months. The time shift compared to the maximum in the *in situ* measurements can be explained by the accumulation of the surface emission in the boundary layer and breaking of the nocturnal boundary layer. The latter causes the NO<sub>x</sub> present at high altitudes (e.g. from power plants >200 m, Fig. 5) to mix in with the surface layers. A modelling study performed using the CMAQ model has shown that the peak in the diurnal profiles of NO<sub>2</sub> columns occurs 2–3 h later than that for surface concentrations (Fishman et al., 2008). Since MAX-DOAS surface VMR represents the mean over a few hundred metres, we expect similar behaviour in its comparison with *in situ* measurements. In winter months, though the diurnal trends are similar in both observations, a general overestimation by MAX-DOAS is found, which is caused by a shallower boundary layer and the presence of high NO<sub>2</sub> mixing ratios above the inlet of the *in situ* analyser.

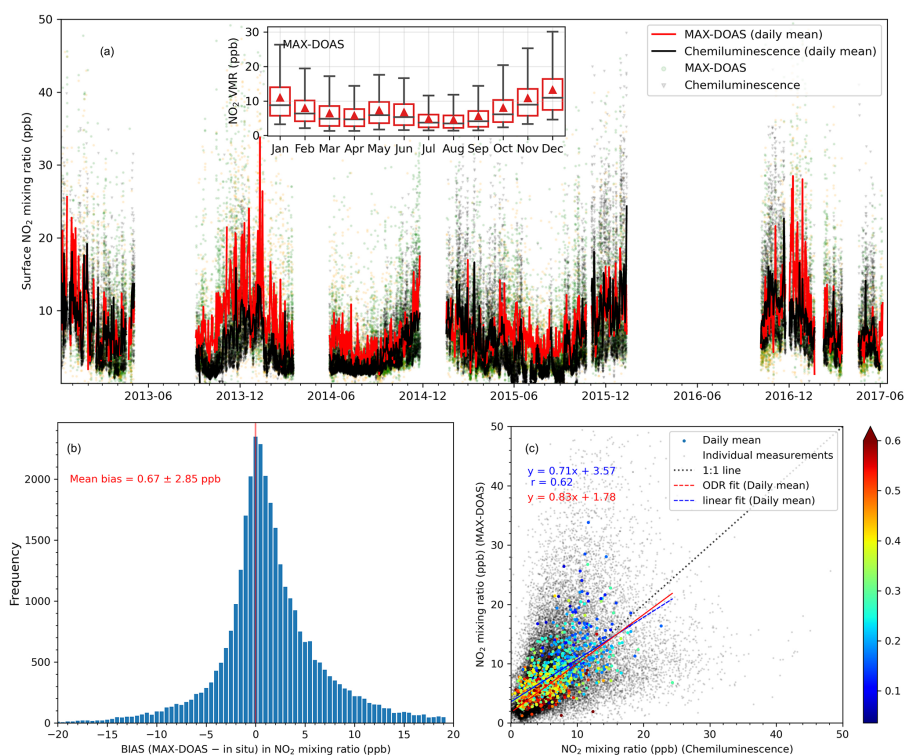


**Figure 12.** (a) Daily mean NO<sub>2</sub> mixing ratios measured using an in situ chemiluminescence analyser (black line) and average mixing ratio in the lowest layer (0–200 m) retrieved by the profile inversion of MAX-DOAS measurements (red line). The green and orange dots in the background show the mixing ratios corresponding to the individual MAX-DOAS elevation sequences flagged as valid and warning, respectively. The inset of (a) shows the monthly variability of the MAX-DOAS surface NO<sub>2</sub> VMR as a box-and-whiskers plot; (b) shows the frequency distribution of the BIAS (MAX-DOAS – in situ) for the individual surface VMR measurements; (c) shows the scatter plot between the daily mean surface NO<sub>2</sub> VMR from MAX-DOAS and an in situ analyser colour-coded according to the profile height ( $H_{75}$ ). The individual measurements are shown as black dots in the background of (c).

#### 4 Conclusions

We have presented long-term (from January 2013 until June 2017) MAX-DOAS measurements of NO<sub>2</sub>, HCHO, and aerosols from a regionally representative suburban site, Mohali, in the densely populated north-west Indo-Gangetic Plain. MAX-DOAS radiance measurements at 360 nm and a colour index (ratio of measured radiances at 330 and 390 nm) were employed to quantitatively determine the prevalent sky conditions. Clear sky with high aerosol load conditions (AOD at 360 nm > 0.85) was observed for about half of the measurement period. The profile inversion algorithm MAPA was used to derive the aerosol optical depth, vertical column density of NO<sub>2</sub> and HCHO, and vertical profiles of aerosol extinction, NO<sub>2</sub>, and HCHO. A mean AOD at 360 nm, tropospheric NO<sub>2</sub> VCD, and HCHO VCD for the measurement period were observed to be  $0.63 \pm 0.51$ ,  $(6.7 \pm 4.1) \times 10^{15}$ , and  $(12.1 \pm 7.5) \times 10^{15}$  molecules cm<sup>-2</sup>, respectively, with substantial seasonal variations in all the measured parameters. While the NO<sub>2</sub> VCDs are generally lower than those observed in the suburban and urban location of China and western countries, the HCHO VCDs are comparable to previ-

ously reported values. Despite the rapid urbanization, no evident annual trends were observed in AOD, NO<sub>2</sub>, and HCHO VCDs for the measurement period. The seasonal trends are rather driven by non-organized anthropogenic sources of emissions, e.g. agricultural residue burning, waste burning, and biofuel burning for heating and cooking. Early summer (March) and monsoon (July and August) months are the cleanest with respect to the measured NO<sub>2</sub> and HCHO VCDs, but high AOD was observed during the monsoon likely due to hygroscopic growth of the aerosol particles. Maximum NO<sub>2</sub> VCDs were observed in winter months, followed by the periods of post-monsoon and summer when extensive crop residue burning is practised in the agricultural regions near the measurement site. Maximum formaldehyde VCDs were observed in the summer and post-monsoon seasons when photochemical production from precursors emitted from agricultural residue fires is favoured by meteorological conditions (high temperature and strong solar radiation). Biogenic sources were also found to be crucial for formaldehyde during the monsoon and early post-monsoon periods. The vertical profiles retrieved from MAX-DOAS measurements show that the major fraction of the NO<sub>2</sub> column is lo-

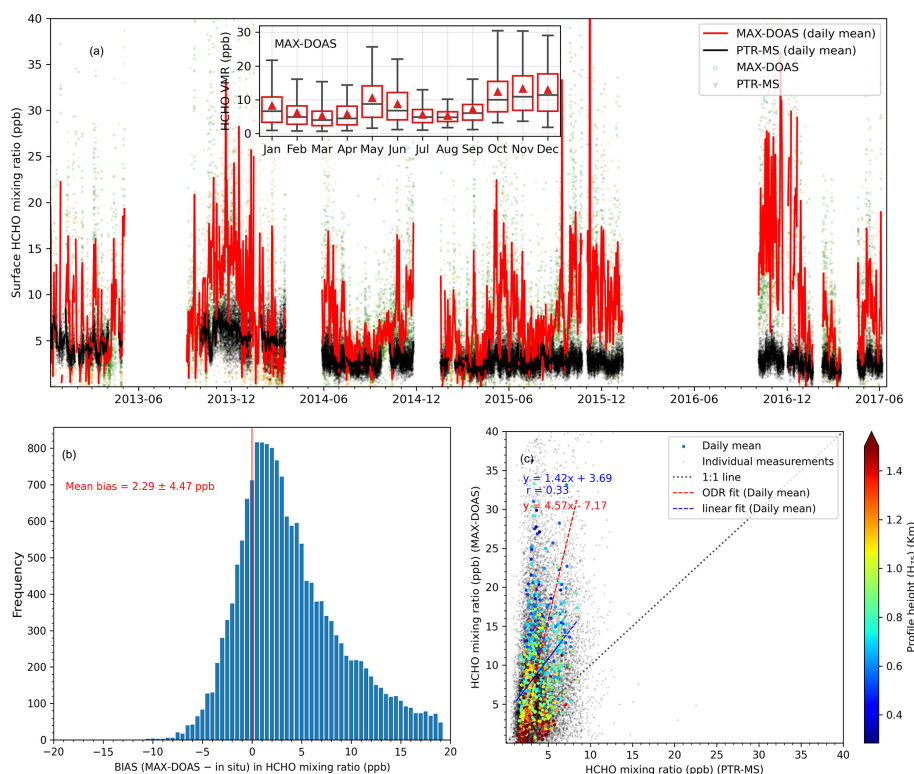


**Figure 13.** (a) Daily mean HCHO mixing ratios measured using an in situ chemiluminescence analyser (black line) and average mixing ratio in the lowest layer (0–200 m) retrieved by the profile inversion of MAX-DOAS measurements (red line). The green and orange dots in the background show the mixing ratios corresponding to the individual MAX-DOAS elevation sequences flagged as valid and warning, respectively. The inset of (a) shows the monthly variability of the MAX-DOAS surface HCHO VMR as a box-and-whiskers plot; (b) shows the frequency distribution of the BIAS (MAX-DOAS – in situ) for the individual surface VMR measurements; (c) shows the scatter plot between the daily mean surface HCHO VMR from MAX-DOAS and PTR-MS colour-coded according to the profile height ( $H_{75}$ ). The individual measurements are shown as black dots in the background of (c).

cated close to the surface (0–200 m) in all the seasons, while the same is true for HCHO only in winter. In other seasons, comparable HCHO mixing ratios are also observed in higher layers until 600 m indicating active photochemistry at higher altitudes. Interestingly, the seasonal variation in the vertical profiles of aerosol extinction did not depend on the significant change in the ERA5 boundary layer heights between summer and monsoon. In addition to serving as an input for the retrieval of VCDs from the preliminary satellite data analysis, vertical profiles retrieved from MAX-DOAS measurements can also be used to validate the regional atmospheric chemistry models around the measured location.

We observed a very good agreement in the temporal trend, and a slight overestimation by the high-resolution MODIS MAIAC data product around Mohali with respect to the AOD retrieved from MAX-DOAS O<sub>4</sub> measurements. The OMI aerosol data product “OMAERUV” generally underestimated the AOD at Mohali compared to MAX-DOAS, and the accountability is also not as good as for the MAIAC product. In an ideal case, sun photometer measurements, which provide AOD at 360 nm, are best suited for an intercompar-

ison with the MAX-DOAS measurements. However, such measurements were not available at our measurement location, and for future studies, sun photometer measurements are recommended for a direct comparison of the AOD at 360 nm. We use the MAX-DOAS measurements of NO<sub>2</sub> and HCHO to evaluate the three widely used NO<sub>2</sub> data products (DOMINO v2, QA4ECV, and OMNO2) and two HCHO data products (QA4ECV and OMHCHO) of OMI for the first time over India and the Indo-Gangetic Plain. Among the three OMI NO<sub>2</sub> data products, we observe reasonable agreement between MAX-DOAS and OMI for the latter two. However, all three OMI data products underestimate the MAX-DOAS NO<sub>2</sub> VCDs by 30 %–50 %. The maximum discrepancy is observed in late post-monsoon and in the winter months when a large amount of trace gases and aerosol is trapped in the air close to the surface. A major reason behind the discrepancy between the MAX-DOAS and OMI observations is the inaccurate representation of the a priori NO<sub>2</sub> profiles and aerosol profiles used for the calculation of air mass factors in satellite retrievals. If we account for the decreased satellite sensitivity close to the ground, a smaller bias is observed between the

MAX-DOAS and OMI NO<sub>2</sub> VCDs. Because of their large ground footprint, OMI measurements are representative of a larger area around the MAX-DOAS measurement site, which is also responsible for part of the discrepancy. Two OMI data products of HCHO are also compared against MAX-DOAS observations. The QA4ECV HCHO product was found to exceed the MAX-DOAS HCHO VCDs by ~ 30 % overall, whereas a generally good agreement was found with the OMHCHO data product. Using the ratio of HCHO and NO<sub>2</sub> VCDs measured from MAX-DOAS, we found that the daytime ozone production is sensitive towards NO<sub>x</sub> in summer, monsoon, and post-monsoon, whereas a strong sensitivity towards both NO<sub>x</sub> and VOCs was observed in winter. We observed a transition from stronger VOC sensitivity to stronger NO<sub>x</sub> sensitivity on ozone production from morning to late afternoon.

The mean surface VMRs of NO<sub>2</sub> and HCHO retrieved from MAX-DOAS observations for the measurement period were  $8.2 \pm 6.7$  ppb and  $8.7 \pm 7.5$  ppb, respectively. We have compared the surface volume mixing ratios retrieved from MAX-DOAS measurements with those measured using in situ analysers. The temporal intraday and the day-to-day variations in the NO<sub>2</sub> surface VMR agree well for both measurements, but the MAX-DOAS measurements were generally higher than those measured using the in situ analysers, with a bias of  $0.67 \pm 2.85$  ppb. For HCHO, however, a poorer agreement in the temporal trend and a large bias of  $2.29 \pm 4.47$  ppb was observed between MAX-DOAS and in situ measurements. The observed differences can be mainly attributed to the differences in vertical and horizontal representativeness of both the measurements. The MAX-DOAS surface VMRs are representative of trace gases (e.g. HCHO or NO<sub>2</sub>) located from the surface to altitudes of up to a few hundred metres. We found evidence of vertical gradients of photochemically formed compounds and hence stronger differences were observed when a significant fraction of trace gases is present at altitudes higher than the inlet of in situ analysers.

MAX-DOAS instruments can provide stand-alone routine measurements of trace gases and aerosol from remote locations, which can be further employed for air quality assessment, similar to the AERONET global network. (e.g. PANDORA, NDACC: <https://www.ndaccdemo.org/instruments/uv-visible-spectrometer>, last access: 17 November 2020). A plethora of studies related to satellite observations of tropospheric pollutants from China and western countries have sensitized the authorities to reduce emissions to curb the pollution (de Foy et al., 2016). MAX-DOAS measurements were of substantial importance to validate and complement the satellite observations in these studies. With the Indian subcontinent being projected as the new hotspot of anthropogenic emissions (Li et al., 2017; De Smedt et al., 2018), similar (or new generation, e.g. TROPOMI, GEMS) satellite and corresponding MAX-DOAS observation will be of great importance for future studies.

### Appendix A: A performance of the NO<sub>2</sub> retrieval in the UV and visible spectral range and comparison of the NO<sub>2</sub> VCD obtained from the profile retrievals to the results from the geometric approximation

The DOAS spectral analysis and profile inversion have been performed both in the UV and visible spectral ranges. As mentioned in Sect. 2.2 of the main text and also shown in Fig. A1 for a smaller subset of data from 2015, the analysis in the UV results in larger fit uncertainties, which eventually leads to a poorer performance of the profile inversion.

For an elevation angle sequence, MAPA finds the best fit of the model dSCDs by minimizing the difference compared to the measured dSCDs. The difference is quantified by the rms ( $R$ ), which is defined as

$$R = \sqrt{\frac{(S_{\text{fm}} - S_{\text{ms}})^2}{N_{\text{eas}}}}. \quad (\text{A1})$$

Here  $S_{\text{fm}}$  and  $S_{\text{ms}}$  represent dSCDs sequences from model and measurements and  $N_{\text{eas}}$  represents the number of elevation angles in the measurement sequence. Warning and error flags are raised for the retrieved profile if the following two conditions are fulfilled:

1.  $R_{\text{bm}}$  (rms for the best matching model dSCD) exceeds the sequence median dSCD uncertainty.
2.  $R_n$  (the ratio of  $R_{\text{bm}}$  and maximum dSCD of a sequence) exceeds the predefined thresholds (Beirle et al., 2019).

The larger fit uncertainties of the NO<sub>2</sub> analysis in the UV directly result in larger errors in the NO<sub>2</sub> dSCDs. These larger errors lead to larger residuals and hence larger  $R_{\text{bm}}$ , leading to more flagged sequences. Here we check if the threshold for  $R_n$  can be relaxed from that (0.05) recommended by Beirle et al. (2019) for the NO<sub>2</sub> retrieval in the UV while still retaining reasonable retrievals. We have calculated the total retrieval quality flag as described in Sect. 2.8.6 of Beirle et al. (2019) by varying  $R_n$  from 0.05 to 0.15. A larger  $R_n$  leads to a larger number of retrievals being flagged as valid. The retrieved VCDs and concentrations in the layer closest to the surface derived in the UV for different  $R_n$  values are compared to those in the visible as reference. We find that increasing  $R_n$  from 0.05 to 0.15 for the UV retrieval almost doubles the number of valid retrievals while keeping similar statistical agreement as compared to Vis retrievals. From Fig. A2, we see that the slope of the linear regression of the NO<sub>2</sub> VCDs between UV and Vis remains close to 0.95, while the correlation coefficient ( $r$ ) only changes from 0.91 to 0.89. Similar results are obtained for the surface concentration, where the slope of the linear regression and correlation coefficient ( $r$ ) only slightly change from 0.87 and 0.94 to 0.85 and 0.93, respectively.

For several years, the geometric approximation has been used for the calculation of VCDs from the dSCDs retrieved

from DOAS spectral analysis. If only the photon light path is taken into account with the assumption that the last scattering event before the photon reached the telescope of the instrument has happened above the trace gas layer, the geometric air mass factors for an elevation angle  $\alpha$  can be calculated trigonometrically:

$$\text{AMF}_{\alpha, \text{Geo}} = \frac{1}{\sin \alpha}. \quad (\text{A2})$$

Since the geometric approximation relies on the single scattering approximation above the trace gas layer, it is expected to work well under clear-sky conditions with low aerosol loads and for trace gases confined to layers close to the surface. Generally, there is a trade-off between the sensitivity and validity of geometric approximation for the choice of elevation angle. At low-elevation angles, though the measurements are more sensitive, the probability of scattering within the trace gas layer is rather high. We have chosen an elevation angle of 15° for the calculation of geometric VCDs. Several studies (Bösch, 2018; Wagner et al., 2011; Jin et al., 2016) have shown that the geometric VCDs usually agree within 20% to the VCDs that are retrieved using radiative transfer simulations if the trace gas is not located at higher altitudes (> 1000 m) and trace gas is confined within the aerosol layer. In Fig. A3, we compare the VCDs calculated from the geometric approximation and from valid MAPA retrievals for various sky conditions, both for NO<sub>2</sub> in the UV and visible and for HCHO (in the UV).

As expected, we see an excellent agreement between the NO<sub>2</sub> geometric VCDs and those retrieved from the profile inversion in clear-sky conditions with low aerosol load both for the UV and visible retrievals. The level of agreement is still reasonable in high aerosol conditions and cloudy cases; however, for such conditions, the geometric VCDs are systematically lower. This finding is in line with that observed by Wagner et al. (2011). It indicates the effect of photon scattering within the trace gas layer. We also observe that the agreement of NO<sub>2</sub> VCDs between geometric approximation and profile inversion is better for the UV than for the visible retrieval. If we chose a 30° elevation angle for the calculation of the geometric VCDs, reasonable agreement ( $r > 0.9$ ) with the VCDs retrieved from profile inversion is observed only for the visible retrievals. For the NO<sub>2</sub> retrievals in the UV, reasonable agreement ( $r = 0.86$ ) was observed for clear sky with low aerosol load, but a larger scatter ( $r < 0.8$ ) is found for clear-sky conditions with high aerosol load and for cloudy-sky conditions.

Similar to NO<sub>2</sub>, we also observe the best agreement for the HCHO VCDs retrieved using the geometric approximation and those using the profile inversion for clear-sky conditions with low aerosol load. For high aerosol loads and cloudy-sky conditions, the VCDs from the geometric approximation are significantly lower. In contrast to NO<sub>2</sub>, a significant fraction of formaldehyde is usually found in higher layers, which limits the validity of geometric approximation. The bias gets

higher for HCHO VCDs greater than  $\sim 1.5 \times 10^{16}$  molecules  $\text{cm}^{-2}$ . If we chose observations at a 30° elevation angle for the calculation of the geometric VCD, lower correlation with the VCDs retrieval using the profile inversion was observed ( $r < 0.8$ ) for all sky conditions.

We also checked the internal consistency of the NO<sub>2</sub> dSCDS retrieved from the DOAS analysis in the UV and visible. For the comparison, even for a geometric approximation, we only consider those sequences for which the profile retrieval was flagged valid. From Fig. A3 (panels j–l), we see that in clear-sky cases, NO<sub>2</sub> VCDs from the geometric approximation in the visible are systematically higher than those retrieved in the UV. The Rayleigh scattering probability is inversely proportional to the fourth power of the wavelength, and therefore in the UV, the higher scattering probability results in shorter light paths within the trace gas layer. Since the AMFs from the geometric approximation are independent of the wavelength, the shorter dSCDS results in smaller VCDs from the geometric approximation in the UV. The radiative transfer models, however, account for different path lengths in UV and the visible. Hence, the VCDs retrieved using MAPA do not show any systematic bias in UV or the visible (Fig. A2). It is interesting to note that the difference in the NO<sub>2</sub> VCDs retrieved from the geometric approximation in the UV and visible is much smaller for cloudy-sky conditions. For such conditions, the differences in the light path lengths in the UV and visible are usually much smaller than for clear-sky conditions.

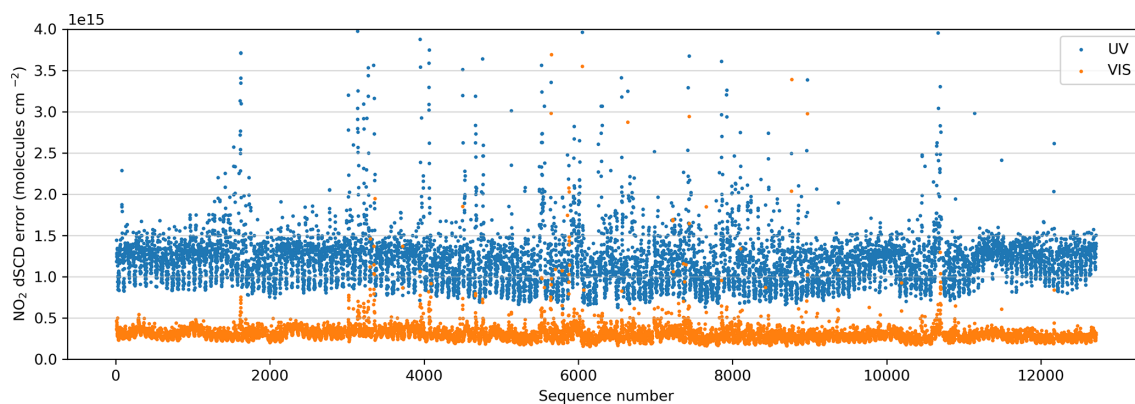


**Figure A1.** DOAS fit errors of the NO<sub>2</sub> retrievals in the UV and visible wavelength windows.

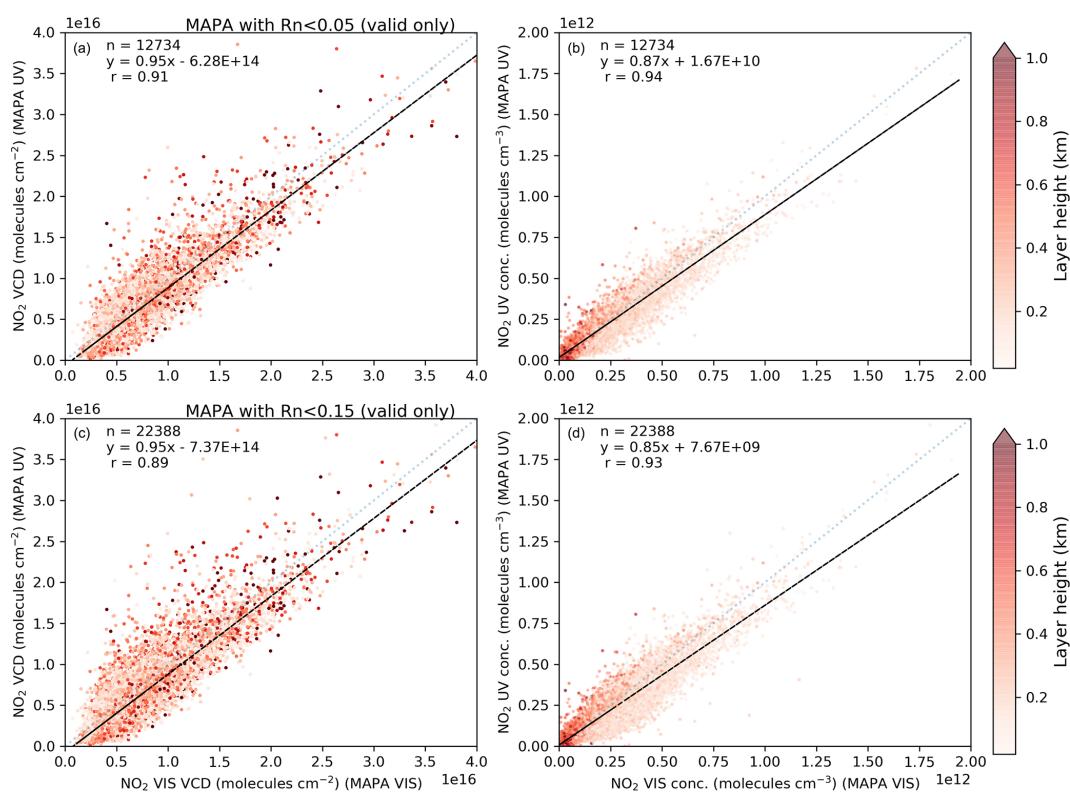


**Figure A2.** Comparison of NO<sub>2</sub> VCDs (a, c) and surface concentrations (b, d) retrieved in the UV against those retrieved in the visible. Please note that the number of valid data points shown in this figure corresponds to the number of valid overlapping retrievals in UV and the visible. The number of valid retrievals for NO<sub>2</sub> in UV shown in Table 2 corresponds to the  $R_n$  flag with a threshold <0.15.

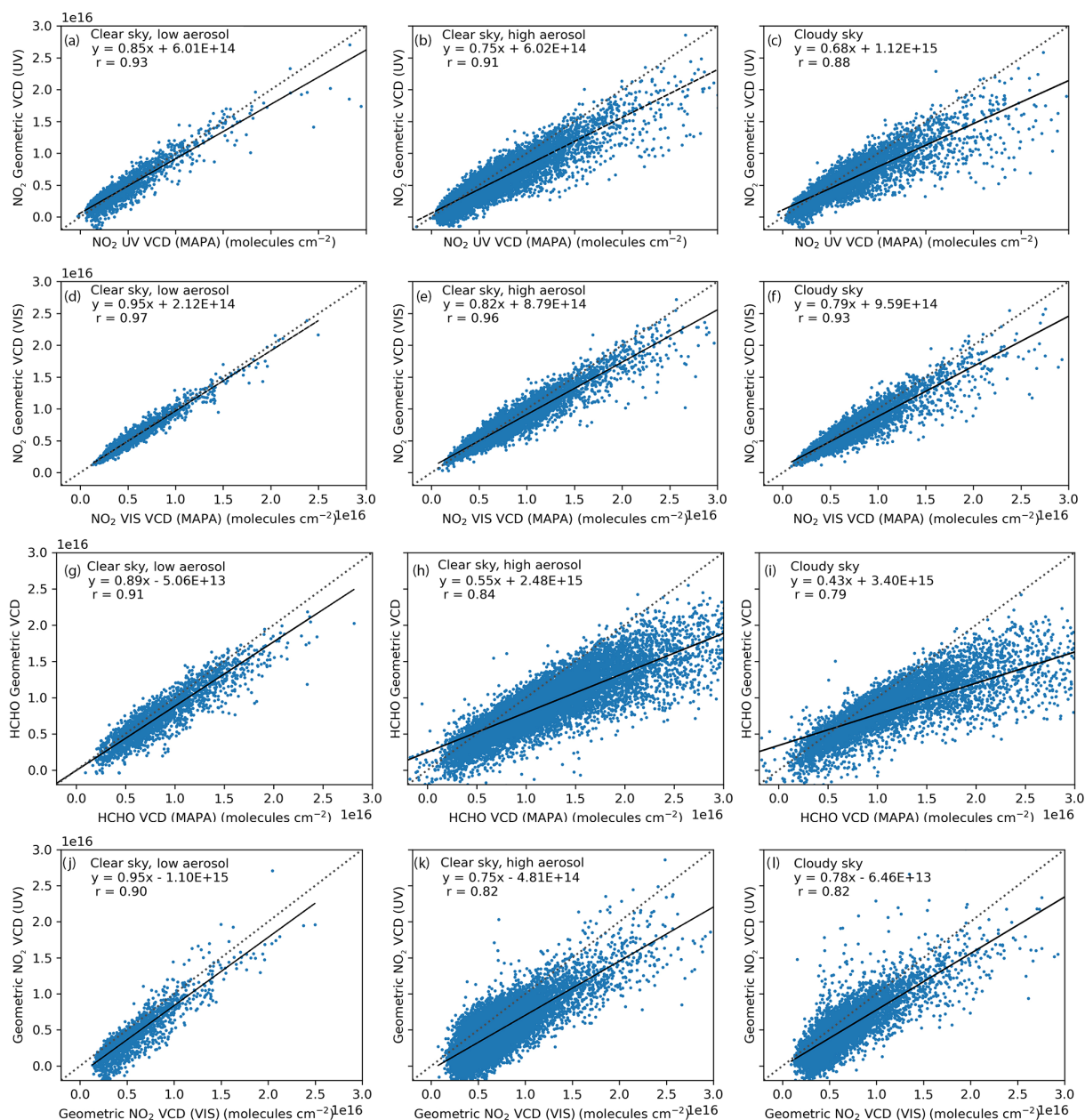


**Figure A3.** Comparison of VCDs calculated using the geometric approximation at 15° elevation angle and that calculated using MAPA for NO<sub>2</sub> in the UV (top row), NO<sub>2</sub> in the visible (second row), and HCHO (third row) for various sky conditions: clear sky with low aerosol load (left), clear sky with high aerosol load (middle), and cloudy-sky conditions except for thick clouds and fog (right). The bottom row shows the comparison of NO<sub>2</sub> VCD calculated using the geometric approximation for spectral analyses in the UV and visible for the three different sky conditions.

## Appendix B: Identification of thick clouds

For the identification of thick clouds, Wagner et al. (2016) proposed the use of an absolute calibration method for the O<sub>4</sub> absorption in the Fraunhofer reference spectrum. However, this method can only be applied for relatively short time periods, over which the spectral properties of the MAX-DOAS instrument stay almost the same. For the measurements used in this study, this method cannot easily be applied because the spectral properties of the Mini-MAX-DOAS instruments are known to vary rather strongly even within rather short periods of time (a few days to weeks). In addition, for the measurements used in this study, the detector temperature had to be changed frequently according to the seasonal variation in the ambient temperature. Therefore, it was impossible to create a consistent time series of absolutely calibrated measured O<sub>4</sub> absorption over the complete measurement period. Therefore, the identification of thick clouds was performed based on the measured radiances (Wagner et al., 2014; Wang et al., 2015)

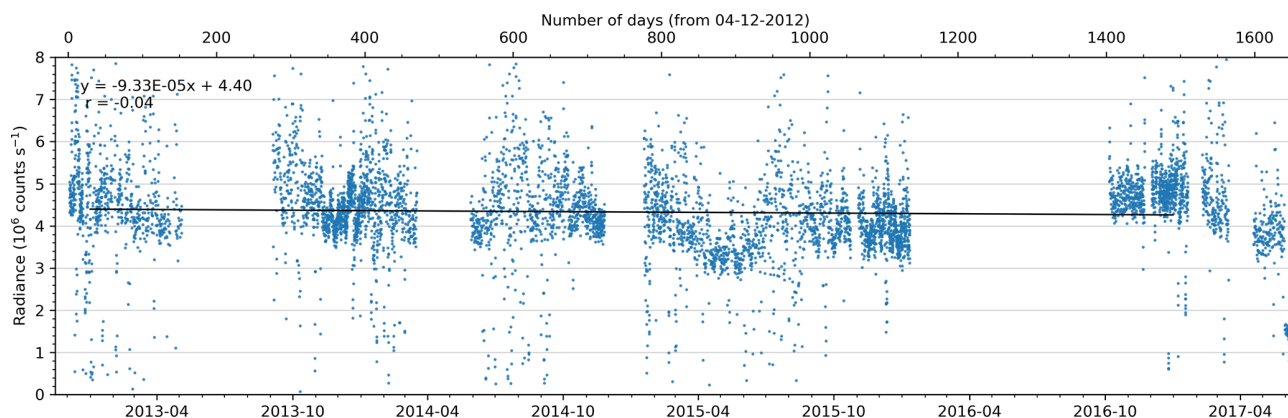
While optically thin clouds often lead to an increase in the measured radiance, optically thick clouds lead to a strong decrease (compared to clear-sky radiance). However, such an approach can only be applied if there is no significant degradation in the measured radiance over the whole measurement period. Figure B1 shows the time series of the measured radiances (at 360 nm) for an SZA interval between 55 and 60°. A significant decrease is not observed in the measured radiance during measurement period of more than 4 years, except for the intra-annual seasonal variation. Hence, we can use the measured radiance for the identification of thick clouds. Please note that the strongly increased values of the radiances are caused by optically thin clouds. Note that the linear trend was fitted only for the period from 1 January 2013 to 31 December 2016 to minimize the impact of the seasonal variation.

In order to identify the optically thick clouds, the measured radiances in the zenith direction have to be compared to an SZA-dependent reference value (see Wagner et al., 2014 and 2016), which is obtained from RTM simulations for a well-defined atmospheric scenario. However, as these instruments are usually not radiometrically calibrated, the measured radiances cannot be directly compared to the reference radiances derived from the RTMs. Hence, we first have to perform a calibration of measured radiances.

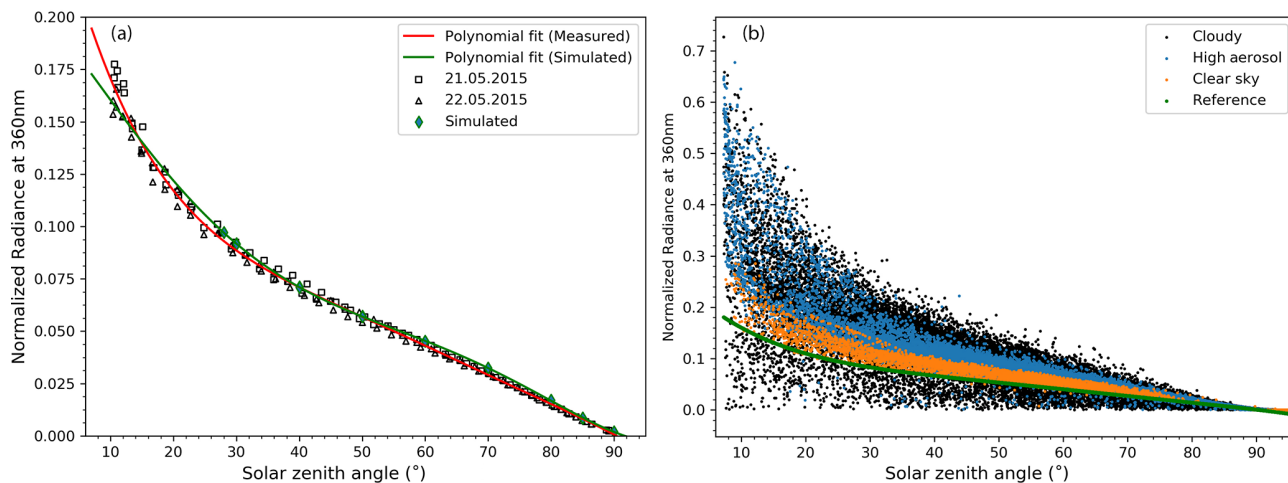
For the calibration, we first calculated the radiance in the zenith direction at 360 nm for an SZA range between 7 and 95° using the RTM McARTIM (Deutschmann et al., 2011). The simulations are done for an AOD = 0.3, aerosol particles properties as proposed by Wagner et al. (2014) and a surface albedo of 5%. In the next step, 2 clear days in summer (such that the measurements are available even at solar zenith angles less than 10°) with AOD (at 360 nm) close to 0.3 (as measured by MODIS) are selected. By comparing the SZA dependence of the measured radiances with the simulated radiances (Fig. B2), we determined the calibration factor to be  $1.48 \times 10^{-8}$  counts<sup>-1</sup> for our measurements. Here it should be noted that from the similar relative SZA dependences of the measured and simulated radiances at larger SZA, we can conclude that the AOD at 360 nm was similar to 0.3.

Figure B2a shows the variation in the calibrated measured radiances on the 2 selected days and the polynomial fit of the simulated radiances as a function of the SZA. It should be noted that in contrast to Wang et al. (2015), we have observed good agreement between the measured and simulated radiances even for solar zenith angles less than 40°. In the study by Wang et al. (2015) in Wuxi, the disagreement was attributed to a possible deviation from the parameterized Henyey–Greenstein aerosol phase function. For Mohali, a better agreement is probably related to the presence of a different aerosol type compared to that in Wuxi. A single fifth-order polynomial was fitted to the calibrated measured radiances in the complete SZA range to derive an SZA-dependent function of the clear-sky normalized radiance, which is subsequently used as an SZA-dependent reference.

For the identification of thick clouds, we have used a threshold of 0.94 times the SZA-dependent threshold radiance similar to Wang et al. (2015). In order to check the consistency of the thick-cloud identification using the normalized radiances, we have also performed thick-cloud identification based on the O<sub>4</sub> AMFs as described by Wagner et al. (2016) for a small period in July 2014. Figure B3 shows an excellent consistency of the thick-cloud identification using the two methods. In panel a, the periods having smaller radiances than the threshold show larger O<sub>4</sub> AMFs than the respective threshold in the bottom panel.



**Figure B1.** Time series of the measured radiances at 360 nm derived from the MAX-DOAS measurements in the zenith viewing direction for SZA between 55 and 60°. Please note that the trend is calculated only for the measurements from 1 January 2013 to 31 December 2016 to minimize the effect of seasonal variation. The dark black line indicates the linear regression of the measured radiance as a function of day number.



**Figure B2.** Dependence of the measured and simulated radiances in zenith direction (at 360 nm) on the solar zenith angle for the 2 selected days (a). Panel (b) shows all measured normalized radiances (after calibration) in zenith direction, colour-coded for three sky conditions: black – cloudy sky; orange – clear sky with low aerosol load; blue – clear sky with high aerosol load. All measurements corresponding to thick clouds lie below the threshold (shown as green curve) in (b).

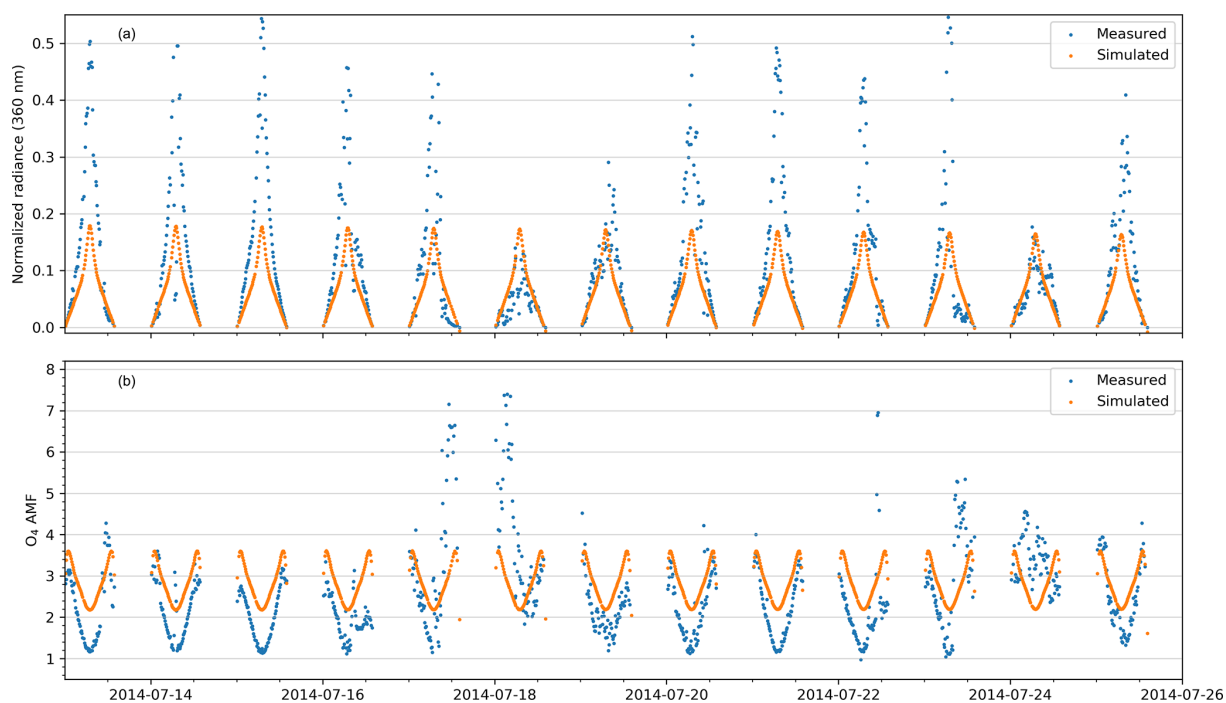


**Figure B3.** (a) Measured calibrated radiances in the zenith direction and (b) O<sub>4</sub> AMFs derived for zenith direction for a selected short period of the measurements, over which the instrument properties were almost constant. Also shown are the simulation results for the SZA-dependent thresholds. On some days greatly enhanced O<sub>4</sub> AMFs are found, indicating the presence of optically thick clouds. On these days, greatly decreased radiances are also measured.

## Appendix C: Satellite data products used for comparison against MAX-DOAS measurements

### C1 OMAERUV

The OMAERUV algorithm uses the Lambert equivalent reflectivity (LER) calculated from the measured radiance at 388 nm to first yield the AODs and aerosol absorption optical depth (AAOD) at 388 nm. Subsequently, using an inherent aerosol model, the AOD at 354 and 500 nm are calculated (Torres et al., 2007). The OMAERUV V1.8.9.1 product used in this study also provides an indicator for the data quality named “FinalAlgorithmFlags” corresponding to every measurement. For the intercomparison in this study, we have only retained the data corresponding to a “FinalAlgorithmFlags” value of 0, which represent the most reliable retrievals of AOD.

### C2 DOMINO V2

The DOMINO version 2.0 NO<sub>2</sub> product (Boersma et al., 2011) makes use of the measurements in the 405–465 nm wavelength interval. The NO<sub>2</sub> SCD retrieved by employing the DOAS technique in the first step is separated for stratospheric and tropospheric composition. The DOAS fit includes the absorptions due to NO<sub>2</sub>, O<sub>3</sub>, O<sub>4</sub>, H<sub>2</sub>O (l), H<sub>2</sub>O (g), and the Ring effect. Subsequently, the tropospheric SCD is converted into the tropospheric VCD using the tropospheric air mass factors. Both the calculation of the air mass factor using a radiative transfer model and the estimation of the stratospheric NO<sub>2</sub> uses the NO<sub>2</sub> fields from a 3° × 2° spatial resolution global chemistry transport model TM4.

### C3 OMNO2 v 3.0

The OMNO2 algorithm developed by NASA (Marchenko et al., 2015) uses the 402–465 nm fit window for the NO<sub>2</sub> retrieval. In the first step, the wavelength calibration and Ring correction are performed in seven sub-windows within the spectral range. The DOAS fit involves an iterative process, in which first a preliminary estimate of NO<sub>2</sub>, H<sub>2</sub>O, and glyoxal is made using fits in smaller sub-windows of the full spectral range of 402–465 nm. The absorption due to this initial estimate is used for the determination of instrumental noise in the original spectrum. The noise-corrected spectrum in the next stage is again subjected to a DOAS fit including the absorptions from NO<sub>2</sub>, H<sub>2</sub>O (g), glyoxal, and the Ring effect in the 402–465 nm spectral range to retrieve the NO<sub>2</sub> SCDs. A stratospheric correction is applied, and air mass factors are applied to retrieve the tropospheric NO<sub>2</sub> VCDs. The NO<sub>2</sub> a priori vertical profiles used for the calculation of the AMF are taken from the climatology of the 4-year-long global model initiative (GMI) 2° × 2.5° spatial resolution chemistry transport model simulation. The cloud information is incorporated from the external OMCLDO2 product, which calculates the cloud fraction using the contrast in measured radiances be-

tween clear and cloudy pixels. The cloud pressure (an indicator of cloud height) is calculated using the O<sub>4</sub> absorption at 477 nm.

### C4 QA4ECV

In this work, we also use the OMI QA4ECV (quality assurance for essential climate variables) data product for NO<sub>2</sub> (Boersma et al., 2018) and HCHO (De Smedt et al., 2018) for comparison with respective MAX-DOAS measurements. The DOAS retrieval of NO<sub>2</sub> SCDs uses a similar wavelength window and absorbers as DOMINO v2 but includes an additional intensity offset. Also, an optical depth fit is performed in place of an intensity fit. While for DOMINO the wavelength calibration was performed prior to the fit in the 409–428 nm window, for QA4ECV, it is performed along with the DOAS fit in the 405–465 nm wavelength window. The most significant improvement in the QA4ECV NO<sub>2</sub> retrieval concerns the AMF calculation and the stratospheric background correction. QA4ECV uses the 1° × 1° spatial resolution TM5 model for the calculation of a priori NO<sub>2</sub> profiles. In several studies, QA4ECV NO<sub>2</sub> products are shown to have a better agreement with ground-based measurements and a smaller uncertainty than the other OMI NO<sub>2</sub> data products (Boersma et al., 2018; Chan et al., 2019; Zara et al., 2018).

The QA4ECV HCHO algorithm performs a DOAS optical depth fit including HCHO, O<sub>3</sub>, BrO, NO<sub>2</sub>, O<sub>4</sub>, and the Ring effect in the wavelength interval 328.5–359 nm to obtain the HCHO SCDs (Zara et al., 2018). The across-track stripes observed in the retrieved dSCDs are corrected by subtracting an OMI detector row-dependent mean equatorial pacific HCHO SCD. The a priori vertical profiles of HCHO are also calculated using the 1° × 1° spatial resolution TM5 model.

### C5 OMHCHO

The OMHCHO v003 (González Abad et al., 2015) is a level 2 formaldehyde data product from NASA. The HCHO slant column densities are retrieved by employing a DOAS intensity fit in the 328.5–356.5 nm wavelength window, which includes the absorptions from HCHO, O<sub>3</sub>, NO<sub>2</sub>, BrO, O<sub>4</sub>, and the Ring effect. Similar to OMNO2, the air mass factor for the conversion of the SCD into the VCD is calculated by considering climatological HCHO vertical profiles. The cloud information is also taken from the OMCLDO2 product. In order to account for the observed across-track stripes in the VCD, a normalization is performed with respect to the GEOS-Chem model calculated monthly climatological means over the remote Pacific.

### C6 MAIAC

The collection 6 MCD19A2 level 2 gridded product from MODIS provides the 1 × 1 km<sup>2</sup> spatially resolved AOD at 470 and 550 nm based on the MAIAC (Multi-Angle Implementation of Atmospheric Correction) algorithm. In contrast

to previous swath-based retrievals for individual ground pixels, the MAIAC algorithm grids the L1B top-of-atmosphere reflectance in  $1 \times 1 \text{ km}^2$  predefined sinusoidal grids prior to further processing. For each grid, data up to 16 d are accumulated, which include measurements at various viewing geometries from different orbits. The AOD retrieval relies on the ratio of measured spectral regression coefficients (SRC) at Band3 (459–479 nm)/Band7 (2105–2155 nm) and Band3/Band4 (545–565 nm). The analysis of time series of SRC enables the separation of the relatively static surface properties and fast varying atmospheric properties (e.g. AOD).

To generate a time series of AOD for comparison with MAX-DOAS, we have extracted the MODIS data spatially averaged within 2 km of the measurement location in Mohali. We have assumed a linear dependence between the logarithms of the wavelength and the AOD in the wavelength range 360 and 550 nm to convert the MODIS AOD measured at 470 nm using the Ångström exponent calculated according to Eq. (3). We have only retained the highest-quality MODIS AOD measurements corresponding to a QA value of “0000” in bits 8–11 provided in the MAC19A2 dataset (Lyapustin et al., 2018). This criterion removes all the data contaminated by clouds and those adjacent to cloudy pixels.

#### Appendix D: Evaluation of the air mass factors and a priori profiles in the OMI retrievals

The sensitivity of satellite instruments is usually characterized by the so-called bAMF profiles (Eskes and Boersma, 2003). bAMFs can be regarded as the air mass factors for discrete atmospheric layers. They can be integrated from the surface until the tropopause (Trop), weighted by the trace gas profile, according to the following equation to get tropospheric air mass factors.

$$\text{AMF}_{\text{Trop}} = \sum_{i=0}^{\text{Trop}} \text{bAMF}_i \frac{\text{VCD}_i}{\text{VCD}_{\text{Trop}}} \quad (\text{D1})$$

The vertical profiles of trace gases and aerosol extinction are a piece of important information needed to derive VCDs from the satellite measurements. Due to the absence of such measured information, global chemistry, usually transport, models (e.g. a coarse  $2.5^\circ \times 2.5^\circ$  spatial resolution TM4 for DOMINO and finer  $1^\circ \times 1^\circ$  spatial resolution TM5 for QA4ECV) are employed. From Eq. (D1) it is evident that if a relatively small fraction of an absorber (for e.g. NO<sub>2</sub>) is located close to the ground in the a priori profiles, the resulting AMFs become positively biased and, finally, the VCDs become negatively biased. The finer horizontal resolution of the a priori NO<sub>2</sub> profiles in the QA4ECV product probably results in a more accurate representation of the NO<sub>2</sub> vertical profiles, especially close to strong emission sources like Mohali, and thus improves the retrieved NO<sub>2</sub> VCD.

In order to further investigate the underestimation (in particular late post-monsoon and winter months), we first calculate the box air mass factors (with the RTM McARTIM) at 30° SZA over Mohali using mean aerosol extinction profiles (Fig. F16) retrieved from MAX-DOAS measurements and compare them with bAMFs used for the DOMINO and QA4ECV NO<sub>2</sub> retrievals. We perform this comparison for September (representative of early post-monsoon or clean conditions), October, and November (representative of late post-monsoon and winter, respectively) (Fig. D1). Two striking features are observed:

1. The overall vertical variability of the bAMFs is different in the satellite products compared to the bAMF calculated for the MAX-DOAS aerosol profiles. The calculated bAMFs indicate a rather sharp increase with altitude until the first 1000 m.
2. The calculated bAMFs show systematically higher values close to the surface than those used in the satellite retrievals. The largest underestimation is found for the DOMINO bAMF, which uses the rather coarse TM4 model input.

The smaller bAMF of the satellite product in the lower layers indicates a smaller weight of these layers where a major fraction of NO<sub>2</sub> is present. Hence, the AMFs will become smaller and the VCDs become higher if the relative a priori NO<sub>2</sub> profiles for satellite data retrieval are adjusted to the observed profiles. However, if the a priori profiles assume a smaller fraction of NO<sub>2</sub> in layers close to the surface, higher layers will get a larger weight in Eq. (D1), resulting in larger AMF and smaller VCD. Hence, in the next step, we compare the a priori NO<sub>2</sub> profiles of the satellite data product with those retrieved from MAX-DOAS measurements. Unfortunately, our comparison is limited to the DOMINO product, as the a priori NO<sub>2</sub> profiles are not available for the other products.

Figure D2 shows monthly mean relative vertical profiles of NO<sub>2</sub> retrieved by MAX-DOAS and the corresponding TM4 profiles. We can clearly notice two differences:

1. The vertical gradient in the relative profile shape is stronger in the MAX-DOAS profiles than in the TM4 product.
2. The TM4 relative a priori shape is somewhat similar in all months, whereas the profile shape retrieved from DOAS changes strongly with season. More than half of the NO<sub>2</sub> is located in the bottom-most layer in the winter months.

The consequence of the first observation is that the total air mass factors will generally be higher if the TM4 profiles are used as a priori, which results in smaller VCDs as also observed in Fig. 8. The consequence of the second observation

is that in the winter months, the discrepancy due to the a priori profile is even stronger, resulting in a larger disagreement with the measured MAX-DOAS VCDs.

Accurate satellite AMFs can be recalculated using MAX-DOAS vertical profiles as a priori, which could improve the agreement with MAX-DOAS observations as also shown by De Smedt et al. (2015). The satellite AMFs corresponding to the MAX-DOAS a priori profiles ( $x_m$ ) can be recalculated according to the following equation:

$$\text{AMF}_{\text{trop}}(x_m) = \text{AMF}_{\text{tot}}(x_a) \frac{\sum_{l=1}^L A_l x_{m,l}}{\sum_{l=1}^L x_{m,l}}. \quad (\text{D2})$$

Here,  $x_a$  is the original satellite (TM5) a priori trace gas profile,  $L$  is the tropopause level index,  $A$  represents the satellite averaging kernels, and  $\text{AMF}_{\text{tot}}$  is the total air mass factor.

Total AMF ( $\text{AMF}_{\text{tot}}$ ) and satellite averaging kernels used for OMI retrievals are crucial information required to recalculate the satellite (OMI) AMF. For NO<sub>2</sub>, only the DOMINO product provides both  $\text{AMF}_{\text{tot}}$  and satellite averaging kernels in the data product. We attempted to recalculate the  $\text{AMF}_{\text{trop}}$  using the MAX-DOAS profiles, but this resulted in very small air mass factors (and very large recalculated OMI VCDs). The small  $\text{AMF}_{\text{trop}}$  is due to the fact that the MAX-DOAS profiles do not account for the background NO<sub>2</sub> in the free troposphere, where the satellite averaging kernels are large. In the next step, we used hybrid profiles such that we only replaced the profiles in the lowest 5 and 2.5 km of the TM5 profile with those retrieved from MAX-DOAS measurements. The observations are summarized in Fig. D3. We note that even with the hybrid approach, there is an overestimation of VCDs for many months. This is probably caused by the incorrect aerosol profiles used for the calculation of the averaging kernels in the satellite analyses.

For formaldehyde,  $\text{AMF}_{\text{tot}}$  is not provided in the QA4ECV products, while averaging kernels are not available for OMH-CHO products. However, we approximated  $\text{AMF}_{\text{tot}}$  to be close to  $\text{AMF}_{\text{trop}}$  because of the negligible amount of HCHO present in the stratosphere. Using this approximation, we have recalculated the modified  $\text{AMF}_{\text{trop}}$  using MAX-DOAS profiles as a priori. Similar to NO<sub>2</sub> we have replaced the profile in the lowest 2.5 km of the TM5 profile with that retrieved from MAX-DOAS measurements. For HCHO, the modified VCDs are largely positively biased. Like for NO<sub>2</sub>, this overestimation might be caused by incorrect aerosol profiles used for the calculation of the averaging kernels in the satellite analyses.

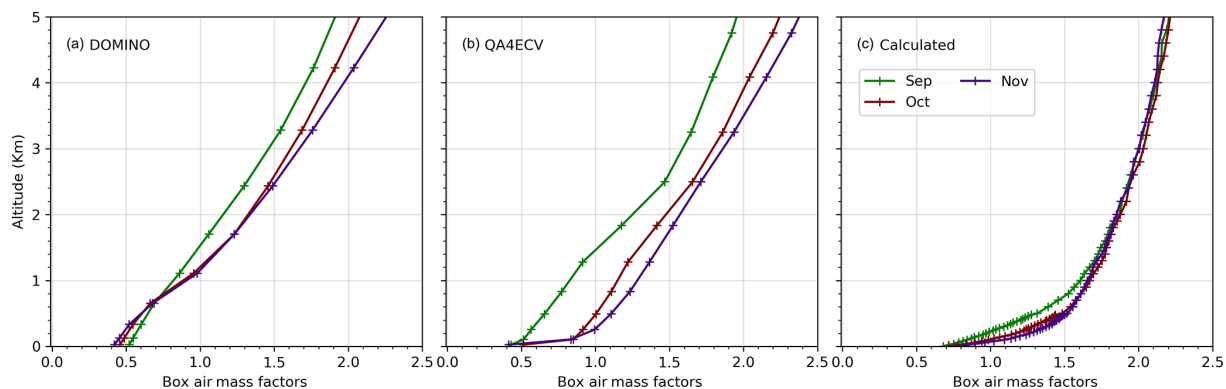


**Figure D1.** Monthly mean box air mass factors used in the DOMINO (a) and QA4ECV (b) NO<sub>2</sub> data products under clear-sky conditions (cloud fraction <0.1) over Mohali for September (when the aerosol load is small) and October and November (when the aerosol load is high close to the surface). Panel (c) shows the corresponding box air mass factors calculated using MAX-DOAS aerosol extinction profiles.

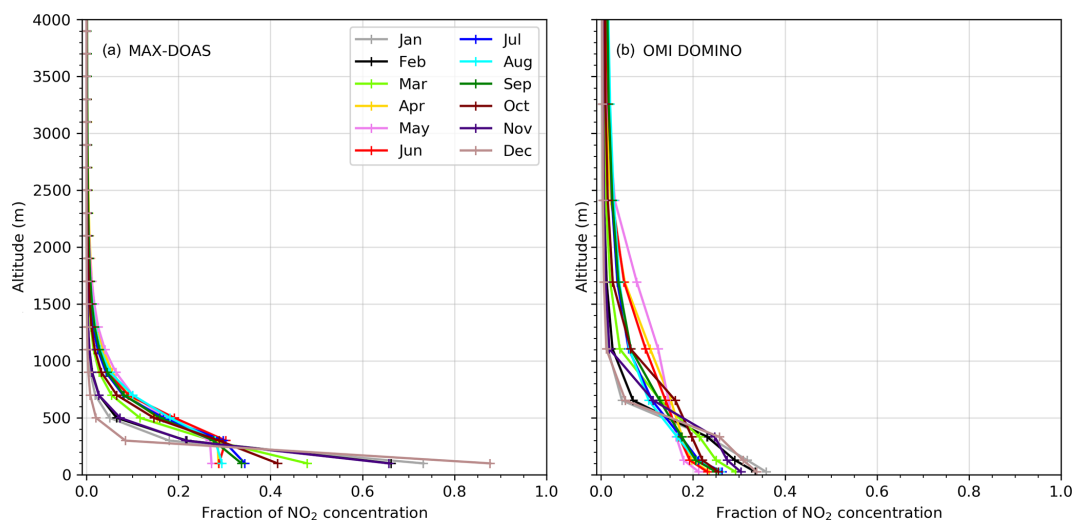


**Figure D2.** Monthly mean relative a priori NO<sub>2</sub> profiles over Mohali retrieved from MAX-DOAS measurements around the OMI overpass time (between 12:30 and 14:30 LT) (a) and the TM4 a priori profiles used for the DOMINO retrieval (b). The a priori profiles are not available for the QA4ECV NO<sub>2</sub> product.

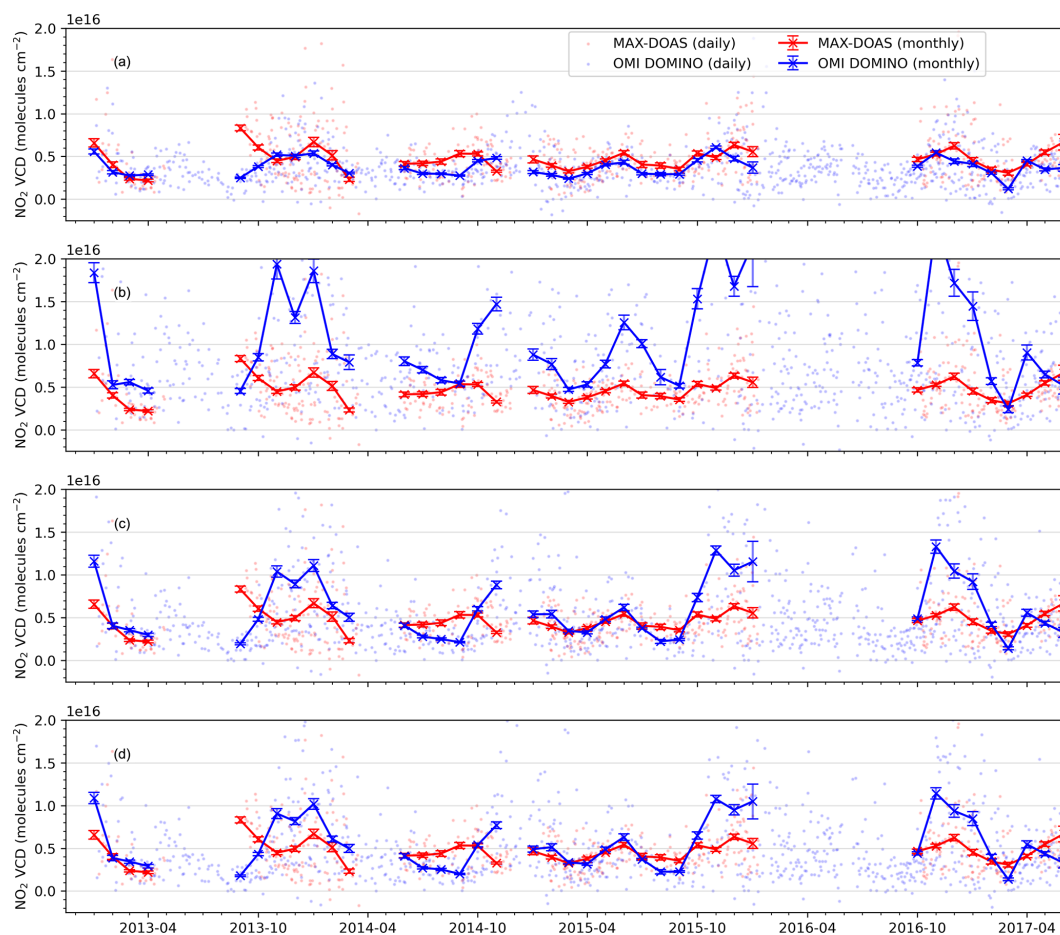


**Figure D3.** Time series of the MAX-DOAS and OMI DOMINO NO<sub>2</sub> tropospheric VCDs for (a) when no modifications in the a priori profiles are applied, (b) when the a priori profiles of DOMINO are replaced by the MAX-DOAS profiles, (c) when the lowest 5 km of the profiles of the a priori are replaced by the corresponding MAX-DOAS profiles, and (d) when the lowest 2.5 km of the profiles of the a priori are replaced by the corresponding MAX-DOAS profiles.

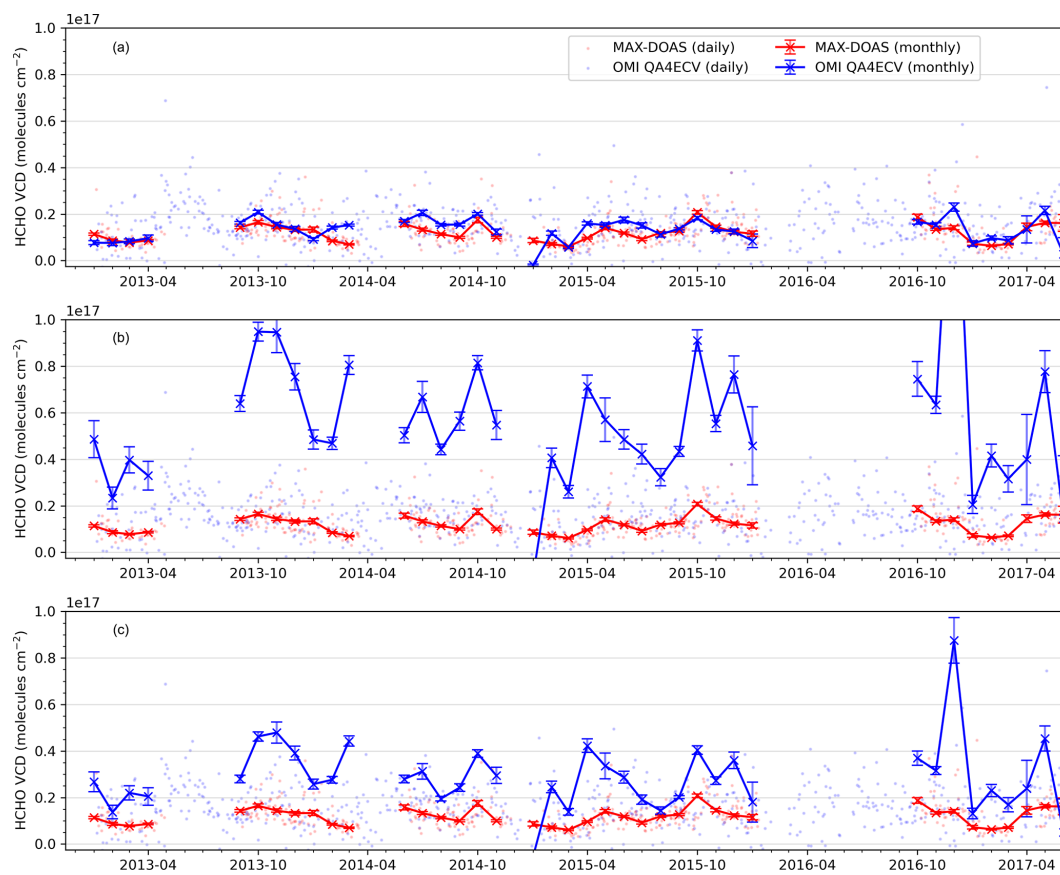


**Figure D4.** Time series of the MAX-DOAS and OMI QA4ECV HCHO tropospheric VCDs for (a) when no modifications in the a priori profiles are applied, (b) when the a priori profiles of QA4ECV are replaced by the MAX-DOAS profiles, and (c) when the lowest 2.5 km of the a priori profiles are replaced by corresponding MAX-DOAS profiles.

### Appendix E: Comparison of surface concentration of NO<sub>2</sub> and HCHO from MAX-DOAS and in situ measurements

In addition to the comparison with the NO<sub>2</sub> and HCHO VCDs from satellite data products, the surface concentration derived from MAX-DOAS is also compared with in situ measurements. From this comparison, a first-order assessment of the quality of the profile retrieval is obtained (Wang et al., 2019; Vlemmix et al., 2015). Often systematic differences of up to 30 % are found between MAX-DOAS and in situ measurements which are mainly related to the limited vertical (and horizontal) resolution of the MAX-DOAS profiles (Vlemmix et al., 2015; Wang et al., 2019; Li et al., 2013). The vertical resolution of the profiles retrieved from MAX-DOAS measurements depends strongly on altitude.

Taking the standard deviation of the daily means into account for an ODR fit further improves the agreement between the MAX-DOAS and in situ measurements of the NO<sub>2</sub> surface VMRs. The frequency distribution of the bias between the two measurements shows a normal distribution which peaks at  $\sim 0.7$  ppb. Please note that in Fig. 12, we have used all profiles which were flagged as valid and warning by MAPA. The linear correlation coefficient ( $r$ ) changes slightly from 0.62 to 0.60 if only valid retrieval results were considered, while for the ODR fit, the slope and intercept change from 0.83 and 1.78 to 0.90 and 1.39, respectively. MAX-DOAS is sensitive towards air masses in the viewing direction of the instrument, whereas in situ analysers are sensitive for air directly sampled by the inlet. NO<sub>2</sub> is primarily emitted (or converted very fast from NO near the source) close to surface. So, if the measurements are performed in the vicinity of emission sources, we expect higher NO<sub>2</sub> from in situ measurements than MAX-DOAS, which provides a mean concentration in the 0–200 m output grid. This was also observed in previous intercomparison studies (Wang et al., 2019; Li et al., 2013; PETERS et al., 2012). To a surprising extent, we observe that until the end of 2014, most surface VMRs from MAX-DOAS are systematically higher than the in situ measurements, while afterwards, the differences become smaller. A plausible reason for the positive bias is the plumes from the Rupnagar power plant (PP1, Fig. 1),  $\sim 45$  km far from Mohali in the north-west direction, which also is the viewing direction of the MAX-DOAS instrument. Pawar et al. (2015) have previously shown back trajectories of air mass arriving at Mohali for a period of 2 years (2011–2013). Except during monsoon, more than 80 % of the back trajectories were among the clusters “westerlies”, “local”, or “calm”, all of which include the location of PP1. In monsoon, these clusters accounted for more than 50 % of the total. From the wind rose plot of Fig. F1, we also observe that in all the seasons except monsoon, the major fetch region includes PP1. The Rupnagar power plant was active with 90 % of its capacity until October 2014 and operated only with

20 % of its capacity until the ceasing of its operation in 2018 (<https://timesofindia.indiatimes.com/city/chandigarh/Punjab-shuts-10-of-14-thermal-power-plants/articleshow/44730937.cms>, last access: 19 November 2020). The power plant plume is emitted directly at an altitude ( $\sim 100$  m), much higher than the inlet height of the in situ measurements ( $\sim 15$  m). Due to their coarser vertical resolution, the MAX-DOAS surface VMRs are also influenced by the NO<sub>2</sub> at higher altitudes (e.g. from the power plant plume). During stagnant conditions, the vertical mixing is suppressed, and we expect a larger bias between the two measurements. From the MAX-DOAS NO<sub>2</sub> profiles, we can also estimate the extent of the vertical mixing of NO<sub>2</sub> in terms of the characteristic profile height ( $H_{75}$ ). Figure 12c shows the scatter plot between the MAX-DOAS and in situ surface VMRs of NO<sub>2</sub> colour-coded according to  $H_{75}$ . We observe that for profile heights of less than 200 m, the MAX-DOAS surface VMRs are more positively biased than for higher  $H_{75}$ . During the summer months (March–June), due to the radiative heating of the surface, vertical mixing is enhanced and leads to a higher  $H_{75}$  (Fig. 6). Also, the down-mixing of the power plant plume to the surface is more efficient during such conditions. Hence, during summer 2013, even though the power plant was operational at high capacity, we see a smaller bias between the two datasets. For some applications, the limited vertical resolution of MAX-DOAS instrument can be regarded as an advantage in terms of robustness against stratification in stable meteorological conditions and yield a more spatially representative value.

The horizontal heterogeneity of the NO<sub>2</sub> VMR and differences in the spatial representativeness of the measurements can also add to the observed bias in the overall measurement period. The measurements were performed within an educational institute campus, located in the south-east corner of the tri-city Panchkula, Chandigarh, and Mohali. From the high-resolution TROPOMI NO<sub>2</sub> maps for the year 2018 (Fig. 1), we can observe that the measurement location is relatively clean (with respect to the NO<sub>2</sub> VCD) compared to the surrounding regions. The viewing direction of the MAX-DOAS instrument is towards the city, and the horizontal sensitivity along the range of sight is typically a few kilometres. Thus, the MAX-DOAS measurements are sensitive for an urban air mixture consisting of higher NO<sub>2</sub> than at the measurement location. Post-2014, the bias is within 20 %, similar to those observed in previous studies, which can be attributed to these factors.

The frequency distribution of the bias (MAX-DOAS – PTR-MS) in the individual measurements of the HCHO surface VMRs shows a distribution similar to lognormal with a maximum at  $\sim 1.1$  ppb and skewed towards positive values. The large bias can also be inferred from the large offset (3.18 ppb) and slope (1.14) in the linear regression of HCHO VMRs measured by MAX-DOAS and by PTR-MS. We observe that until May 2015, there was a general agreement between the two measurements regarding their tempo-

ral variability, but the in situ VMRs were generally lower. Post-May 2015, the bias between the two measurements became larger. The reason for the larger bias is not well understood. We also observe a large variability in the MAX-DOAS HCHO VMRs, which possibly arises due to a larger uncertainty in the MAX-DOAS HCHO measurements as compared to the random uncertainty of  $\sim 30\%$  in the PTR-MS HCHO measurements. The major contribution to the error budget is from fitting errors in the DOAS fit in addition to the uncertainties in the profile inversion algorithm and cross sections. The HCHO surface VMRs retrieved using the MAX-DOAS measurements have an uncertainty of  $\sim 50\%$  (as compared to only  $\sim 20\%$  for NO<sub>2</sub> surface VMR) (Wang et al., 2017b).

Secondary photochemical production is the major source of atmospheric formaldehyde. The photo-oxidation of primarily emitted VOCs occurs in the course of their mixing in the boundary layer, and hence, a significant amount of formaldehyde is observed at altitudes of up to 600 m or even higher in some cases. The surface VMRs from MAX-DOAS shown in Fig. 13 represent the mean in the lowest 200 m layer of the MAPA output; which might also be influenced by higher altitudes due to a limited vertical resolution of MAX-DOAS. Surface VMRs from the PTR-MS measurements are sensitive to the inlet height ( $\sim 15$  m). Hence, a higher VMR from the MAX-DOAS measurement was expected. This is further supported by our observations in Fig. F8, where we observe that for the periods when the emissions of precursors of HCHO are higher (e.g. from crop residue fires in May, June, October, and November and from burning for domestic heating in December and January), the bias between the MAX-DOAS and in situ VMRs is also higher. Nevertheless, keeping in mind the systematic uncertainty of the in situ measurements (which could not be quantified within the scope of this study due to the unavailability of calibration standards) and the high uncertainty of MAX-DOAS measurements, we cannot further interpret the comparison results.

## Appendix F: Additional figures

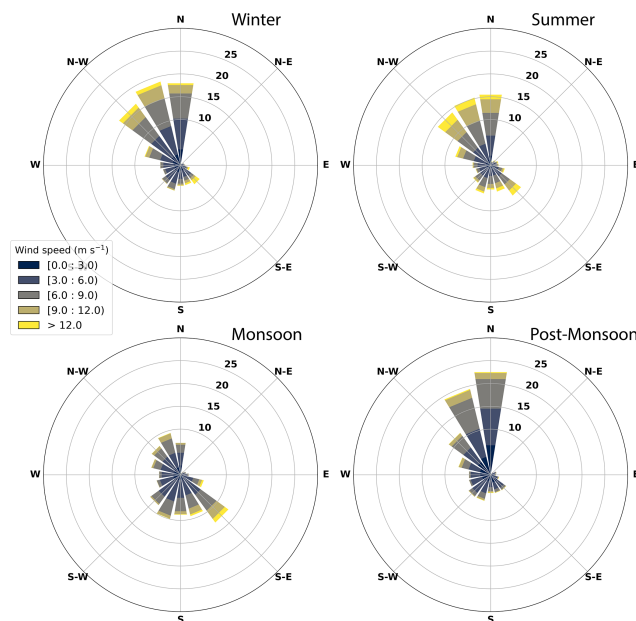


**Figure F1.** Wind rose plots showing the major fetch region of air mass arriving at Mohali for the four major seasons of the year.

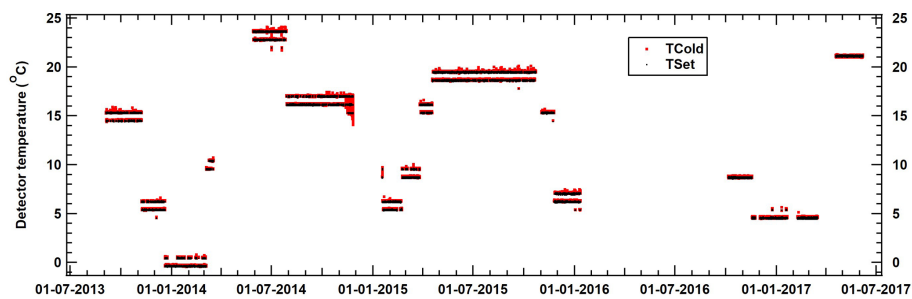


**Figure F2.** The time series of the nominal ( $T_{\text{set}}$ ) and the actual temperature ( $T_{\text{cold}}$ ) of the detector within the MAX-DOAS instrument.

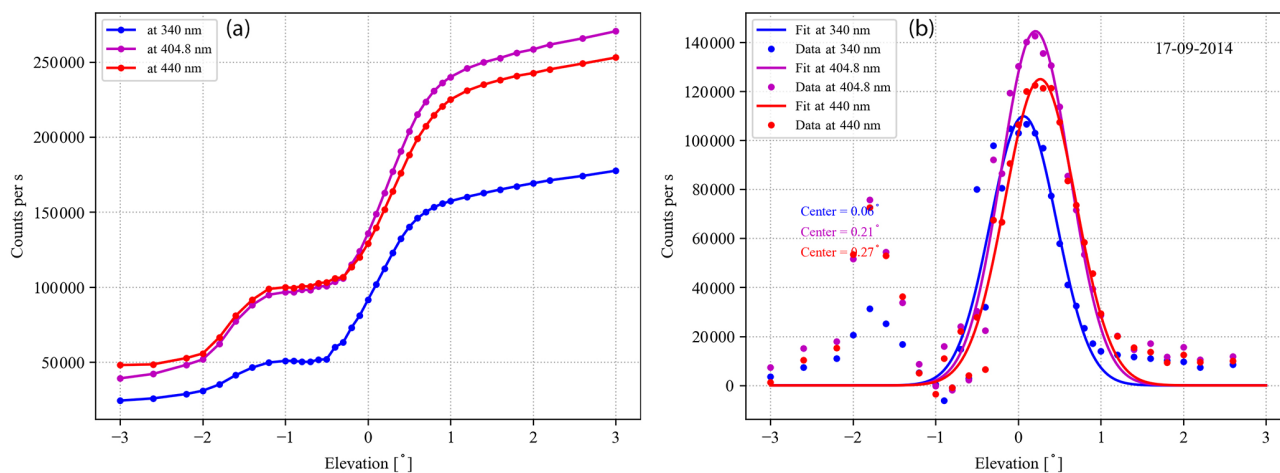


**Figure F3.** Example plots showing the measured radiance (a) and the derivative of the radiance (b) during a horizon scan spanning elevation viewing angles from  $-3$  to  $3^\circ$ . The figures correspond to the horizon scan performed on 17 September 2014.

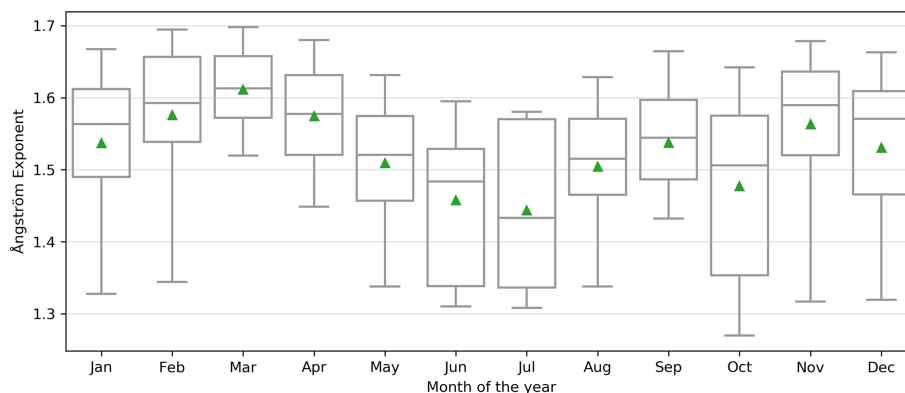


**Figure F4.** Monthly variation in Ångström exponent for the wavelength pair 470 and 550 nm derived from MODIS measurements over Mohali. The green triangles represent the monthly means. The centre line of each box represents the median values, whereas the box represents the interquartile range. The whiskers represent the 5th and 95th percentiles.

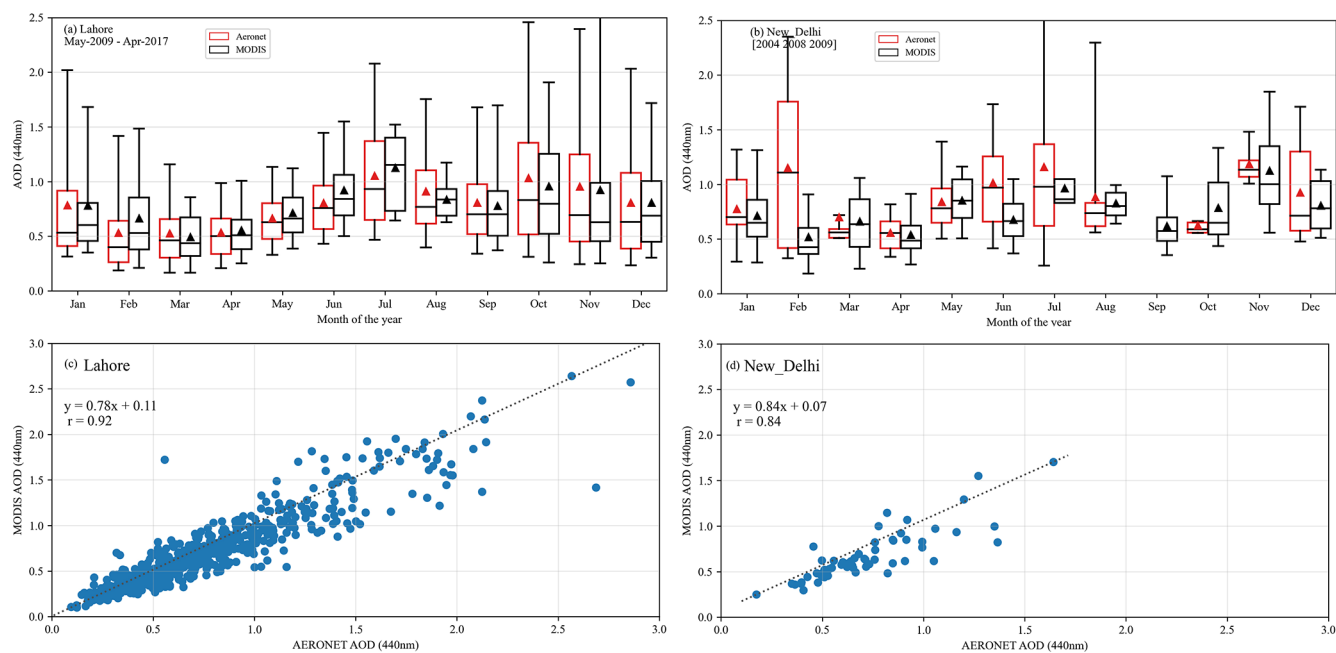


**Figure F5.** Monthly variation in the AOD (at 440 nm) as observed by AERONET sun photometers (red boxes) and MODIS (black boxes) at two sites (**a**, Lahore and **b**, New Delhi), which are the nearest stations to Mohali in the Indo-Gangetic Plain. Panels (**c**) and (**d**) show the corresponding scatter plots indicating the agreement in the daily MODIS and AERONET measurements.

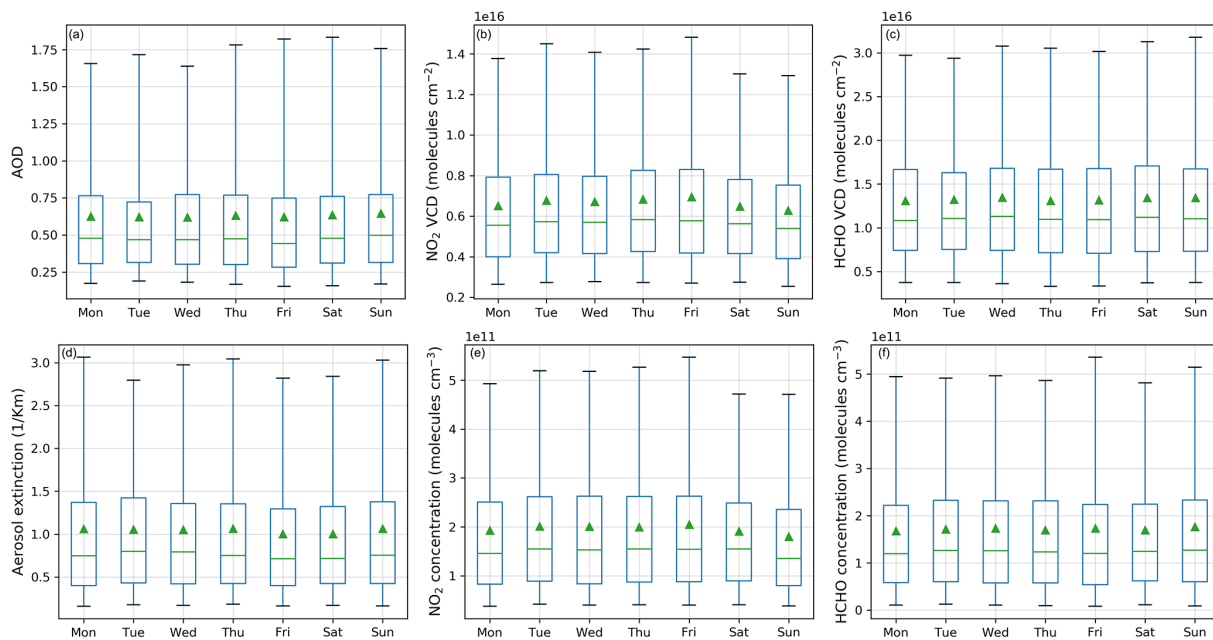


**Figure F6.** Mean weekly variation in (**a**) AOD, (**b**) NO<sub>2</sub> VCD, and (**c**) HCHO VCD. The bottom row shows the mean weekly variation in (**d**) aerosol extinction, (**e**) NO<sub>2</sub> concentration, and (**f**) HCHO concentration in the bottom-most layer (0–200 m) retrieved from the profile inversion of the MAX-DOAS measurements.

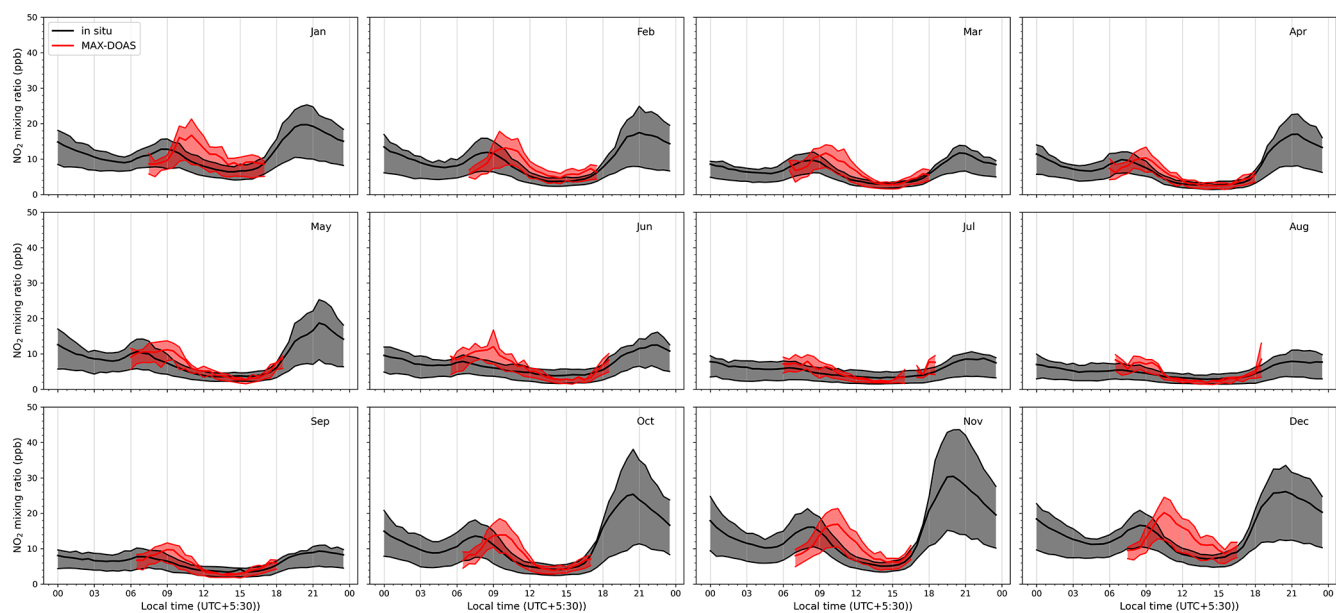


**Figure F7.** Mean diurnal profiles of surface NO<sub>2</sub> mixing ratios measured by an in situ analyser (black) and retrieved from the MAX-DOAS measurements (red) for different months of the year. The dark line represents the mean value, while the shaded region above and below the dark lines represent the 75th and 25th percentiles, respectively.

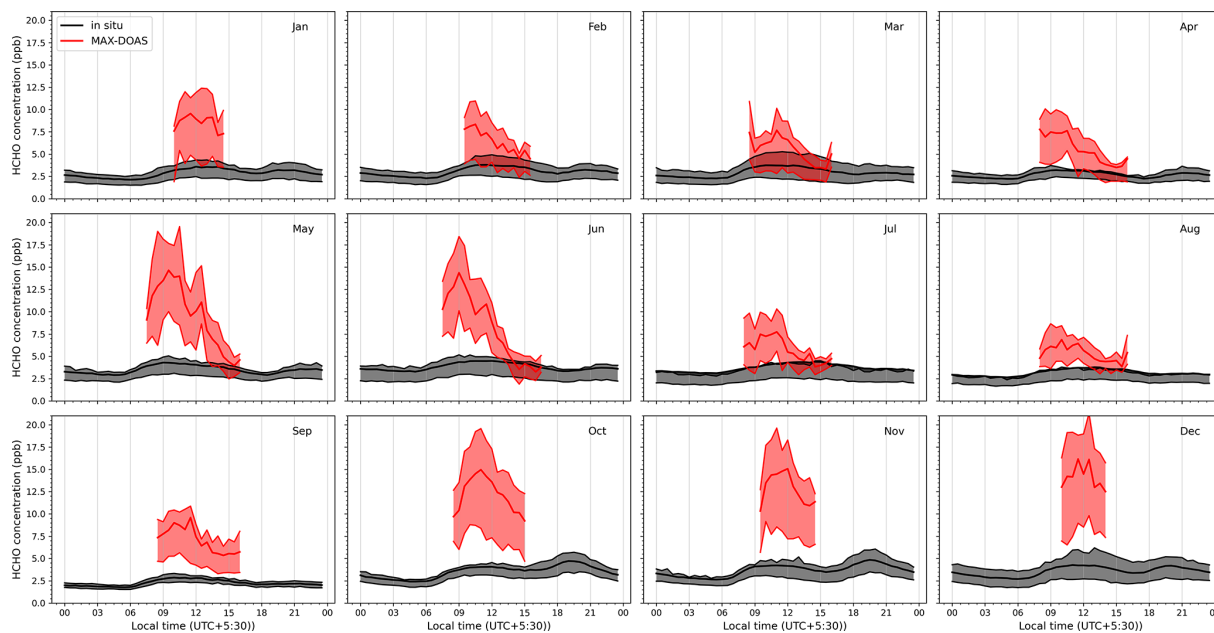


**Figure F8.** Mean diurnal profiles of surface HCHO mixing ratios measured by the PTR-MS (black) and retrieved from the MAX-DOAS measurements (red) for different months of the year. The dark line represents the mean value, while the shaded region above and below the dark lines represent the 75th and 25th percentiles, respectively.

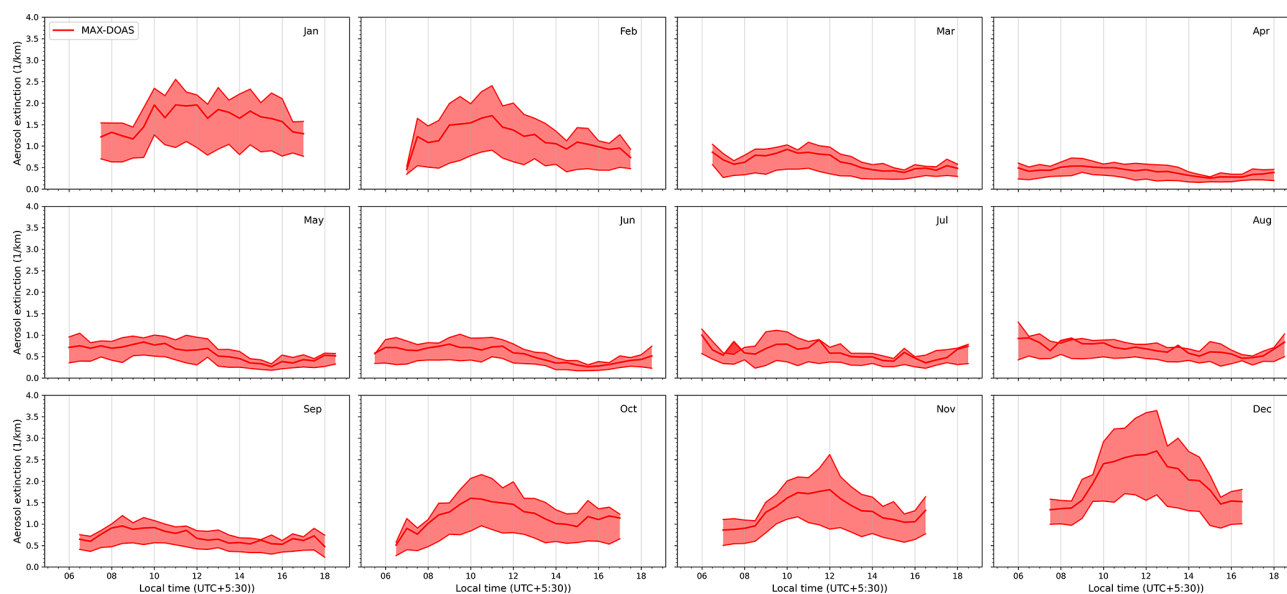


**Figure F9.** Mean diurnal profiles of the aerosol extinction in the bottom-most layer (0–200 m) retrieved from the MAX-DOAS measurements for different months of the year. The dark line represents the mean value, while the shaded region above and below the dark lines represent the 75th and 25th percentiles, respectively.

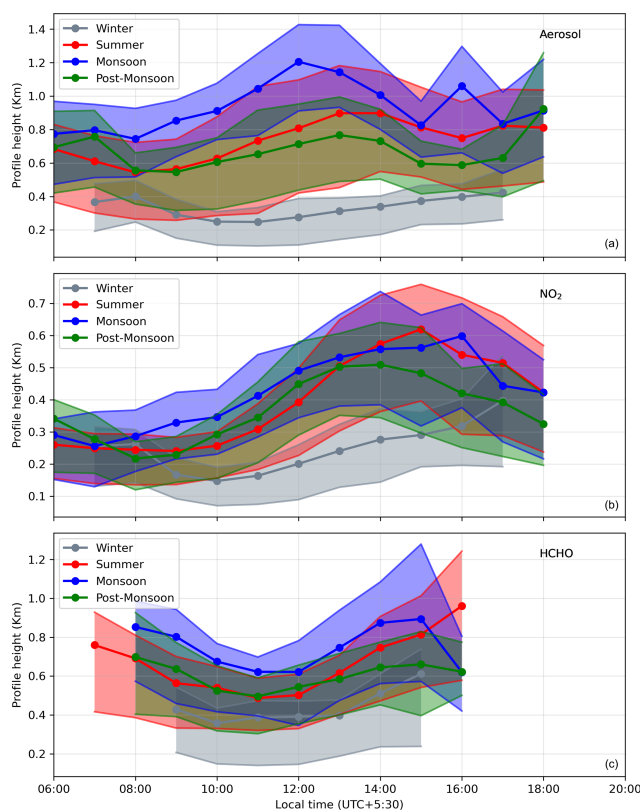


**Figure F10.** Diurnal variation in characteristic profile heights of aerosol (a), NO<sub>2</sub> (b), and HCHO (c) for the four major seasons.

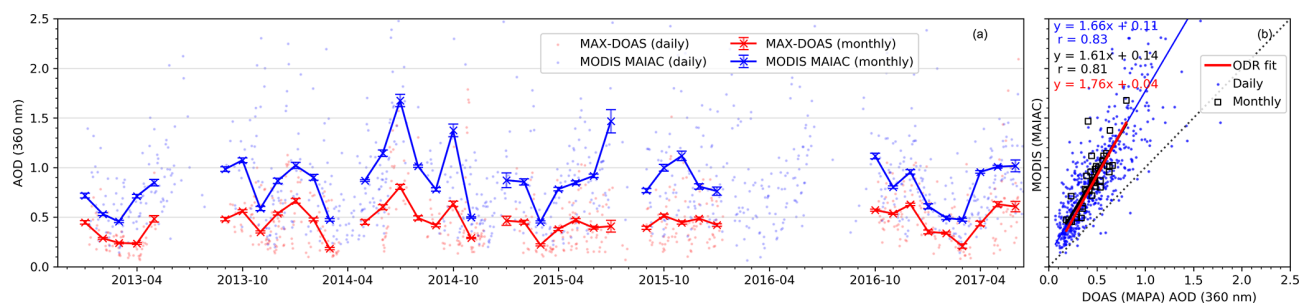


**Figure F11.** Intercomparison of daily (dots) and monthly mean (lines and markers) AOD at 360 nm retrieved from ground-based MAX-DOAS O<sub>4</sub> measurements and from the MODIS MAIAC data product when no scaling factors were applied for the O<sub>4</sub> dSCDs.

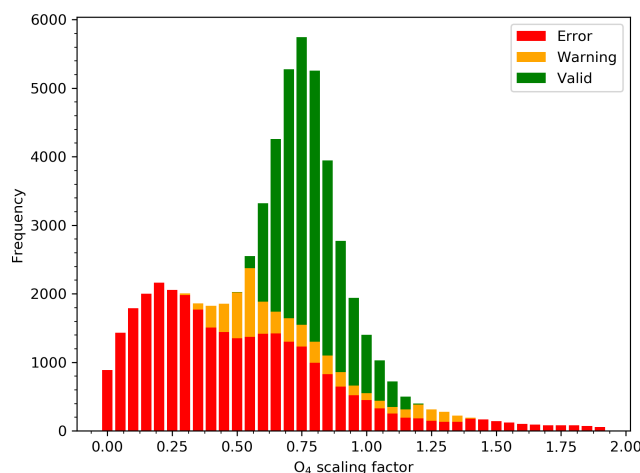


**Figure F12.** Frequency distribution of O<sub>4</sub> scaling factors derived from profile inversions, which allowed us to vary the O<sub>4</sub> scaling factors in order to achieve an agreement between measurements and forward model. The green bars show retrievals which are flagged as valid, while the orange and red bars indicate retrievals with warning and error flags.

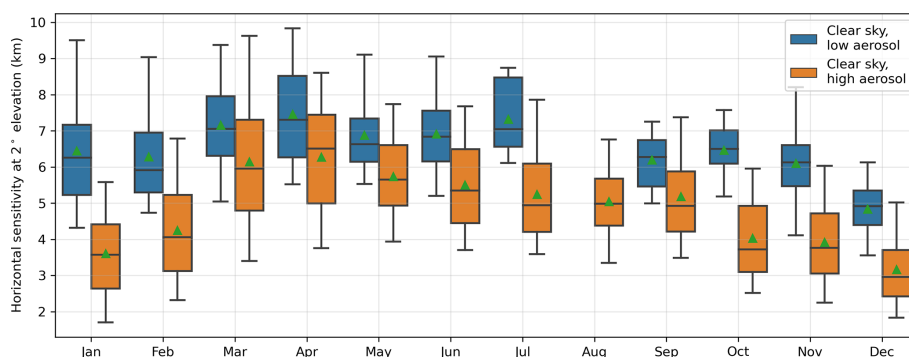


**Figure F13.** Box-and-whiskers plot showing the horizontal sensitivity distance of MAX-DOAS measurements during afternoon hours (between 12:00 and 15:00 LT) for 2° elevation angle. The blue boxes represent clear-sky conditions with low aerosol load, and the orange boxes indicate clear-sky conditions with high aerosol load.

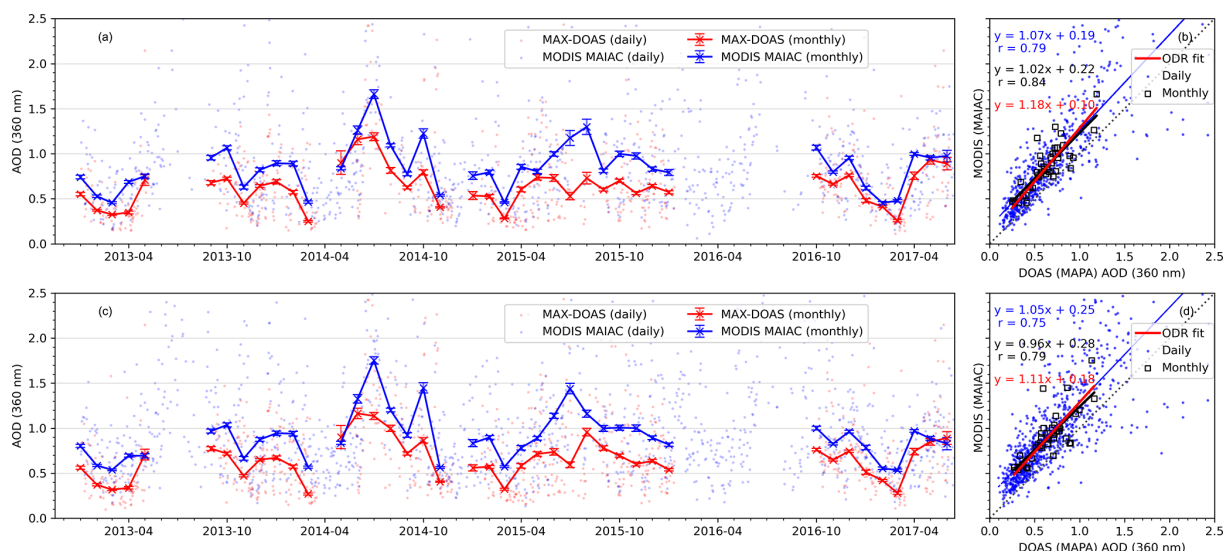


**Figure F14.** Intercomparison of daily (dots) and monthly mean (lines and markers) AOD at 360 nm retrieved from ground-based MAX-DOAS O<sub>4</sub> measurements and from the MODIS MAIAC data product when spatially averaged over 5 km (a, b) and 25 km (c, d) around Mohali. O<sub>4</sub> dSCD were scaled by a factor of 0.8, as discussed in the main text.

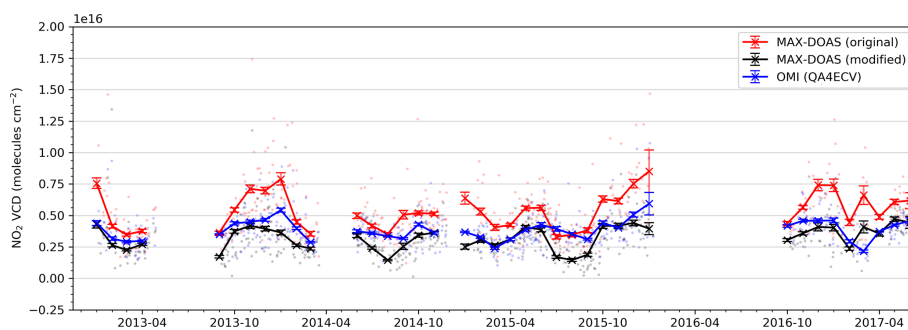


**Figure F15.** Time series of daily (dots) and monthly means (lines and markers) of MAX-DOAS NO<sub>2</sub> VCDs, OMI QA4ECV NO<sub>2</sub> VCDs, and MAX-DOAS VCDs modified using the QA4ECV averaging kernels and the TM4 a priori profiles.

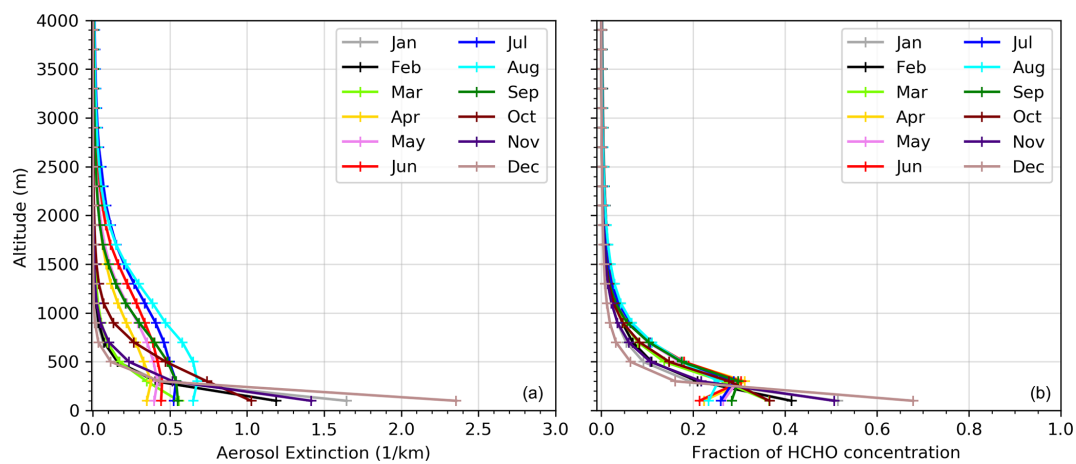


**Figure F16.** Monthly mean aerosol extinction profiles (a) retrieved from MAX-DOAS O<sub>4</sub> measurement and HCHO profiles (b) over Mohali at around the OMI overpass time (12:30–14:30 LT).

**Data availability.** The MODIS MAIAC (Lyapustin et al., 2018), OMI OMAERUV (Torres et al., 2007), OMNO2 (Marchenko et al., 2015), and OMHCHO (González Abad et al., 2015) data can be downloaded from the LAADS website (<https://ladsweb.modaps.eosdis.nasa.gov/>, last access: 19 November 2020). The OMI DOMINO (Boersma et al., 2011) and QA4ECV (Boersma et al., 2018; De Smedt et al., 2018) data are available at <http://www.temis.nl> (last access: 19 November 2020). The MAX-DOAS measurement data, spectral analysis, and profile inversion results can be obtained from the corresponding author. The in situ measurement data can be obtained from IISER Mohali atmospheric chemistry facility by contacting Vinayak Sinha ([vsinha@iisermohali.ac.in](mailto:vsinha@iisermohali.ac.in)).

**Author contributions.** VK and TW prepared the paper with contributions from all co-authors. VK, StD, AKM, and SeD operated the MAX-DOAS instrument, and VK performed spectral analyses and profile inversion with help from SB, StD, SeD, and TW. YW helped VK with cloud classification. VK, AKM, and VS operated the in situ analysers and contributed to the analyses. All co-authors contributed to modifications and discussions in preparing the paper.

**Competing interests.** Thomas Wagner is a member of the editorial board of the journal.

**Acknowledgements.** We acknowledge the IISER Mohali atmospheric chemistry facility for the support with logistics related to the operation of the MAX-DOAS instrument and the sharing of meteorological and in situ measurement data. Vinod Kumar acknowledges the Alexander von Humboldt Foundation and Max Planck Society for a supporting postdoctoral stipend. Abhishek Kumar Mishra acknowledges MHRD, India, for support regarding a PhD fellowship. Vinayak Sinha thanks the Max Planck Society and Max Planck Institute for Chemistry and the Department of Science and Technology, India, for funding a Max Planck India partner group at IISER Mohali through which this long-term collaboration could be accomplished. We acknowledge the free use of DOMINO NO<sub>2</sub> and QA4ECV NO<sub>2</sub> and HCHO level 2 data products from OMI from <http://www.temis.nl> (last access: 17 November 2020). We thank the Level-1 and Atmosphere Archive & Distribution System (LAADS) Distributed Active Archive Center (DAAC) for providing free access to the OMAERUV, OMNO2, OMHCHO, and MAIAC data products. We thank Philippe Goloub and Brent N. Holben for establishing and maintaining the AERONET sites New Delhi and Lahore, respectively, whose data have been used in this study. We thank the two anonymous reviewers for their constructive feedback to the paper.

**Financial support.** The article processing charges for this open-access publication were covered by the Max Planck Society.

**Review statement.** This paper was edited by Yugo Kanaya and reviewed by two anonymous referees.

## References

- Altaratz, O., Bar-Or, R. Z., Wollner, U., and Koren, I.: Relative humidity and its effect on aerosol optical depth in the vicinity of convective clouds, *Environ. Res. Lett.*, 8, 034025, <https://doi.org/10.1088/1748-9326/8/3/034025>, 2013.
- Beig, G., Gunthe, S., and Jadhav, D. B.: Simultaneous measurements of ozone and its precursors on a diurnal scale at a semi urban site in India, *J. Atmos. Chem.*, 57, 239–253, <https://doi.org/10.1007/s10874-007-9068-8>, 2007.
- Beirle, S., Folkert, B. K., Platt, U., Lawrence, M. G., and Wagner, T.: Megacity Emissions and Lifetimes of Nitrogen Oxides Probed from space, *Science*, 333, 1737–1739, <https://doi.org/10.1126/science.1207824>, 2011.
- Beirle, S., Dörner, S., Donner, S., Remmers, J., Wang, Y., and Wagner, T.: The Mainz profile algorithm (MAPA), *Atmos. Meas. Tech.*, 12, 1785–1806, <https://doi.org/10.5194/amt-12-1785-2019>, 2019.
- Biswas, M. S., Ghude, S. D., Gurnale, D., Prabhakaran, T., and Mahajan, A. S.: Simultaneous Observations of Nitrogen Dioxide, Formaldehyde and Ozone in the Indo-Gangetic Plain, *Aerosol Air Qual. Res.*, 19, 1749–1764, <https://doi.org/10.4209/aaqr.2018.12.0484>, 2019.
- Boersma, K. F., Eskes, H. J., Dirksen, R. J., van der A, R. J., Veefkind, J. P., Stammes, P., Huijnen, V., Kleipool, Q. L., Sneep, M., Claas, J., Leitão, J., Richter, A., Zhou, Y., and Brunner, D.: An improved tropospheric NO<sub>2</sub> column retrieval algorithm for the Ozone Monitoring Instrument, *Atmos. Meas. Tech.*, 4, 1905–1928, <https://doi.org/10.5194/amt-4-1905-2011>, 2011 (data available at: <http://www.temis.nl>, last access: 19 November 2020).
- Boersma, K. F., Eskes, H. J., Richter, A., De Smedt, I., Lorente, A., Beirle, S., van Geffen, J. H. G. M., Zara, M., Peters, E., Van Roozendaal, M., Wagner, T., Maasackers, J. D., van der A, R. J., Nightingale, J., De Rudder, A., Irie, H., Pinardi, G., Lambert, J.-C., and Compernelle, S. C.: Improving algorithms and uncertainty estimates for satellite NO<sub>2</sub> retrievals: results from the quality assurance for the essential climate variables (QA4ECV) project, *Atmos. Meas. Tech.*, 11, 6651–6678, <https://doi.org/10.5194/amt-11-6651-2018>, 2018 (data available at: <http://www.temis.nl>, last access: 19 November 2020).
- Bösch, T.: Detailed analysis of MAX-DOAS measurements in Bremen : spatial and temporal distribution of aerosols, formaldehyde and nitrogen dioxide, PhD thesis, Universität Bremen, Germany, 2018.
- Brinksmas, E. J., Pinardi, G., Volten, H., Braak, R., Richter, A., Schönhardt, A., van Roozendaal, M., Fayt, C., Hermans, C., Dirksen, R. J., Vlemmix, T., Berkhout, A. J. C., Swart, D. P. J., Oetjen, H., Wittrock, F., Wagner, T., Ibrahim, O. W., de Leeuw, G., Moerman, M., Curier, R. L., Celarier, E. A., Cede, A., Knap, W. H., Veefkind, J. P., Eskes, H. J., Allaart, M., Rothe, R., Peters, A. J. M., and Levelt, P. F.: The 2005 and 2006 DANDELIONS NO<sub>2</sub> and aerosol intercomparison campaigns, *J. Geophys. Res.-Atmos.*, 113, D16S46, <https://doi.org/10.1029/2007jd008808>, 2008.
- Chaliyakunnel, S., Millet, D. B., and Chen, X.: Constraining emissions of volatile organic compounds over the Indian subcontinent using space-based formaldehyde measurements, *J. Geophys. Res.-Atmos.*, 124, 10525–10545, <https://doi.org/10.1029/2019jd031262>, 2019.

- Chan, K. L., Wang, Z., Ding, A., Heue, K.-P., Shen, Y., Wang, J., Zhang, F., Shi, Y., Hao, N., and Wenig, M.: MAX-DOAS measurements of tropospheric NO<sub>2</sub> and HCHO in Nanjing and a comparison to ozone monitoring instrument observations, *Atmos. Chem. Phys.*, 19, 10051–10071, <https://doi.org/10.5194/acp-19-10051-2019>, 2019.
- Chandra, B. P. and Sinha, V.: Contribution of post-harvest agricultural paddy residue fires in the N.W. Indo-Gangetic Plain to ambient carcinogenic benzenoids, toxic isocyanic acid and carbon monoxide, *Environ. Int.*, 88, 187–197, <https://doi.org/10.1016/j.envint.2015.12.025>, 2016.
- Cui, L., Zhang, Z., Huang, Y., Lee, S. C., Blake, D. R., Ho, K. F., Wang, B., Gao, Y., Wang, X. M., and Louie, P. K. K.: Measuring OVOCs and VOCs by PTR-MS in an urban roadside microenvironment of Hong Kong: relative humidity and temperature dependence, and field intercomparisons, *Atmos. Meas. Tech.*, 9, 5763–5779, <https://doi.org/10.5194/amt-9-5763-2016>, 2016.
- Danckaert, T., Fayt, C., Van Roozendael, M., De Smedt, I., Letocart, V., Merlaud, A., and Pinardi, G.: QDOAS Software user manual, Belgian Institute for Space Aeronomy, Brussels, Belgium, 2012.
- Debaje, S. B. and Kakade, A. D.: Surface ozone variability over western Maharashtra, India, *J. Hazard. Mater.*, 161, 686–700, <https://doi.org/10.1016/j.jhazmat.2008.04.010>, 2009.
- de Foy, B., Lu, Z., and Streets, D. G.: Satellite NO<sub>2</sub> retrievals suggest China has exceeded its NO<sub>x</sub> reduction goals from the twelfth Five-Year Plan, *Sci. Rep.*, 6, 35912, <https://doi.org/10.1038/srep35912>, 2016.
- de Gouw, J. and Warneke, C.: Measurements of volatile organic compounds in the earth's atmosphere using proton-transfer-reaction mass spectrometry, *Mass Spectrom. Rev.*, 26, 223–257, <https://doi.org/10.1002/mas.20119>, 2007.
- De Smedt, I., Stavrou, T., Hendrick, F., Danckaert, T., Vlemmix, T., Pinardi, G., Theys, N., Lerot, C., Gielen, C., Vigouroux, C., Hermans, C., Fayt, C., Veefkind, P., Müller, J.-F., and Van Roozendael, M.: Diurnal, seasonal and long-term variations of global formaldehyde columns inferred from combined OMI and GOME-2 observations, *Atmos. Chem. Phys.*, 15, 12519–12545, <https://doi.org/10.5194/acp-15-12519-2015>, 2015.
- De Smedt, I., Theys, N., Yu, H., Danckaert, T., Lerot, C., Compernelle, S., Van Roozendael, M., Richter, A., Hilboll, A., Peters, E., Pedergnana, M., Loyola, D., Beirle, S., Wagner, T., Eskes, H., van Geffen, J., Boersma, K. F., and Veefkind, P.: Algorithm theoretical baseline for formaldehyde retrievals from S5P TROPOMI and from the QA4ECV project, *Atmos. Meas. Tech.*, 11, 2395–2426, <https://doi.org/10.5194/amt-11-2395-2018>, 2018 (data available at: <http://www.temis.nl>, last access: 19 November 2020).
- Deutschmann, T., Beirle, S., Frieß, U., Grzegorski, M., Kern, C., Kritten, L., Platt, U., Prados-Román, C., Pukite, J., Wagner, T., Werner, B., and Pfeilsticker, K.: The Monte Carlo atmospheric radiative transfer model McArtim: Introduction and validation of Jacobians and 3D features, *Journal of Quantitative Spectroscopy and Radiative Transfer*, 112, 1119–1137, <https://doi.org/10.1016/j.jqsrt.2010.12.009>, 2011.
- Donner, S., Kuhn, J., Van Roozendael, M., Bais, A., Beirle, S., Bösch, T., Bogner, K., Bruchkouski, I., Chan, K. L., Dörner, S., Drosoglou, T., Fayt, C., Frieß, U., Hendrick, F., Hermans, C., Jin, J., Li, A., Ma, J., Peters, E., Pinardi, G., Richter, A., Schreier, S. F., Seyler, A., Strong, K., Tirpitz, J.-L., Wang, Y., Xie, P., Xu, J., Zhao, X., and Wagner, T.: Evaluating different methods for elevation calibration of MAX-DOAS (Multi AXis Differential Optical Absorption Spectroscopy) instruments during the CINDI-2 campaign, *Atmos. Meas. Tech.*, 13, 685–712, <https://doi.org/10.5194/amt-13-685-2020>, 2020.
- Drosoglou, T., Bais, A. F., Zyrichidou, I., Kouremeti, N., Poupkou, A., Liora, N., Giannaros, C., Koukouli, M. E., Balis, D., and Melas, D.: Comparisons of ground-based tropospheric NO<sub>2</sub> MAX-DOAS measurements to satellite observations with the aid of an air quality model over the Thessaloniki area, Greece, *Atmos. Chem. Phys.*, 17, 5829–5849, <https://doi.org/10.5194/acp-17-5829-2017>, 2017.
- Dutta, C., Chatterjee, A., Jana, T. K., Mukherjee, A. K., and Sen, S.: Contribution from the primary and secondary sources to the atmospheric formaldehyde in Kolkata, India, *Sci. Total Environ.*, 408, 4744–4748, <https://doi.org/10.1016/j.scitotenv.2010.01.031>, 2010.
- Eskes, H. J. and Boersma, K. F.: Averaging kernels for DOAS total-column satellite retrievals, *Atmos. Chem. Phys.*, 3, 1285–1291, <https://doi.org/10.5194/acp-3-1285-2003>, 2003.
- Fadnavis, S., Semeniuk, K., Schultz, M. G., Kiefer, M., Mahajan, A., Pozzoli, L., and Sonbawane, S.: Transport pathways of peroxyacetyl nitrate in the upper troposphere and lower stratosphere from different monsoon systems during the summer monsoon season, *Atmos. Chem. Phys.*, 15, 11477–11499, <https://doi.org/10.5194/acp-15-11477-2015>, 2015.
- Fishman, J., Bowman, K. W., Burrows, J. P., Richter, A., Chance, K. V., Edwards, D. P., Martin, R. V., Morris, G. A., Pierce, R. B., Ziemke, J. R., Al-Saadi, J. A., Creilson, J. K., Schaack, T. K., and Thompson, A. M.: Remote Sensing of Tropospheric Pollution from Space, *B. Am. Meteorol. Soc.*, 89, 805–822, <https://doi.org/10.1175/2008bams2526.1>, 2008.
- Fleischmann, O. C., Hartmann, M., Burrows, J. P., and Orphal, J.: New ultraviolet absorption cross-sections of BrO at atmospheric temperatures measured by time-windowing Fourier transform spectroscopy, *J. Photoch. Photobio. A*, 168, 117–132, <https://doi.org/10.1016/j.jphotochem.2004.03.026>, 2004.
- Fortems-Cheiney, A., Chevallier, F., Pison, I., Bousquet, P., Saunio, M., Szopa, S., Cressot, C., Kurosu, T. P., Chance, K., and Fried, A.: The formaldehyde budget as seen by a global-scale multi-constraint and multi-species inversion system, *Atmos. Chem. Phys.*, 12, 6699–6721, <https://doi.org/10.5194/acp-12-6699-2012>, 2012.
- Franco, B., Hendrick, F., Van Roozendael, M., Müller, J.-F., Stavrou, T., Marais, E. A., Bovy, B., Bader, W., Fayt, C., Hermans, C., Lejeune, B., Pinardi, G., Servais, C., and Mahieu, E.: Retrievals of formaldehyde from ground-based FTIR and MAX-DOAS observations at the Jungfraujoch station and comparisons with GEOS-Chem and IMAGES model simulations, *Atmos. Meas. Tech.*, 8, 1733–1756, <https://doi.org/10.5194/amt-8-1733-2015>, 2015.
- Fu, T.-M., Jacob, D. J., Palmer, P. I., Chance, K., Wang, Y. X., Barletta, B., Blake, D. R., Stanton, J. C., and Pilling, M. J.: Space-based formaldehyde measurements as constraints on volatile organic compound emissions in east and south Asia and implications for ozone, *J. Geophys. Res.-Atmos.*, 112, D06312, <https://doi.org/10.1029/2006JD007853>, 2007.
- Fukushima, A., Kanamori, H., and Matsumoto, J.: Regionality of long-term trends and interannual variation of seasonal precipita-

- tion over India, *Progress in Earth and Planetary Science*, 6, 20, <https://doi.org/10.1186/s40645-019-0255-4>, 2019.
- Gaur, A., Tripathi, S. N., Kanawade, V. P., Tare, V., and Shukla, S. P.: Four-year measurements of trace gases (SO<sub>2</sub>, NO<sub>x</sub>, CO, and O<sub>3</sub>) at an urban location, Kanpur, in Northern India, *J. Atmos. Chem.*, 71, 283–301, <https://doi.org/10.1007/s10874-014-9295-8>, 2014.
- Ghude, S. D., Fadnavis, S., Beig, G., Polade, S. D., and van der A, R. J.: Detection of surface emission hot spots, trends, and seasonal cycle from satellite-retrieved NO<sub>2</sub> over India, *J. Geophys. Res.-Atmos.*, 113, D20305, <https://doi.org/10.1029/2007jd009615>, 2008.
- Ghude, S. D., Kulkarni, S. H., Jena, C., Pfister, G. G., Beig, G., Fadnavis, S., and van der A, R. J.: Application of satellite observations for identifying regions of dominant sources of nitrogen oxides over the Indian Subcontinent, *J. Geophys. Res.-Atmos.*, 118, 1075–1089, <https://doi.org/10.1029/2012jd017811>, 2013.
- Giles, J.: Hikes in surface ozone could suffocate crops, *Nature*, 435, 7, <https://doi.org/10.1038/435007a>, 2005.
- González Abad, G., Liu, X., Chance, K., Wang, H., Kurosu, T. P., and Suleiman, R.: Updated Smithsonian Astrophysical Observatory Ozone Monitoring Instrument (SAO OMI) formaldehyde retrieval, *Atmos. Meas. Tech.*, 8, 19–32, <https://doi.org/10.5194/amt-8-19-2015>, 2015 (data available at: <https://ladsweb.modaps.eosdis.nasa.gov/>, last access: 19 November 2020).
- Gonzalez Abad, G., Souri, A. H., Bak, J., Chance, K., Flynn, L. E., Krotkov, N. A., Lamsal, L., Li, C., Liu, X., Miller, C. C., Nowlan, C. R., Suleiman, R., and Wang, H.: Five decades observing Earth's atmospheric trace gases using ultraviolet and visible backscatter solar radiation from space, *J. Quant. Spectrosc. Ra.*, 238, 106478, <https://doi.org/10.1016/j.jqsrt.2019.04.030>, 2019.
- Guenther, A. B., Monson, R. K., and Fall, R.: Isoprene and monoterpene emission rate variability: Observations with eucalyptus and emission rate algorithm development, *J. Geophys. Res.-Atmos.*, 96, 10799–10808, <https://doi.org/10.1029/91JD00960>, 1991.
- Halla, J. D., Wagner, T., Beirle, S., Brook, J. R., Hayden, K. L., O'Brien, J. M., Ng, A., Majonis, D., Wenig, M. O., and McLaren, R.: Determination of tropospheric vertical columns of NO<sub>2</sub> and aerosol optical properties in a rural setting using MAX-DOAS, *Atmos. Chem. Phys.*, 11, 12475–12498, <https://doi.org/10.5194/acp-11-12475-2011>, 2011.
- Heckel, A., Richter, A., Tarsu, T., Wittrock, F., Hak, C., Pundt, I., Junkermann, W., and Burrows, J. P.: MAX-DOAS measurements of formaldehyde in the Po-Valley, *Atmos. Chem. Phys.*, 5, 909–918, <https://doi.org/10.5194/acp-5-909-2005>, 2005.
- Hilboll, A., Richter, A., and Burrows, J. P.: Long-term changes of tropospheric NO<sub>2</sub> over megacities derived from multiple satellite instruments, *Atmos. Chem. Phys.*, 13, 4145–4169, <https://doi.org/10.5194/acp-13-4145-2013>, 2013.
- Hönninger, G., von Friedeburg, C., and Platt, U.: Multi axis differential optical absorption spectroscopy (MAX-DOAS), *Atmos. Chem. Phys.*, 4, 231–254, <https://doi.org/10.5194/acp-4-231-2004>, 2004.
- Hoque, H. M. S., Irie, H., Damiani, A., Rawat, P., and Naja, M.: First simultaneous observations of formaldehyde and glyoxal by MAX-DOAS in the Indo-Gangetic Plain region, *SOLA*, 14, 159–164, <https://doi.org/10.2151/sola.2018-028>, 2018.
- Huijnen, V., Eskes, H. J., Poupkou, A., Elbern, H., Boersma, K. F., Foret, G., Sofiev, M., Valdebenito, A., Flemming, J., Stein, O., Gross, A., Robertson, L., D'Isidoro, M., Kioutsioukis, I., Friese, E., Amstrup, B., Bergstrom, R., Strunk, A., Vira, J., Zyryanov, D., Maurizi, A., Melas, D., Peuch, V.-H., and Zerefos, C.: Comparison of OMI NO<sub>2</sub> tropospheric columns with an ensemble of global and European regional air quality models, *Atmos. Chem. Phys.*, 10, 3273–3296, <https://doi.org/10.5194/acp-10-3273-2010>, 2010.
- Irie, H., Kanaya, Y., Akimoto, H., Tanimoto, H., Wang, Z., Gleason, J. F., and Bucsela, E. J.: Validation of OMI tropospheric NO<sub>2</sub> column data using MAX-DOAS measurements deep inside the North China Plain in June 2006: Mount Tai Experiment 2006, *Atmos. Chem. Phys.*, 8, 6577–6586, <https://doi.org/10.5194/acp-8-6577-2008>, 2008.
- Jin, J., Ma, J., Lin, W., Zhao, H., Shaiganfar, R., Beirle, S., and Wagner, T.: MAX-DOAS measurements and satellite validation of tropospheric NO<sub>2</sub> and SO<sub>2</sub> vertical column densities at a rural site of North China, *Atmos. Environ.*, 133, 12–25, <https://doi.org/10.1016/j.atmosenv.2016.03.031>, 2016.
- Kaiser, J., Jacob, D. J., Zhu, L., Travis, K. R., Fisher, J. A., González Abad, G., Zhang, L., Zhang, X., Fried, A., Crouse, J. D., St. Clair, J. M., and Wisthaler, A.: High-resolution inversion of OMI formaldehyde columns to quantify isoprene emission on ecosystem-relevant scales: application to the southeast US, *Atmos. Chem. Phys.*, 18, 5483–5497, <https://doi.org/10.5194/acp-18-5483-2018>, 2018.
- Kramer, L. J., Leigh, R. J., Remedios, J. J., and Monks, P. S.: Comparison of OMI and ground-based in situ and MAX-DOAS measurements of tropospheric nitrogen dioxide in an urban area, *J. Geophys. Res.-Atmos.*, 113, D16S39, <https://doi.org/10.1029/2007jd009168>, 2008.
- Kumar, V. and Sinha, V.: VOC–OHM: A new technique for rapid measurements of ambient total OH reactivity and volatile organic compounds using a single proton transfer reaction mass spectrometer, *Int. J. Mass Spectrom.*, 374, 55–63, <https://doi.org/10.1016/j.ijms.2014.10.012>, 2014.
- Kumar, V., Sarkar, C., and Sinha, V.: Influence of post-harvest crop residue fires on surface ozone mixing ratios in the N.W. IGP analyzed using 2 years of continuous in situ trace gas measurements, *J. Geophys. Res.*, 121, 3619–3633, <https://doi.org/10.1002/2015JD024308>, 2016.
- Kumar, V., Chandra, B. P., and Sinha, V.: Large unexplained suite of chemically reactive compounds present in ambient air due to biomass fires, *Sci. Rep.*, 8, 626, <https://doi.org/10.1038/s41598-017-19139-3>, 2018.
- Kunhikrishnan, T., Lawrence, M. G., von Kuhlmann, R., Wenig, M. O., Asman, W. A. H., Richter, A., and Burrows, J. P.: Regional NO<sub>x</sub> emission strength for the Indian subcontinent and the impact of emissions from India and neighboring countries on regional O<sub>3</sub> chemistry, *J. Geophys. Res.-Atmos.*, 111, D15301, <https://doi.org/10.1029/2005jd006036>, 2006.
- Lawrence, M. G. and Lelieveld, J.: Atmospheric pollutant outflow from southern Asia: a review, *Atmos. Chem. Phys.*, 10, 11017–11096, <https://doi.org/10.5194/acp-10-11017-2010>, 2010.
- Levelt, P. F., van den Oord, G. H. J., Dobber, M. R., Malkki, A., Visser, H., de Vries, J., Stammes, P., Lundell, J. O. V., and Saari, H.: The ozone monitoring instrument, *IEEE T. Geosci. Remote*,

- 44, 1093–1101, <https://doi.org/10.1109/TGRS.2006.872333>, 2006.
- Levy, R. C., Mattoo, S., Munchak, L. A., Remer, L. A., Sayer, A. M., Patadia, F., and Hsu, N. C.: The Collection 6 MODIS aerosol products over land and ocean, *Atmos. Meas. Tech.*, 6, 2989–3034, <https://doi.org/10.5194/amt-6-2989-2013>, 2013.
- Li, C., McLinden, C., Fioletov, V., Krotkov, N., Carn, S., Joiner, J., Streets, D., He, H., Ren, X., Li, Z., and Dickerson, R. R.: India Is Overtaking China as the World's Largest Emitter of Anthropogenic Sulfur Dioxide, *Sci. Rep.*, 7, 14304, <https://doi.org/10.1038/s41598-017-14639-8>, 2017.
- Li, X., Brauers, T., Hofzumahaus, A., Lu, K., Li, Y. P., Shao, M., Wagner, T., and Wahner, A.: MAX-DOAS measurements of NO<sub>2</sub>, HCHO and CHOCHO at a rural site in Southern China, *Atmos. Chem. Phys.*, 13, 2133–2151, <https://doi.org/10.5194/acp-13-2133-2013>, 2013.
- Lindinger, W., Hansel, A., and Jordan, A.: On-line monitoring of volatile organic compounds at pptv levels by means of proton-transfer-reaction mass spectrometry (PTR-MS) medical applications, food control and environmental research, *Int. J. Mass Spectrom.*, 173, 191–241, [https://doi.org/10.1016/s0168-1176\(97\)00281-4](https://doi.org/10.1016/s0168-1176(97)00281-4), 1998.
- Lyapustin, A., Wang, Y., Korkin, S., and Huang, D.: MODIS Collection 6 MAIAC algorithm, *Atmos. Meas. Tech.*, 11, 5741–5765, <https://doi.org/10.5194/amt-11-5741-2018>, 2018 (data available at: <https://ladsweb.modaps.eosdis.nasa.gov/>, last access: 19 November 2020).
- Ma, J. Z., Beirle, S., Jin, J. L., Shaiganfar, R., Yan, P., and Wagner, T.: Tropospheric NO<sub>2</sub> vertical column densities over Beijing: results of the first three years of ground-based MAX-DOAS measurements (2008–2011) and satellite validation, *Atmos. Chem. Phys.*, 13, 1547–1567, <https://doi.org/10.5194/acp-13-1547-2013>, 2013.
- MacDonald, S. M., Oetjen, H., Mahajan, A. S., Whalley, L. K., Edwards, P. M., Heard, D. E., Jones, C. E., and Plane, J. M. C.: DOAS measurements of formaldehyde and glyoxal above a south-east Asian tropical rainforest, *Atmos. Chem. Phys.*, 12, 5949–5962, <https://doi.org/10.5194/acp-12-5949-2012>, 2012.
- Mahajan, A. S., De Smedt, I., Biswas, M. S., Ghude, S., Fadnavis, S., Roy, C., and van Roozendaal, M.: Inter-annual variations in satellite observations of nitrogen dioxide and formaldehyde over India, *Atmos. Environ.*, 116, 194–201, <https://doi.org/10.1016/j.atmosenv.2015.06.004>, 2015.
- Marchenko, S., Krotkov, N. A., Lamsal, L. N., Celarier, E. A., Swartz, W. H., and Bucseles, E. J.: Revising the slant column density retrieval of nitrogen dioxide observed by the Ozone Monitoring Instrument, *J. Geophys. Res.-Atmos.*, 120, 5670–5692, <https://doi.org/10.1002/2014jd022913>, 2015 (data available at: <https://ladsweb.modaps.eosdis.nasa.gov/>, last access: 19 November 2020).
- Martin, R. V., Fiore, A. M., and Van Donkelaar, A.: Space-based diagnosis of surface ozone sensitivity to anthropogenic emissions, *Geophys. Res. Lett.*, 31, L06120, <https://doi.org/10.1029/2004gl019416>, 2004.
- Meller, R. and Moortgat, G. K.: Temperature dependence of the absorption cross sections of formaldehyde between 223 and 323 K in the wavelength range 225–375 nm, *J. Geophys. Res.-Atmos.*, 105, 7089–7101, <https://doi.org/10.1029/1999jd901074>, 2000.
- Mendolia, D., D'Souza, R. J. C., Evans, G. J., and Brook, J.: Comparison of tropospheric NO<sub>2</sub> vertical columns in an urban environment using satellite, multi-axis differential optical absorption spectroscopy, and in situ measurements, *Atmos. Meas. Tech.*, 6, 2907–2924, <https://doi.org/10.5194/amt-6-2907-2013>, 2013.
- Mhawish, A., Banerjee, T., Sorek-Hamer, M., Lyapustin, A., Broday, D. M., and Chatfield, R.: Comparison and evaluation of MODIS Multi-angle Implementation of Atmospheric Correction (MAIAC) aerosol product over South Asia, *Remote Sens. Environ.*, 224, 12–28, <https://doi.org/10.1016/j.rse.2019.01.033>, 2019.
- Mishra, A. K. and Sinha, V.: Emission drivers and variability of ambient isoprene, formaldehyde and acetaldehyde in north-west India during monsoon season, *Environ. Pollut.*, 267, 115538, <https://doi.org/10.1016/j.envpol.2020.115538>, 2020.
- Mishra, A. K., Sinha, B., Kumar, R., Barth, M., Hakkim, H., Kumar, V., Kumar, A., Datta, S., Guenther, A., and Sinha, V.: Cropland trees need to be included for accurate model simulations of land-atmosphere heat fluxes, temperature, boundary layer height, and ozone, *Sci. Total Environ.*, 751, 141728, <https://doi.org/10.1016/j.scitotenv.2020.141728>, 2020.
- Pathak, P. S., Dagar, J. C., Kaushal, R., and Chaturvedi, O. P.: Agroforestry Inroads from the Traditional Two-Crop Systems in Heartlands of the Indo-Gangetic Plains, in: *Agroforestry Systems in India: Livelihood Security & Ecosystem Services*, edited by: Dagar, J. C., Singh, A. K., and Arunachalam, A., Springer India, New Delhi, 87–116, 2014.
- Pawar, H., Garg, S., Kumar, V., Sachan, H., Arya, R., Sarkar, C., Chandra, B. P., and Sinha, B.: Quantifying the contribution of long-range transport to particulate matter (PM) mass loadings at a suburban site in the north-western Indo-Gangetic Plain (NW-IGP), *Atmos. Chem. Phys.*, 15, 9501–9520, <https://doi.org/10.5194/acp-15-9501-2015>, 2015.
- Peters, A. J. M., Boersma, K. F., Kroon, M., Hains, J. C., Van Roozendaal, M., Wittrock, F., Abuhassan, N., Adams, C., Akrami, M., Allaart, M. A. F., Apituley, A., Beirle, S., Bergwerff, J. B., Berkhout, A. J. C., Brunner, D., Cede, A., Chong, J., Cl  mer, K., Fayt, C., Frie  , U., Gast, L. F. L., Gil-Ojeda, M., Goutail, F., Graves, R., Griesfeller, A., Gro  mann, K., Hemerijckx, G., Hendrick, F., Henzing, B., Herman, J., Hermans, C., Hoexum, M., van der Hoff, G. R., Irie, H., Johnston, P. V., Kanaya, Y., Kim, Y. J., Klein Baltink, H., Kreher, K., de Leeuw, G., Leigh, R., Merlaud, A., Moerman, M. M., Monks, P. S., Mount, G. H., Navarro-Comas, M., Oetjen, H., Pazmino, A., Perez-Camacho, M., Peters, E., du Piesanie, A., Pinardi, G., Puentedura, O., Richter, A., Roscoe, H. K., Sch  nhardt, A., Schwarzenbach, B., Shaiganfar, R., Sluis, W., Spinei, E., Stolk, A. P., Strong, K., Swart, D. P. J., Takashima, H., Vlemmix, T., Vrekoussis, M., Wagner, T., Whyte, C., Wilson, K. M., Yela, M., Yilmaz, S., Zieger, P., and Zhou, Y.: The Cabauw Intercomparison campaign for Nitrogen Dioxide measuring Instruments (CINDI): design, execution, and early results, *Atmos. Meas. Tech.*, 5, 457–485, <https://doi.org/10.5194/amt-5-457-2012>, 2012.
- Platt, U.: Differential Optical Absorption Spectroscopy (DOAS), in: *Air Monitoring by Spectroscopic Techniques*, edited by: Sigrist, M. W., John Wiley, New York, 27–84, 1994.

- Rodgers, C. D. and Connor, B. J.: Intercomparison of remote sounding instruments, *J. Geophys. Res.-Atmos.*, 108, 4116, <https://doi.org/10.1029/2002jd002299>, 2003.
- Rothman, L. S., Gordon, I. E., Barber, R. J., Dothe, H., Gamache, R. R., Goldman, A., Perevalov, V. I., Tashkun, S. A., and Tennyson, J.: HITRAN, the high-temperature molecular spectroscopic database, *J. Quant. Spectrosc. Ra.*, 111, 2139–2150, <https://doi.org/10.1016/j.jqsrt.2010.05.001>, 2010.
- Saraswati, Sharma, S. K., and Mandal, T. K.: Five-year measurements of ambient ammonia and its relationships with other trace gases at an urban site of Delhi, India, *Meteorol. Atmos. Phys.*, 130, 241–257, <https://doi.org/10.1007/s00703-017-0512-2>, 2018.
- Sarkar, C., Kumar, V. and Sinha, V.: Massive emissions of carcinogenic benzenoids from paddy residue burning in North India, available at: <http://www.currentscience.ac.in/Volumes/104/12/1703.pdf> (last access: 20 November 2020), *Curr. Sci. India*, 104, 1703–1706, 2013.
- Sathyanadh, A., Prabhakaran, T., Patil, C., and Karipot, A.: Planetary boundary layer height over the Indian subcontinent: Variability and controls with respect to monsoon, *Atmos. Res.*, 195, 44–61, <https://doi.org/10.1016/j.atmosres.2017.05.010>, 2017.
- Schenkeveld, V. M. E., Jaross, G., Marchenko, S., Haffner, D., Kleipool, Q. L., Rozemeijer, N. C., Veefkind, J. P., and Levelt, P. F.: In-flight performance of the Ozone Monitoring Instrument, *Atmos. Meas. Tech.*, 10, 1957–1986, <https://doi.org/10.5194/amt-10-1957-2017>, 2017.
- Schreier, S. F., Richter, A., Peters, E., Ostendorf, M., Schmalwieser, A. W., Weihs, P., and Burrows, J. P.: Dual ground-based MAX-DOAS observations in Vienna, Austria: Evaluation of horizontal and temporal NO<sub>2</sub>, HCHO, and CHOCHO distributions and comparison with independent data sets, *Atmospheric Environment: X*, 5, 100059, <https://doi.org/10.1016/j.aeaoa.2019.100059>, 2020.
- Schroeder, J. R., Crawford, J. H., Fried, A., Walega, J., Weinheimer, A., Wisthaler, A., Müller, M., Mikoviny, T., Chen, G., Shook, M., Blake, D. R., and Tonnesen, G. S.: New insights into the column CH<sub>2</sub>O/NO<sub>2</sub> ratio as an indicator of near-surface ozone sensitivity, *J. Geophys. Res.-Atmos.*, 122, 8885–8907, <https://doi.org/10.1002/2017JD026781>, 2017.
- Serduchenko, A., Gorshelev, V., Weber, M., Chehade, W., and Burrows, J. P.: High spectral resolution ozone absorption cross-sections – Part 2: Temperature dependence, *Atmos. Meas. Tech.*, 7, 625–636, <https://doi.org/10.5194/amt-7-625-2014>, 2014.
- Shaiganfar, R., Beirle, S., Sharma, M., Chauhan, A., Singh, R. P., and Wagner, T.: Estimation of NO<sub>x</sub> emissions from Delhi using Car MAX-DOAS observations and comparison with OMI satellite data, *Atmos. Chem. Phys.*, 11, 10871–10887, <https://doi.org/10.5194/acp-11-10871-2011>, 2011.
- Shaiganfar, R., Beirle, S., Denier van der Gon, H., Jonkers, S., Kuenen, J., Petetin, H., Zhang, Q., Beekmann, M., and Wagner, T.: Estimation of the Paris NO<sub>x</sub> emissions from mobile MAX-DOAS observations and CHIMERE model simulations during the MEGAPOLI campaign using the closed integral method, *Atmos. Chem. Phys.*, 17, 7853–7890, <https://doi.org/10.5194/acp-17-7853-2017>, 2017.
- Sharma, S., Chatani, S., Mahtta, R., Goel, A., and Kumar, A.: Sensitivity analysis of ground level ozone in India using WRF-CMAQ models, *Atmos. Environ.*, 131, 29–40, <https://doi.org/10.1016/j.atmosenv.2016.01.036>, 2016.
- Singh, A. P., Varshney, C. K., and Singh, U. K.: Seasonal Variations in Isoprene Emission from Tropical Deciduous Tree Species, *Environ. Monit. Assess.*, 131, 231–235, <https://doi.org/10.1007/s10661-006-9471-7>, 2007.
- Singla, V., Satsangi, A., Pachauri, T., Lakhani, A., and Kumari, K. M.: Ozone formation and destruction at a sub-urban site in North Central region of India, *Atmos. Res.*, 101, 373–385, <https://doi.org/10.1016/j.atmosres.2011.03.011>, 2011.
- Sinha, B., Singh Sangwan, K., Maurya, Y., Kumar, V., Sarkar, C., Chandra, B. P., and Sinha, V.: Assessment of crop yield losses in Punjab and Haryana using 2 years of continuous in situ ozone measurements, *Atmos. Chem. Phys.*, 15, 9555–9576, <https://doi.org/10.5194/acp-15-9555-2015>, 2015.
- Sinha, V., Kumar, V., and Sarkar, C.: Chemical composition of pre-monsoon air in the Indo-Gangetic Plain measured using a new air quality facility and PTR-MS: high surface ozone and strong influence of biomass burning, *Atmos. Chem. Phys.*, 14, 5921–5941, <https://doi.org/10.5194/acp-14-5921-2014>, 2014.
- Sinreich, R., Frie, Wagner, T., and Platt, U.: Multi axis differential optical absorption spectroscopy (MAX-DOAS) of gas and aerosol distributions, *Faraday Discuss.*, 130, 153–164, 2005.
- Surl, L., Palmer, P. I., and González Abad, G.: Which processes drive observed variations of HCHO columns over India?, *Atmos. Chem. Phys.*, 18, 4549–4566, <https://doi.org/10.5194/acp-18-4549-2018>, 2018.
- Thalman, R. and Volkamer, R.: Temperature dependent absorption cross-sections of O<sub>2</sub>–O<sub>2</sub> collision pairs between 340 and 630 nm and at atmospherically relevant pressure, *Phys. Chem. Chem. Phys.*, 15, 15371–15381, <https://doi.org/10.1039/C3CP50968K>, 2013.
- Tiwari, S., Dahiya, A., and Kumar, N.: Investigation into relationships among NO, NO<sub>2</sub>, NO<sub>x</sub>, O<sub>3</sub>, and CO at an urban background site in Delhi, India, *Atmos. Res.*, 157, 119–126, <https://doi.org/10.1016/j.atmosres.2015.01.008>, 2015.
- Torres, O., Tanskanen, A., Veihelmann, B., Ahn, C., Braak, R., Bhartia, P. K., Veefkind, P., and Levelt, P.: Aerosols and surface UV products from Ozone Monitoring Instrument observations: An overview, *J. Geophys. Res.-Atmos.*, 112, D24S47, <https://doi.org/10.1029/2007jd008809>, 2007 (data available at: <https://ladsweb.modaps.eosdis.nasa.gov/>, last access: 19 November 2020).
- Tripathi, S. and Mahey, K.: Urbanization and economic growth in Punjab (India): an empirical analysis, *Urban Research & Practice*, 10, 379–402, <https://doi.org/10.1080/17535069.2016.1227875>, 2017.
- Tripathi, S. N., Dey, S., Chandel, A., Srivastava, S., Singh, R. P., and Holben, B. N.: Comparison of MODIS and AERONET derived aerosol optical depth over the Ganga Basin, India, *Ann. Geophys.*, 23, 1093–1101, <https://doi.org/10.5194/angeo-23-1093-2005>, 2005.
- Vandaele, A. C., Hermans, C., Simon, P. C., Carleer, M., Colin, R., Fally, S., Mérienne, M. F., Jenouvrier, A., and Coquart, B.: Measurements of the NO<sub>2</sub> absorption cross-section from 42 000 cm<sup>-1</sup> to 10 000 cm<sup>-1</sup> (238–1000 nm) at 220 K and 294 K, *J. Quant. Spectrosc. Ra.*, 59, 171–184, [https://doi.org/10.1016/S0022-4073\(97\)00168-4](https://doi.org/10.1016/S0022-4073(97)00168-4), 1998.

- van Geffen, J. H. G. M., Boersma, K. F., Eskes, H. J., Maasakkers, J. D., and Veeffkind, J. P.: TROPOMI ATBD of the total and tropospheric NO<sub>2</sub> data products, Royal Netherlands Meteorological Institute, 2017.
- Veeffkind, J. P., Aben, I., McMullan, K., Förster, H., de Vries, J., Otter, G., Claas, J., Eskes, H. J., de Haan, J. F., Kleipool, Q., van Weele, M., Hasekamp, O., Hoogeveen, R., Landgraf, J., Snel, R., Tol, P., Ingmann, P., Voors, R., Kruizinga, B., Vink, R., Visser, H., and Levelt, P. F.: TROPOMI on the ESA Sentinel-5 Precursor: A GMES mission for global observations of the atmospheric composition for climate, air quality and ozone layer applications, *Remote Sens. Environ.*, 120, 70–83, <https://doi.org/10.1016/j.rse.2011.09.027>, 2012.
- Vlemmix, T., Hendrick, F., Pinardi, G., De Smedt, I., Fayt, C., Hermans, C., Pipers, A., Wang, P., Levelt, P., and Van Roozendaal, M.: MAX-DOAS observations of aerosols, formaldehyde and nitrogen dioxide in the Beijing area: comparison of two profile retrieval approaches, *Atmos. Meas. Tech.*, 8, 941–963, <https://doi.org/10.5194/amt-8-941-2015>, 2015.
- Wagner, T. and Beirle, S.: Estimation of the horizontal sensitivity range from MAX-DOAS O<sub>4</sub> observations, Report, QA4ECV, 2016.
- Wagner, T., Dix, B., Friedeburg, C. v., Frieß, U., Sanghavi, S., Sinreich, R., and Platt, U.: MAX-DOAS O<sub>4</sub> measurements: A new technique to derive information on atmospheric aerosols—Principles and information content, *J. Geophys. Res.*, 109, D22205, <https://doi.org/10.1029/2004jd004904>, 2004.
- Wagner, T., Deutschmann, T., and Platt, U.: Determination of aerosol properties from MAX-DOAS observations of the Ring effect, *Atmos. Meas. Tech.*, 2, 495–512, <https://doi.org/10.5194/amt-2-495-2009>, 2009.
- Wagner, T., Beirle, S., Brauers, T., Deutschmann, T., Frieß, U., Hak, C., Halla, J. D., Heue, K. P., Junkermann, W., Li, X., Platt, U., and Pundt-Gruber, I.: Inversion of tropospheric profiles of aerosol extinction and HCHO and NO<sub>2</sub> mixing ratios from MAX-DOAS observations in Milano during the summer of 2003 and comparison with independent data sets, *Atmos. Meas. Tech.*, 4, 2685–2715, <https://doi.org/10.5194/amt-4-2685-2011>, 2011.
- Wagner, T., Apituley, A., Beirle, S., Dörner, S., Friess, U., Remmers, J., and Shaiganfar, R.: Cloud detection and classification based on MAX-DOAS observations, *Atmos. Meas. Tech.*, 7, 1289–1320, <https://doi.org/10.5194/amt-7-1289-2014>, 2014.
- Wagner, T., Beirle, S., Remmers, J., Shaiganfar, R., and Wang, Y.: Absolute calibration of the colour index and O<sub>4</sub> absorption derived from Multi AXis (MAX-)DOAS measurements and their application to a standardised cloud classification algorithm, *Atmos. Meas. Tech.*, 9, 4803–4823, <https://doi.org/10.5194/amt-9-4803-2016>, 2016.
- Wagner, T., Beirle, S., Benavent, N., Bösch, T., Chan, K. L., Donner, S., Dörner, S., Fayt, C., Frieß, U., García-Nieto, D., Gielen, C., González-Bartolome, D., Gomez, L., Hendrick, F., Henzing, B., Jin, J. L., Lampel, J., Ma, J., Mies, K., Navarro, M., Peters, E., Pinardi, G., Puenteledura, O., Puñte, J., Remmers, J., Richter, A., Saiz-Lopez, A., Shaiganfar, R., Sihler, H., Van Roozendaal, M., Wang, Y., and Yela, M.: Is a scaling factor required to obtain closure between measured and modelled atmospheric O<sub>4</sub> absorptions? An assessment of uncertainties of measurements and radiative transfer simulations for 2 selected days during the MAD-CAT campaign, *Atmos. Meas. Tech.*, 12, 2745–2817, <https://doi.org/10.5194/amt-12-2745-2019>, 2019.
- Wang, Y., Li, A., Xie, P. H., Wagner, T., Chen, H., Liu, W. Q., and Liu, J. G.: A rapid method to derive horizontal distributions of trace gases and aerosols near the surface using multi-axis differential optical absorption spectroscopy, *Atmos. Meas. Tech.*, 7, 1663–1680, <https://doi.org/10.5194/amt-7-1663-2014>, 2014.
- Wang, Y., Penning de Vries, M., Xie, P. H., Beirle, S., Dörner, S., Remmers, J., Li, A., and Wagner, T.: Cloud and aerosol classification for 2.5 years of MAX-DOAS observations in Wuxi (China) and comparison to independent data sets, *Atmos. Meas. Tech.*, 8, 5133–5156, <https://doi.org/10.5194/amt-8-5133-2015>, 2015.
- Wang, Y., Beirle, S., Lampel, J., Koukouli, M., De Smedt, I., Theys, N., Li, A., Wu, D., Xie, P., Liu, C., Van Roozendaal, M., Stavrou, T., Müller, J.-F., and Wagner, T.: Validation of OMI, GOME-2A and GOME-2B tropospheric NO<sub>2</sub>, SO<sub>2</sub> and HCHO products using MAX-DOAS observations from 2011 to 2014 in Wuxi, China: investigation of the effects of priori profiles and aerosols on the satellite products, *Atmos. Chem. Phys.*, 17, 5007–5033, <https://doi.org/10.5194/acp-17-5007-2017>, 2017a.
- Wang, Y., Lampel, J., Xie, P., Beirle, S., Li, A., Wu, D., and Wagner, T.: Ground-based MAX-DOAS observations of tropospheric aerosols, NO<sub>2</sub>, SO<sub>2</sub> and HCHO in Wuxi, China, from 2011 to 2014, *Atmos. Chem. Phys.*, 17, 2189–2215, <https://doi.org/10.5194/acp-17-2189-2017>, 2017b.
- Wang, Y., Dörner, S., Donner, S., Böhnke, S., De Smedt, I., Dickerson, R. R., Dong, Z., He, H., Li, Z., Li, Z., Li, D., Liu, D., Ren, X., Theys, N., Wang, Y., Wang, Y., Wang, Z., Xu, H., Xu, J., and Wagner, T.: Vertical profiles of NO<sub>2</sub>, SO<sub>2</sub>, HONO, HCHO, CHOCHO and aerosols derived from MAX-DOAS measurements at a rural site in the central western North China Plain and their relation to emission sources and effects of regional transport, *Atmos. Chem. Phys.*, 19, 5417–5449, <https://doi.org/10.5194/acp-19-5417-2019>, 2019.
- Wolfe, G. M., Kaiser, J., Hanisco, T. F., Keutsch, F. N., de Gouw, J. A., Gilman, J. B., Graus, M., Hatch, C. D., Holloway, J., Horowitz, L. W., Lee, B. H., Lerner, B. M., Lopez-Hilfiker, F., Mao, J., Marvin, M. R., Peischl, J., Pollack, I. B., Roberts, J. M., Ryerson, T. B., Thornton, J. A., Veres, P. R., and Warneke, C.: Formaldehyde production from isoprene oxidation across NO<sub>x</sub> regimes, *Atmos. Chem. Phys.*, 16, 2597–2610, <https://doi.org/10.5194/acp-16-2597-2016>, 2016.
- Wolfe, G. M., Nicely, J. M., St. Clair, J. M., Hanisco, T. F., Liao, J., Oman, L. D., Brune, W. B., Miller, D., Thames, A., González Abad, G., Ryerson, T. B., Thompson, C. R., Peischl, J., McKain, K., Sweeney, C., Wennberg, P. O., Kim, M., Crouse, J. D., Hall, S. R., Ullmann, K., Diskin, G., Bui, P., Chang, C., and Dean-Day, J.: Mapping hydroxyl variability throughout the global remote troposphere via synthesis of airborne and satellite formaldehyde observations, *P. Natl. Acad. Sci. USA*, 116, 11171–11180, <https://doi.org/10.1073/pnas.1821661116>, 2019.
- Zara, M., Boersma, K. F., De Smedt, I., Richter, A., Peters, E., van Geffen, J. H. G. M., Beirle, S., Wagner, T., Van Roozendaal, M., Marchenko, S., Lamsal, L. N., and Eskes, H. J.: Improved slant column density retrieval of nitrogen dioxide and formaldehyde for OMI and GOME-2A from QA4ECV: intercomparison, uncertainty characterisation, and trends, *Atmos. Meas. Tech.*, 11, 4033–4058, <https://doi.org/10.5194/amt-11-4033-2018>, 2018.

- Zhang, W., Gu, X., Xu, H., Yu, T., and Zheng, F.: Assessment of OMI near-UV aerosol optical depth over Central and East Asia, *J. Geophys. Res.-Atmos.*, 121, 382–398, <https://doi.org/10.1002/2015jd024103>, 2016.
- Zhao, J. and Zhang, R.: Proton transfer reaction rate constants between hydronium ion (H<sub>3</sub>O<sup>+</sup>) and volatile organic compounds, *Atmos. Environ.*, 38, 2177–2185, <https://doi.org/10.1016/j.atmosenv.2004.01.019>, 2004.
- Zhu, L., Mickley, L. J., Jacob, D. J., Marais, E. A., Sheng, J., Hu, L., Abad, G. G., and Chance, K.: Long-term (2005–2014) trends in formaldehyde (HCHO) columns across North America as seen by the OMI satellite instrument: Evidence of changing emissions of volatile organic compounds, *Geophys. Res. Lett.*, 44, 7079–7086, <https://doi.org/10.1002/2017gl073859>, 2017.